

Lawrence Berkeley National Laboratory

Recent Work

Title

DEVELOPMENT OF NEUTRON LEAKAGE SPECTROMETERS WITH EMPHASIS ON THE keV RANGE

Permalink

<https://escholarship.org/uc/item/2pv4z2vh>

Author

Henninger, Rudolph J.

Publication Date

1971-03-01

C. J.

DEVELOPMENT OF NEUTRON LEAKAGE SPECTROMETERS
WITH EMPHASIS ON THE keV RANGE

Rudolph J. Henninger
(Ph. D. Thesis)

March 1971

AEC Contract No. W-7405-eng-48

TWO-WEEK LOAN COPY

*This is a Library Circulating Copy
which may be borrowed for two weeks.
For a personal retention copy, call
Tech. Info. Division, Ext. 5545*

LAWRENCE RADIATION LABORATORY
UNIVERSITY of CALIFORNIA BERKELEY

C. J.

DISCLAIMER

This document was prepared as an account of work sponsored by the United States Government. While this document is believed to contain correct information, neither the United States Government nor any agency thereof, nor the Regents of the University of California, nor any of their employees, makes any warranty, express or implied, or assumes any legal responsibility for the accuracy, completeness, or usefulness of any information, apparatus, product, or process disclosed, or represents that its use would not infringe privately owned rights. Reference herein to any specific commercial product, process, or service by its trade name, trademark, manufacturer, or otherwise, does not necessarily constitute or imply its endorsement, recommendation, or favoring by the United States Government or any agency thereof, or the Regents of the University of California. The views and opinions of authors expressed herein do not necessarily state or reflect those of the United States Government or any agency thereof or the Regents of the University of California.

TABLE OF CONTENTS

	<u>Page</u>
I. INTRODUCTION	1
II. THEORY	
A. Interpretation of Measurements by a Leakage Spectrometer	14
B. Determining the Spectrum from the Measurements	20
C. Method of Calculating Response Functions	22
D. Description of Input Data and Test Calculations	37
E. Results	53
III. EXPERIMENT	
A. Apparatus and Experimental Results	68
B. Analysis of Experiment and Comparison of Results	74
IV. SUMMARY OF RESULTS AND CONCLUSIONS	84
APPENDICES	
Appendix A. Development of Group Equations Used in ANISN	85
Appendix B. Tests of ANISN	89
Appendix C. Cross Sections and Energy Transfer Array	95
REFERENCES	103
ACKNOWLEDGMENTS	106

DEVELOPMENT OF NEUTRON LEAKAGE SPECTROMETERS
WITH EMPHASIS ON THE keV RANGE

Ph.D.

Rudolph J. Henninger

Nuclear Engineering

Harvey Amster
Chairman, Thesis Committee

ABSTRACT

Calculations were performed to design and analyze a set of neutron spectrometers consisting of cadmium-covered, spherically-shaped, resonance-absorbing cores, surrounded by various-sized polyethylene spheres. Some of the detectors had an additional layer of boron around the polyethylene. Because of the combined effects of leakage (hence the name) and moderation in the polyethylene, the measured activation of the resonance absorber depends on the incident neutron energy, with a maximum in an energy range determined by the sizes and properties of all the materials. This response is proportional to the adjoint flux, which is calculated by the multigroup discrete ordinate transport code ANISN. The adjoint boundary condition is the probability that a neutron entering the core is captured there. It is assumed that this probability is independent of the presence of the surrounding materials.

Calculations were performed for polyethylene sphere diameters varying from 2 in. to 10 in. to find a set useful in the keV region. Some of these calculations were compared

with experiments performed by S. Binney and Hans Mark using nearly monoenergetic keV photoneutrons. The experimental results were typically about 30% different from those calculated.

INTRODUCTION

The measurement of neutron energy distributions is important for many applications of nuclear energy. Checking calculations that predict the behavior of the "fast" reactors now being developed require this knowledge. This need is particularly acute in the energy region between 1 keV and 1 MeV since most of the fission events are initiated there. For any source of neutrons, calculation of both the neutron induced biological dose rate and flux attenuation by shielding material require knowledge of the spectrum, since the relative biological effectiveness depends strongly on neutron energy.

Within the thermal and epithermal ranges, foil activation techniques have been employed extensively to measure spectra. This method is very convenient since the foils are very small and can easily be placed in many positions inside of assemblies. They are efficient, so that very small quantities of material can be used, hence the flux distribution is not disturbed. The cross sections for activation in this energy range are well known, and, since it is the radioactivity induced in the foil that is measured, the readings do not suffer from interference by gamma rays nor "flooding" from intense neutron pulses. Finally, the existence of large resonances in the cross sections at epithermal energies makes it relatively easy to interpret the activation measurements in terms of the neutron flux

over a narrow energy range.

Activation methods, however, do not work well in the energy region between 1 keV and 1 MeV. At these energies, there are no isolated activation resonances which can be used to define a narrow band; also, the cross sections have not been measured precisely enough. Mechanical choppers have also been used with success in the eV range but above the low keV range their resolution becomes unacceptable.

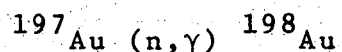
Above 1 MeV spectra can be measured by means of threshold detectors, nuclear emulsions, semiconductor detectors or proton recoil spectrometers. Attempts to extend these methods downward in energy have met with serious difficulties. Thresholds for nuclear reactions are too high (above 1 MeV) for this method to be used. Proton recoil, nuclear emulsion, and semiconductor detectors will operate in the keV range, but generally resolution restricts their usefulness to the very high keV range and above (a good review of the applicability of these detectors can be found in Ref. K160). Good measurements in the keV range can be obtained with time-of-flight methods, but complicated equipment is required as well as an aperture for bringing out the neutron beam.

In consideration of this gap in the field of neutron spectrometry, the purpose of this work will be to adapt activation techniques, with their inherent advantages,

to measure neutron energy distributions in the keV range.

Gold foil activation has been a traditional method for determining certain flux properties in thermal reactors.

The reaction



has a strong resonance at an incident neutron energy of 4.9 eV. Below this energy, the cross section is approximately inversely proportional to the square root of the incident neutron energy (see Figure 1).

A limited amount of spectral information can be obtained by the so-called cadmium ratio measurements. The activation of gold foils shielded with cadmium, to remove thermal neutrons (see Figure 1), determines essentially the neutron flux near five electron volts, provided the spectrum rapidly decreases with increasing neutron energy. The difference between the counting rate of an activated bare foil and a cadmium covered foil is a measure of the flux below the cadmium "cut-off" energy at 0.4 eV.

The same principle can be applied with other elements having strong capture resonances in their cross sections. The induced activity of a foil exposed to a neutron flux $\phi(E)$ is proportional to the integral

$$I = \int \phi(E)\sigma(E)dE \cdot$$

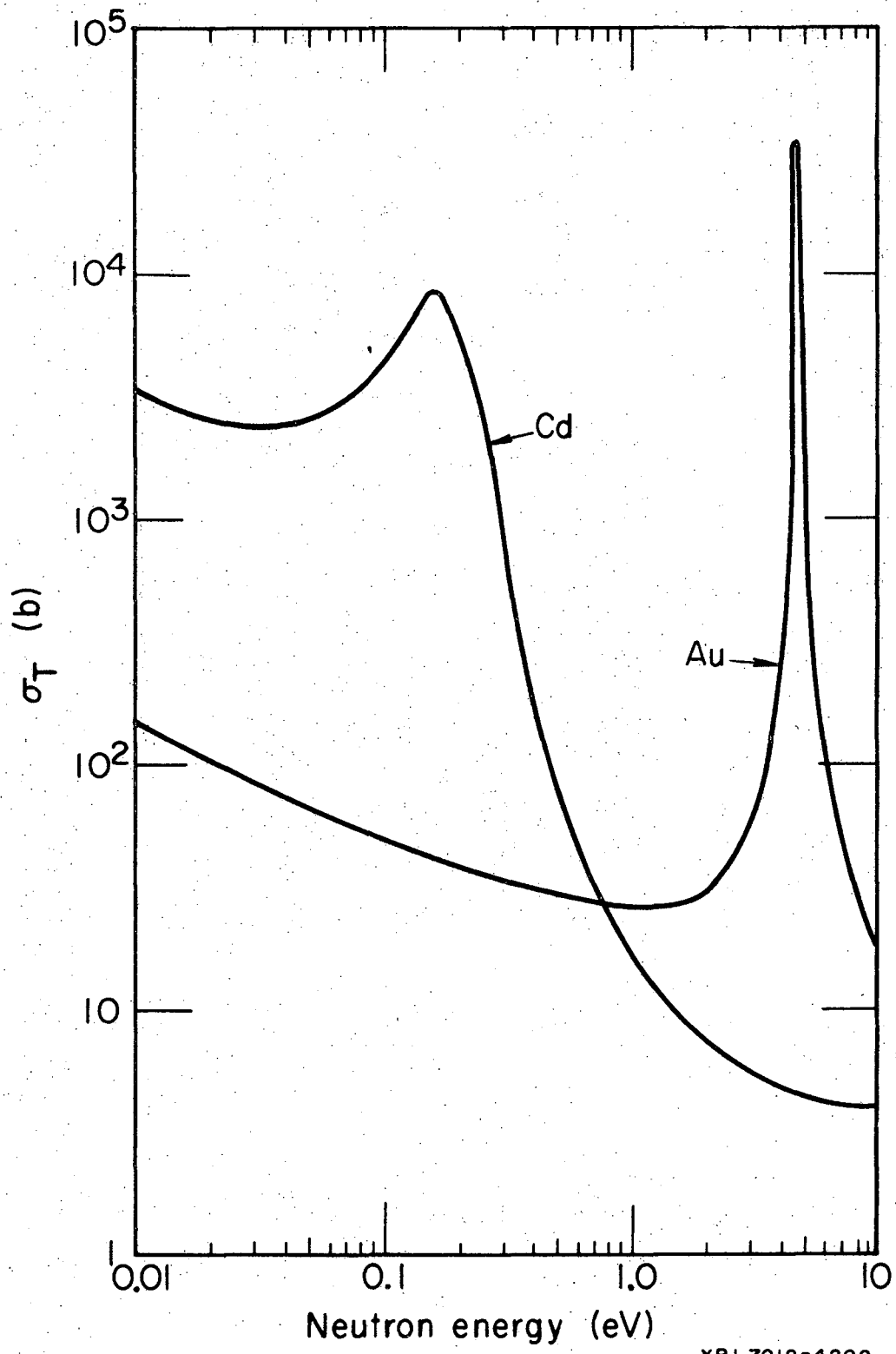


FIGURE 1. Total Cross Sections for Gold and Cadmium

XBL7012-4208

If the flux has the form

$$\phi \sim \frac{1}{E},$$

which is approximately the case for the epithermal flux in a large non-absorbing system, and the cross section $\sigma(E)$ is dominated by a single large resonance, then the activation of a cadmium covered foil is given by the resonance integral

$$I_{\text{res}} = \int_{.4\text{eV}}^{\infty} \sigma(E) \frac{dE}{E} \quad (\text{I.1})$$

where the lower limit has been set at the cadmium cut-off energy. The cadmium cover is used to eliminate the large activation due to thermal neutrons. Table 1 lists the elements generally used as resonance absorbers, along with the half-life of the isotopes resulting from capture, and the resonance integral.

Several theoretical methods for converting the observed activities of the different isotopes into usable information about the neutron spectrum have been devised for the region indicated in Table 1. However, the activation method described thus far are not useful in the energy region of interest without further modification.

A "spectrum shifting" method will now be described which will make it possible to use these methods at higher

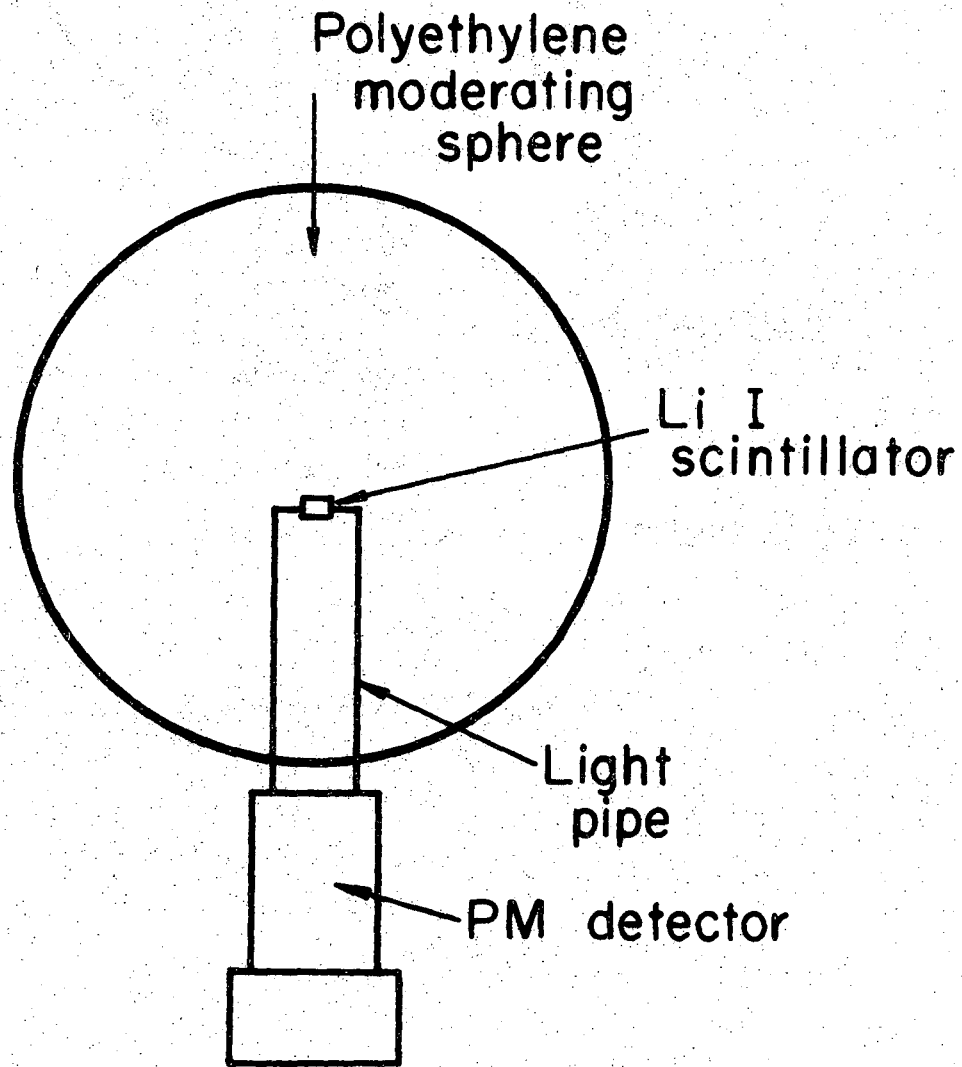
TABLE 1
ISOTOPES USED FOR ACTIVATION ANALYSIS

Element	Resonance Energy (eV)	I_{res} (b)	$T_{1/2}$
In	1.45	2060	54 min
Au	4.9	1543	2.7 d
Mn	337	15	2.56h
W	18.8	500	24 h
Co	132	65	5.2 y
Na	2850	.50	15 h

energies. In 1960, T.W. Bonner devised a multisphere technique for measuring the neutron spectra produced by isotopes undergoing spontaneous fission.^{Br60,Bo61} This method makes use of the inherent advantages of spherical symmetry, which were originally pointed out by Thompson.^{Th53} The "Bonner" sphere consists of a lithium iodide scintillation crystal, which is sensitive to thermal neutrons, surrounded by a polyethylene sphere (Figure 2). The polyethylene (CH₂) acts as a moderator for incident neutrons, slowing them to thermal energies, where they can be detected by the lithium iodide crystal.

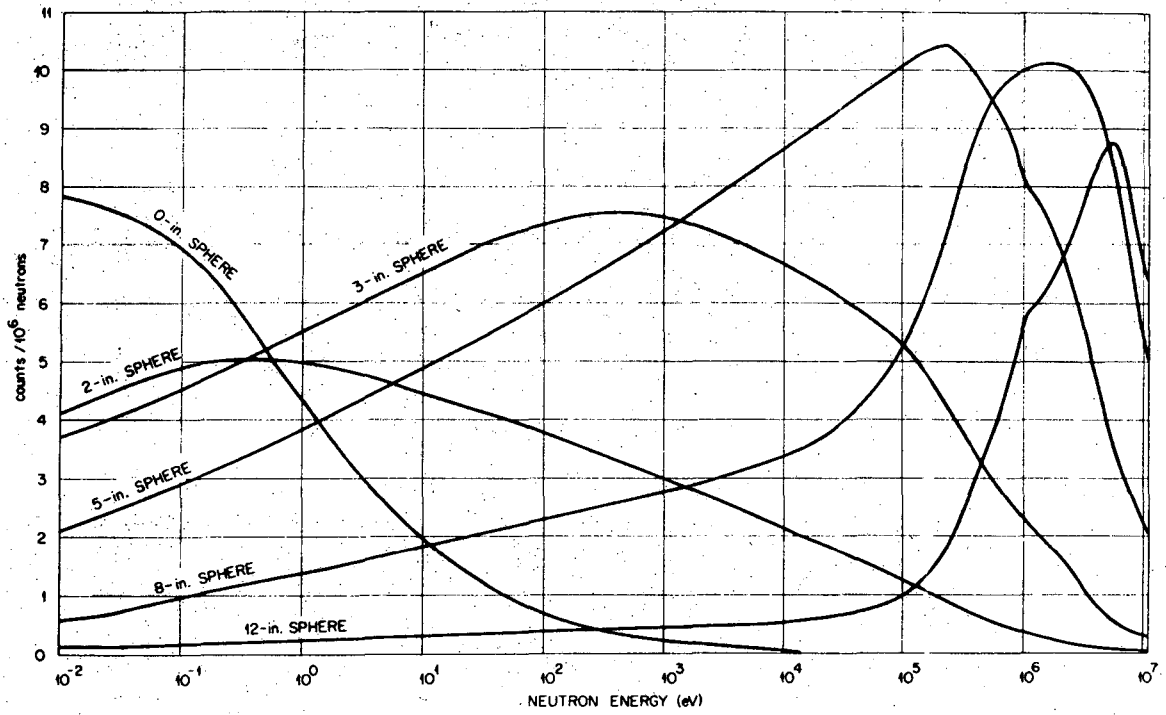
The response of each sphere was measured by means of monoenergetic neutrons produced by a Van de Graaff accelerator and a ⁷Li(p,n)⁷Be reaction. The results obtained for different sized moderating spheres is shown in Figure 3. As can be seen in the figure, the response functions peak in the energy range from about .3 eV to 4 MeV.

The explanation of the peaking is simple: at high incident energies, most of the neutrons leak out of the detector before they can scatter enough times to become thermalized and hence detected. On the other hand, a large fraction of the incident low energy neutrons becomes thermal before reaching the center, and therefore leaks out before being captured there. The large thermal scattering cross section of hydrogen in the polyethylene enhances this effect. A neutron entering near the peak



XBL7012-4206

FIGURE 2. Bonner Leakage Spectrometer



XBL 7012-7161

FIGURE 3. Response Functions for Bonner Spheres. Me65

undergoes, on the average, the number of collisions required to reach thermal energy at the center. Since the peaking is caused by leakage, this type of spectrometer will be referred to here as a "leakage" spectrometer (LS).

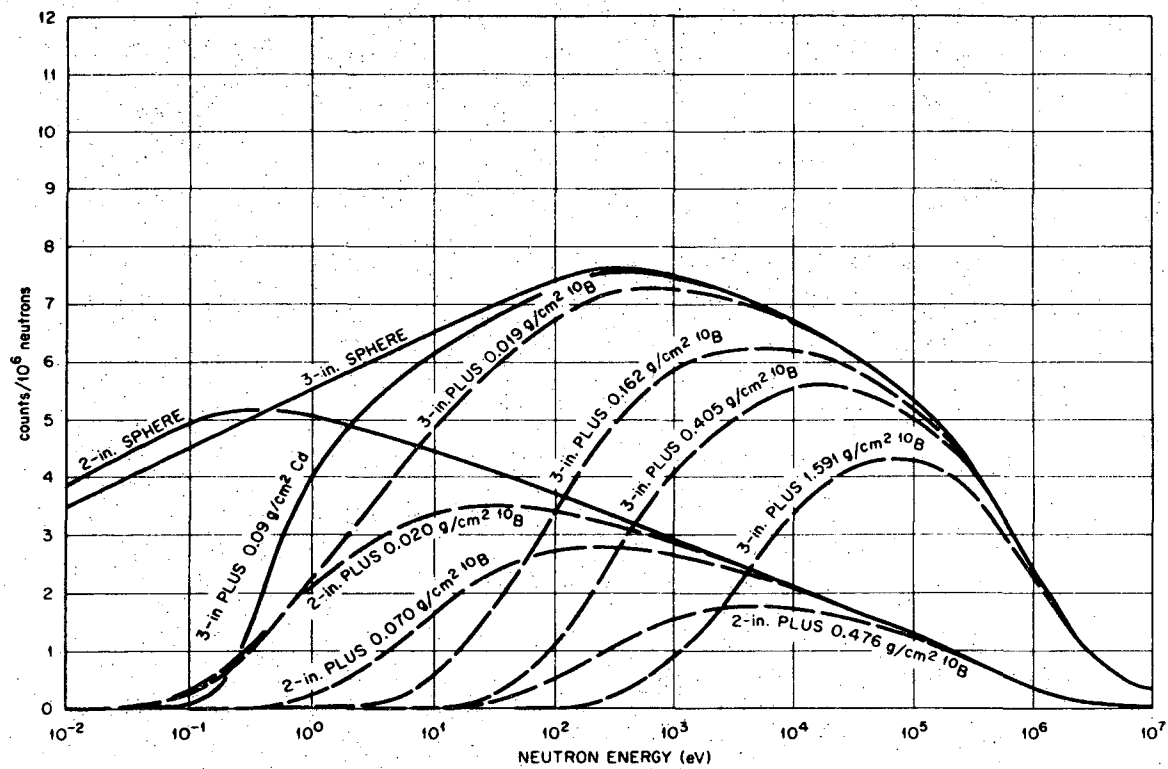
A reduction in the size of the Bonner Leakage Spectrometer, some of which reach 12" in diameter, would be an important improvement. This can be accomplished by replacing the lithium iodide crystal and the necessary light pipe and photomultiplier assembly by something that would detect neutrons at a higher energy, hence, requiring less moderator. A cadmium covered activation foil can be used as such a detector and, therefore, seems a good choice. In this way, incident high energy neutrons (keV and above) will be shifted to an energy region in which they can be detected more easily.

Another important advantage of using a cadmium covered resonance absorber occurs in the calculation of the response curves. Because of the scarcity of monoenergetic neutron sources in the keV range for use in calibration, calculations must be heavily relied upon and any simplification of them is helpful. At energies above the cadmium cut-off the nuclei with which the neutrons interact may be considered stationary compared to the neutrons, and chemical binding effects that are important mainly at thermal energies may be neglected.

When the thermal detector is replaced by one for the

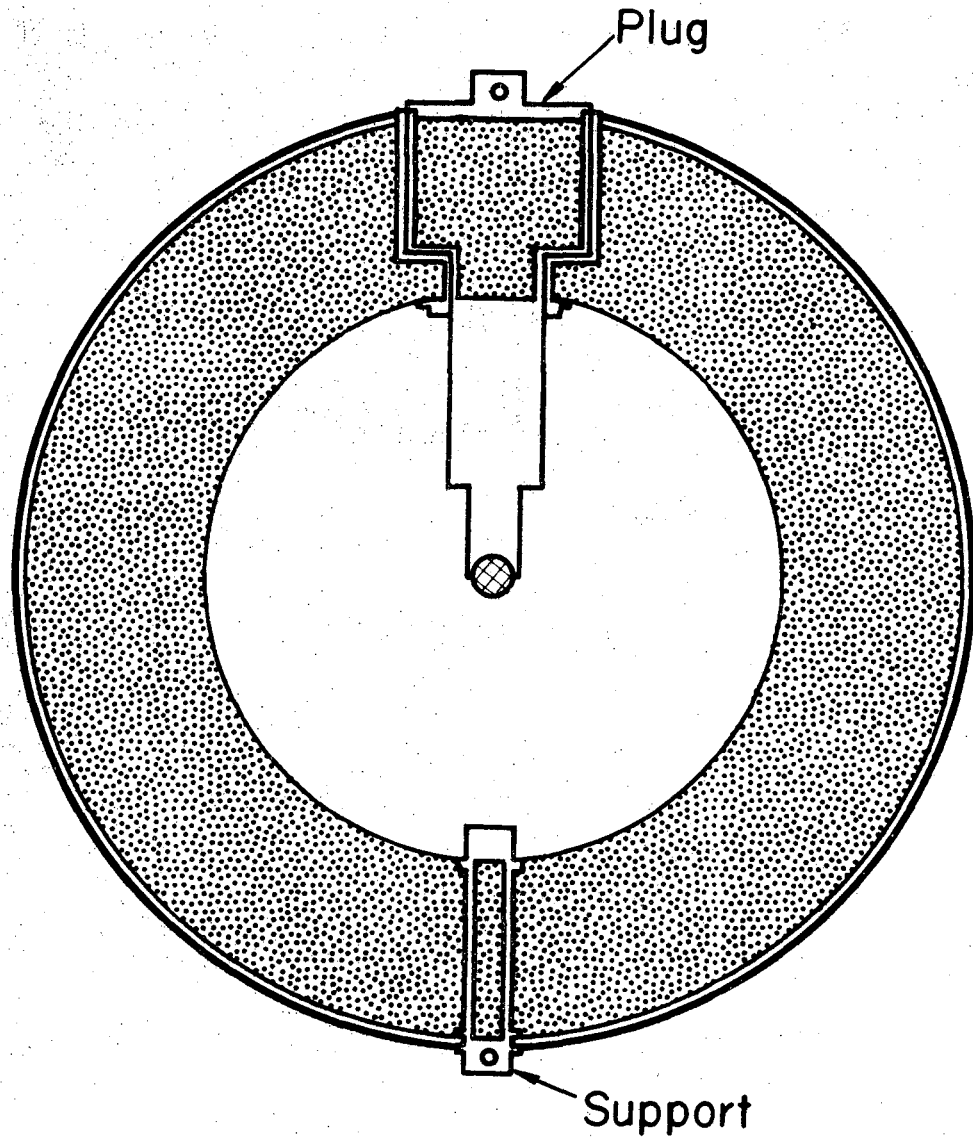
eV range, and the amount of polyethylene is reduced so that the peak sensitivity is at the same energy, the resulting response shape remains approximately the same at all energies. In particular, the resolution of the smaller sized detectors remains poor. The response can be considerably sharpened, however, by adding a layer of boron around the outside of the moderator. Since boron is a $1/v$ absorber, lower energy neutrons are preferentially removed. This effect can be seen in some curves calculated by S.K. Metha^{Me64, Me65} who used spheres, as Bonner had constructed, modified in this manner. Figure 4 shows the lowering of the response at low energies and the shifting of the peak response to higher energies with the addition of a layer of boron.

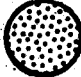


The proposed spectrometers consist of a cadmium covered resonance absorber surrounded by various sized polyethylene spheres (Figure 5). Some have an additional layer of boron. In the following sections, the use and design of this new spectrometer will be described, and calculated response functions will be given for several sizes and resonant absorbers. An experiment is briefly described, the results of which are compared with the calculations.



XBL 7012-7162

FIGURE 4. Response Functions for Modified Bonner Spheres. Me65.



-  Boron carbide powder
-  In-Cd foil
-  Polyethylene

XBL7012-4207

FIGURE 5. Activation Leakage Spectrometer
(cross sectional view)

II. THEORY

A. Interpretation of Measurements by a Leakage Spectrometer

In this section a definition of what a Leakage Spectrometer (LS) measures will be made. Where and how a set of LS's can be used for determining neutron spectra will then be discussed.

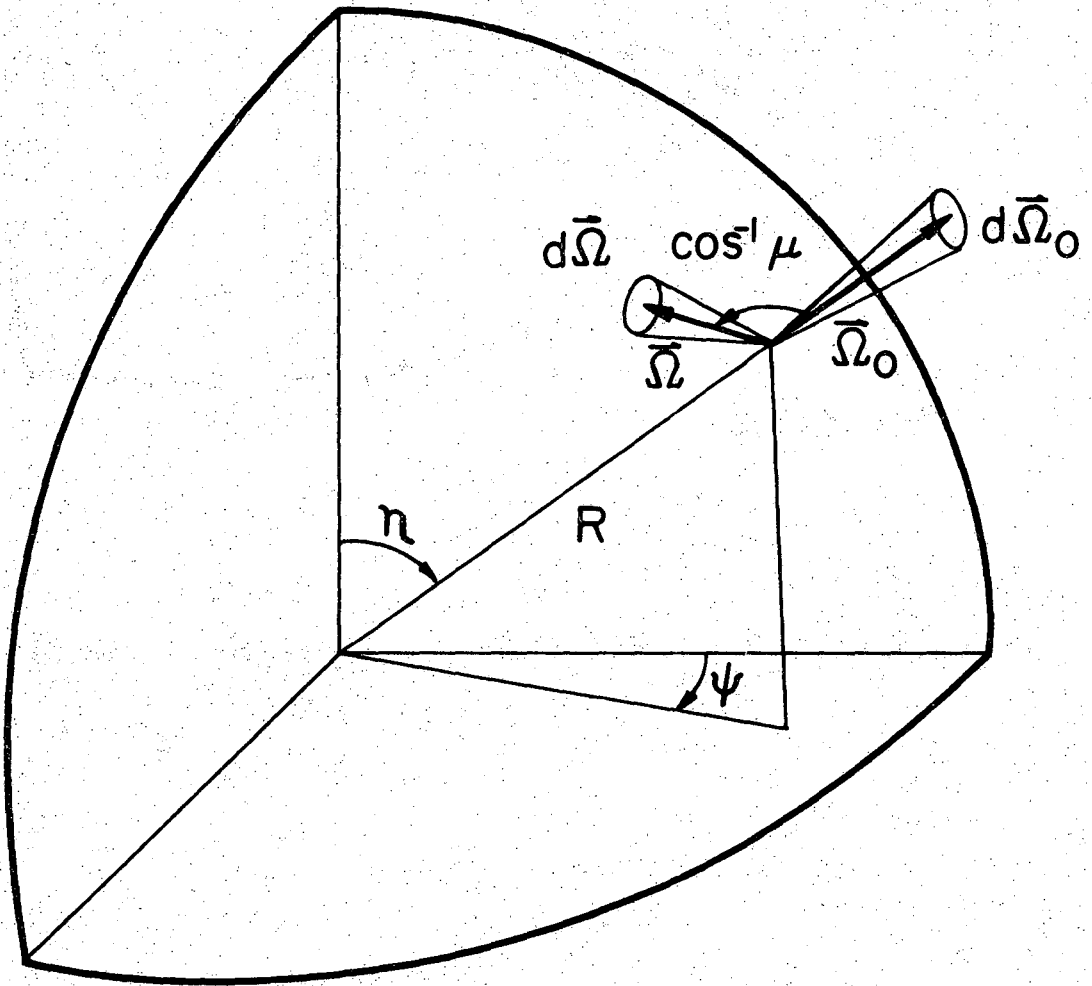
Let $F^+(E, \mu)$ be the probability that a neutron having an energy E and making an angle $\cos^{-1} \mu$ with the outward pointing normal at the surface of the spectrometer, will be absorbed in the core material. This quantity depends on no angles other than $\cos^{-1} \mu$ because of the spherical symmetry. Furthermore, since only incoming neutrons can be absorbed,

$$F^+(E, \mu) = 0 \quad \text{for } \mu > 0 .$$

Let $F(R, \vec{\Omega}_0, E, \vec{\Omega})$ be the angular flux at the position $(R, \vec{\Omega}_0)$ with energy E and direction $\vec{\Omega}$ as shown in Figure 6. Here R is the radius of the spectrometer, so the flux is evaluated at its surface. With this angular flux,

$$F(R, \vec{\Omega}_0, E, \vec{\Omega}) R^2 (-\vec{\Omega} \cdot \vec{\Omega}_0) d\vec{\Omega}_0 d\vec{\Omega} dE \quad \text{neutrons/sec}$$

enter an area $R^2 d\vec{\Omega}_0$ on the surface with directions in $d\vec{\Omega}$ about $\vec{\Omega}$. Thus A , the number of absorptions per second in the core material for the flux given, is



XBL711-2735

FIGURE 6. Geometry for Calculating L.S. Capture Probability

$$A = R^2 \int_{4\pi} d\vec{\Omega}_o \int_{\vec{\Omega} \cdot \vec{\Omega}_o < 0} d\vec{\Omega} \int dE F^+(E, -\vec{\Omega} \cdot \vec{\Omega}_o) F(R, \vec{\Omega}_o, E, \vec{\Omega}) (-\vec{\Omega} \cdot \vec{\Omega}_o) \quad (\text{II.1})$$

At saturation the number of absorptions per second is equal to the activity of the core material.

We now define $\sigma_{LS}(E)$ the "effective cross section of the spectrometer",

$$\sigma_{LS}(E) \equiv A(E) / \bar{\phi}(E) \quad (\text{II.2})$$

where $A(E)dE$ is the number of neutrons absorbed that enter at energies in dE and

$$\bar{\phi} \equiv \frac{1}{4\pi} \int_{4\pi} d\vec{\Omega}_o \cdot 2 \int_{\vec{\Omega} \cdot \vec{\Omega}_o < 0} d\vec{\Omega} F(R, \vec{\Omega}_o, E, \vec{\Omega}) \quad (\text{II.3})$$

$\bar{\phi}$ will be thought of as the average inward scalar flux which under certain conditions mentioned below is the scalar flux "at" the surface of the LS. The saturated activity then becomes

$$A = \int A(E) dE = \int \bar{\phi}(E) \sigma_{LS}(E) dE \quad .$$

Now if the angular flux $F(R, \vec{\Omega}_o, E, \vec{\Omega})$ for neutrons entering the LS is independent of position on the surface of the LS, then

$$\bar{\phi}(E) = \frac{2}{4\pi} \int_{4\pi} d\vec{\Omega}_0 \int_{\vec{\Omega} \cdot \vec{\Omega}_0 < 0} d\vec{\Omega} F(R, E, \vec{\Omega}) = \phi(E) ,$$

the scalar flux on the surface because the integral over $\vec{\Omega}$ is the inward half of the scalar flux at $\vec{\Omega}_0$, but this inward half covers all directions as the integral over $\vec{\Omega}_0$ is performed. Under this condition

$$A(E) = R^2 \int_{4\pi} d\vec{\Omega}_0 \int_{\vec{\Omega} \cdot \vec{\Omega}_0 < 0} d\vec{\Omega} F^+(E, -\vec{\Omega} \cdot \vec{\Omega}_0) F(R, E, \vec{\Omega}) (-\vec{\Omega} \cdot \vec{\Omega}_0)$$

but

$$\begin{aligned} \int_{4\pi} d\vec{\Omega}_0 (-\vec{\Omega}_0 \cdot \vec{\Omega}) F^+(E, -\vec{\Omega} \cdot \vec{\Omega}_0) &= \int_{\vec{\Omega} \cdot \vec{\Omega}_0 < 0} d\vec{\Omega} (-\vec{\Omega} \cdot \vec{\Omega}_0) F^+(E, -\vec{\Omega}_0 \cdot \vec{\Omega}) \\ &= -2\pi \int_{-1}^0 d\mu \mu F^+(E, \mu) \equiv 2\pi J^+(E) \end{aligned} \quad (\text{II.4})$$

independent of $\vec{\Omega}_0$ and $\vec{\Omega}$. It will be seen in a section that follows that J^+ is the adjoint current. Thus,

$$A(E) = 2\pi R^2 J^+(E) \int_{4\pi} d\vec{\Omega} F(R, E, \vec{\Omega}) = 2\pi R^2 J^+(E) \phi(E)$$

and by definition

$$\sigma_{LS}(E) = 2\pi R^2 J^+(E) \quad (\text{II.5})$$

We see then that if the incoming angular flux (no matter how anisotropic) is independent of position on the surface of the LS, A depends only on ϕ , therefore scalar flux is measured directly.

For illustration, consider the special case of a black sphere ($F^+(\mu)=1$, i.e., every neutron entering is absorbed) and a monoenergetic incident flux. For this example

$$\sigma_{LS} = -2\pi R^2 \int_{-1}^0 \mu d\mu = \pi R^2$$

leading to

$$A = \pi R^2 \phi .$$

This equation is clearly true for a monodirectional beam, of flux ϕ , for the black sphere will simply remove neutrons presented to its cross-sectional area. In the case of the black sphere immersed in an infinite isotropic bath of neutrons the number absorbed is the number crossing per unit area (the inward current $J^- = \phi/4$) multiplied by the surface area $4\pi R^2$.

If the angular flux incident on the LS varies slightly, then the average inward scalar flux $\bar{\phi}$ is approximately equal to the scalar flux that would be "at" the center of the sphere if all neutrons actually heading for the center from the surface reached it. The reason is that each point on the surface contributes only one direction to the flux

at the center, and together all the surface points give contributions from all possible directions. Besides, $F^+(E, \mu)$ is peaked at $\mu=1$ (see Figure 21), so that neutrons heading toward the center are heavily weighted in this measurement. Strong motivations for making the spectrometer as small as possible are that $\bar{\phi}$ becomes the scalar flux and that its presence does not alter the spectrum it is to measure.

We have considered only what the LS measures in terms of the flux at the surface in the presence of the sphere. In some cases this flux may not be different from that which is present when the sphere is removed, such as if the spectrometer were to be placed in free space far from other materials with which neutrons could interact. The spectrometer would thus be useful for measuring stray neutron fields outside of shields, critical assemblies, or in relatively large cavities within some systems. In some systems the spectrometer may be placed within a medium such as water and not distort the incident spectrum significantly. Thus it may be used within aqueous shields, without having to correct the spectrum obtained.

There are situations, however, in which the incident flux will be changed by the presence of the LS. In these instances, it might be possible to correct for the influence of the LS fairly easily, e.g. by considering the media as locally infinite (like the treatment of thermal flux

depression by foils) or if the geometry is spherically symmetric (such as including in test calculations the effects of placing an LS at the center of a large critical sphere^{St68}).

B. Determining the Spectrum from the Measurements

The results of the exposure of a set of M spectrometers is given by M integral equations of the form

$$A_m = \kappa \int \phi(E) \sigma_{LS}^m(E) dE \quad m=1,2,\dots,M \quad (\text{II.6})$$

where κ is a constant determined by the foil counting technique employed, and $\phi(E)$ is the flux for which the energy dependence is desired. One method of obtaining an appropriate expression for the flux is to parameterize an assumed function for it and then determine the parameters. This was done by using Bonner Leakage Spectrometers to obtain an expression for fission spectra of the form $(\sqrt{E} \exp-\alpha E)$. This form was substituted into II.6, which was then evaluated numerically to obtain α . Bonner performed measurements with spheres having different radii to verify the procedure. If the same α was obtained for each sphere, the method was considered valid. More general types of spectra would require more parameters. One method might be a multigroup analysis, in which the neutron flux is expressed as a sum of N group fluxes $\phi(E_n)$. A_m , the activity of the core for a particular spectrometer m, is

assumed to be given by

$$A_m = \kappa \sum_{n=1}^N \phi(E_n) \int_{\Delta E_n} \sigma_{LS}^m(E) dE \quad m=1,2,\dots,M \quad (\text{II.7})$$

or

$$\vec{A} = \kappa \underline{\Sigma} \vec{\phi} \quad (\text{II.8})$$

where $\underline{\Sigma}$ is an $M \times N$ matrix and \vec{A} and $\vec{\phi}$ are column vectors.

If this experiment is performed for $M(=N)$ different radius-foil combinations, the matrix equation II.8 becomes a set of simultaneous equations. The group fluxes can be solved for if the responses are linearly independent. A generalized form of II.8 can be obtained by assuming that the neutron spectrum is expressed by a sum of N linearly independent given functions $f_n(E)$,

$$\phi(E) = \sum_{n=1}^N a_n f_n(E) \quad (\text{II.9})$$

Since the number of detectors equals the number of activity equations, the N parameters a_n can be determined uniquely only if N is not greater than the number of detectors.

Equations like II.6 for bare foil activation have been solved by using iterative techniques.^{Mc67, Mc69} This procedure involves selection of an initial spectral approximation and its subsequent correction to obtain

a fit to the activation data. A least squares method has also been used with success to determine the coefficients a_n of II.9 by minimizing the quadratic form

$$Q = \sum_{m=1}^M \left[\frac{A_m - \kappa \sum_{n=1}^N a_n \int_0^{\infty} f_n(E) \sigma^m(E) dE}{A_m} \right]^2 \quad \text{Di65}$$

Gold^{Go64} has stated that, in general, the approximate solution should properly satisfy the set of integral equations II.6 and certain subsidiary conditions imposed by physical considerations (non-negativity, etc). A generalized formalism, which includes a controlled degree of smoothness or closeness to a given approximate solution for II.6, was introduced and coded by Routt^{Ro69}.

Calculations of responses for a set of spectrometers which lend themselves to the above methods for spectrum determination will now be described.

C. Method of Calculating Response Functions

This section will be devoted to the methods for determining $\sigma_{LS}(E)$, the function which, if multiplied by the "scalar" flux and integrated over energy, yields the saturated activity of the absorbing core of the LS. The connection between $F^+(E, \mu)$ from which $\sigma_{LS}(E)$ is generated, and the adjoint flux will be made. It will be seen how the adjoint flux is determined by the code ANISN^{En67} using a boundary condition and/or adjoint source.

The adjoint flux may be interpreted as follows.

Let \underline{H} , called the transport operator, be defined as

$$\begin{aligned} \underline{H}F &\equiv \vec{\Omega} \cdot \nabla F + \Sigma_t F - \int du' \int d\vec{\Omega}' F(\vec{r}, u, \vec{\Omega}) \Sigma_S(u' \rightarrow u; \vec{\Omega}' \cdot \vec{\Omega}) \\ &= S(\vec{r}, u, \vec{\Omega}) \end{aligned} \quad (\text{II.10})$$

where $F(\vec{r}, u, \vec{\Omega})$ is the angular flux as in II.1 with the change of variable $u = \ln E_0/E$ (u is called the neutron lethargy); E_0 is some reference energy (here $E_0 = 10^7$ eV). The first and third terms on the right hand side represent neutron gains to the phase space point $\vec{p} = (\vec{r}, u, \vec{\Omega})$ from streaming and scattering from higher energies respectively, and the second term represents removal from \vec{p} due to collisions. Σ 's are macroscopic cross sections, and $S(\vec{r}, u, \vec{\Omega})$ is an external source at \vec{p} . II.10 may be written in operator notation as

$$\underline{H}F = S \quad (\text{II.11})$$

F is uniquely determined by II.11 and specified boundary conditions.

Formally, the adjoint operator \underline{H}^+ is defined by

$$(F^+, \underline{H}F) = (\underline{H}^+ F^+, F) \quad (\text{II.12})$$

where F is any function obeying the boundary condition for the flux in II.11 and F^+ is any function obeying certain boundary conditions which make II.12 hold. Here the inner product, (f,g) is the integral,

$$(f,g) = \int f(\vec{p})g(\vec{p})d\vec{p} .$$

The normally present complex conjugation is absent because we are dealing with real functions.

Now we consider the particular "adjoint flux" F^+ satisfying $H^+F^+ = S^+$, and satisfying the boundary conditions of the general F^+ in II.12. The adjoint source S^+ can be chosen arbitrarily. When $S = (\vec{p}-\vec{p}_0)$, the Dirac delta-function, is substituted into II.12,

$$(F^+, \underline{H}F) = (F^+, S) = F^+(\vec{p}_0) .$$

Since

$$(\underline{H}F^+, F) = (S^+, F) ,$$

$$F^+(\vec{p}_0) = (S^+, F)$$

F is, however, the Green's function, i.e., the flux due to a unit source at \vec{p}_0 . Now if S^+ is taken to be the cross section for some physical process, then the adjoint

flux at \vec{p}_0 is seen to be just the rate at which the physical process represented by the cross section S^+ occurs throughout the system phase space when a unit source is introduced at \vec{p}_0 . Any cross section like quantity can be used for the adjoint source and each one will give rise to a distinct adjoint solution. Stated another way, the adjoint flux is the probability that a neutron at \vec{p}_0 will eventually lead to a process denoted by S^+ somewhere in the system phase space. Se69

With this interpretation of the adjoint flux it is clear that the function F^+ defined in section II.A is the adjoint flux for the process of being absorbed within the LS core material. We turn now to the calculation of the adjoint flux and from it, via II.4 and II.5, $\sigma_{LS}(E)$.

The code ANISN, a one dimensional multigroup discrete ordinate transport code, can be used to calculate the adjoint flux with some changes in the input data and the interpretation of the angular flux. For a more detailed discussion of the ANISN method for calculating direct flux see Ref. La63 and Tr68. Here we will summarize the development of the group equations for adjoint flux with the details left to Appendix A. II.12 is found to be satisfied if the adjoint operation is

$$\begin{aligned} \underline{H}^+ F^+ = & -\vec{\Omega} \cdot \nabla F^+ + \Sigma_t F^+ - \int d\vec{\Omega}' F^+(\vec{r}, u', \vec{\Omega}') \times \\ & \times \Sigma_S(u \rightarrow u'; \vec{\Omega} \cdot \vec{\Omega}') \end{aligned} \quad (\text{II.13})$$

with $F^+(\vec{r}, u, \vec{\Omega}) = 0$ for $\vec{\Omega} \cdot \vec{n} > 0$, where \vec{n} is the outward normal at the surface of the system. We first assume that the adjoint flux can be divided into G energy groups, with group g extending from u_g to u_{g+1} . Further, we assume that the groups are fine enough that the adjoint flux within each group may be taken as a constant whose value $F_g^+(\vec{r}, u)$ is given by

$$F_g^+(\vec{r}, \vec{\Omega}) = \int_{u_g}^{u_{g+1}} F^+(\vec{r}, u, \vec{\Omega}) du / \Delta u_g$$

where $\Delta u_g = u_{g+1} - u_g$. The group adjoint flux is defined in this manner so that when it is multiplied by the group flux $F_g(\vec{r}, \vec{\Omega})$ (interpreted as being the integral of $F(\vec{r}, u, \vec{\Omega})$ over u in group g) and integrated over $\vec{\Omega}_0$ and $\vec{\Omega}$ the saturated activity due to incident neutrons in g results.

$$A_g = \int_{u_g}^{u_{g+1}} du \int_{4\pi} d\vec{\Omega}_0 \int_{\vec{\Omega} \cdot \vec{\Omega}_0 < 0} d\vec{\Omega} F(\vec{R}, \vec{\Omega}_0, u, \vec{\Omega}) F^+(\vec{R}, u, -\vec{\Omega} \cdot \vec{\Omega}_0) (-\vec{\Omega} \cdot \vec{\Omega}_0)$$

$$A_g \approx \int_{4\pi} d\vec{\Omega}_0 \int_{\vec{\Omega} \cdot \vec{\Omega}_0 < 0} d\vec{\Omega} F_g(\vec{R}, \vec{\Omega}_0, \vec{\Omega}) F_g^+(\vec{R}, -\vec{\Omega} \cdot \vec{\Omega}_0) (-\vec{\Omega} \cdot \vec{\Omega}_0)$$

The total activity is then simply a sum over g

$$A = \sum_{g=1}^G A_g$$

If we approximate the scattering kernel by an L^{th} order Legendre expansion

$$\Sigma_S(u' \rightarrow u; \vec{\Omega}' \cdot \vec{\Omega}) = \sum_{\ell=0}^L \frac{2\ell+1}{4\pi} B_{\ell}(u' \rightarrow u) P_{\ell}(\mu_0)$$

then the adjoint kernel is

$$\Sigma_S(u \rightarrow u'; \vec{\Omega} \cdot \vec{\Omega}') = \sum_{\ell=0}^L \frac{2\ell+1}{4\pi} B_{\ell}(u \rightarrow u') P_{\ell}(\mu_0)$$

where μ_0 is the cosine of the angle between $\vec{\Omega}'$ and $\vec{\Omega}$, and B_{ℓ} are determined from cross section data (see Appendix C). If we apply the spherical harmonics addition theorem and partially perform the integration, the adjoint equation with spherical symmetry may be written as

$$\begin{aligned} & \left(-\mu \frac{\partial}{\partial r} - \frac{1-\mu^2}{r} \frac{\partial}{\partial \mu} + \Sigma_t(u) \right) F^+(r, u, \mu) \\ & - \sum_{\ell=0}^L \frac{2\ell+1}{2} P_{\ell}(\mu) \int_0^{\infty} du' B_{\ell}(u \rightarrow u') \int_{-1}^1 d\mu' P_{\ell}(\mu) F^+(r, u', \mu') \\ & = S^+(r, u, \mu) . \end{aligned} \tag{II.14}$$

Applying the operator

$$\frac{1}{\Delta u_g} \int_{u_g}^{u_{g+1}} du$$

to II.14 we obtain

$$\begin{aligned}
 & \left(-\mu \frac{\partial}{\partial r} - \frac{1-\mu^2}{r} \frac{\partial}{\partial \mu} + \Sigma_{tg} \right) F_g^+(r, \mu) \\
 & - \sum_{\ell} \frac{2\ell+1}{2} P_{\ell}(\mu) \int_{-1}^1 d\mu' P_{\ell}(\mu') \sum_{\substack{u_g \\ u_{g'}}}^{u_{g+1}} \int_{\substack{u_{g'+1} \\ u_{g'}}}^{u_{g'+1}} du' \times \\
 & \frac{B_{\ell}(u \rightarrow u')}{\Delta u_g} F^+(r, u', \mu') \\
 & = \int_{u_g}^{u_{g+1}} du S^+(r, u, \mu) / \Delta u_g \equiv S_g(r, \mu) \tag{II.15}
 \end{aligned}$$

Since $F_g^+(r, \mu')$ is independent of u in group g' ,

$$\begin{aligned}
 & \frac{1}{\Delta u_g} \int_{u_g}^{u_{g+1}} du \int_{u_{g'}}^{u_{g'+1}} du' B_{\ell}(u \rightarrow u') F^+(r, u', \mu') \\
 & = F_{g'}^+ \frac{1}{\Delta u_g} \int_{u_g}^{u_{g+1}} du \int_{u_{g'}}^{u_{g'+1}} du' B_{\ell}(u \rightarrow u') = B_{\ell}^{g \leftarrow g'} F_{g'}^+(r, \mu')
 \end{aligned}$$

where

$$B_{\ell}^{g \leftarrow g'} = \frac{1}{\Delta u_g} \int_{u_g}^{u_{g+1}} du \int_{u_{g'}}^{u_{g'+1}} du' B_{\ell}(u \rightarrow u') .$$

Thus, the scattering kernel for the adjoint problem is the

transpose of the kernel for the forward problem. The multi-group approximation to II.14 then becomes

$$\begin{aligned}
 & \left(-\mu \frac{\partial}{\partial r} - \frac{1-\mu^2}{r} \frac{\partial}{\partial \mu} + \Sigma_{tg} \right) F_g^+(r, \mu) \\
 & - \sum_{\ell=0}^L \sum_{g'=1}^G \frac{2\ell+1}{2} P_\ell(\mu) B_\ell^{g'+g} \int_{-1}^1 F_g^+(r, \mu') P_\ell(\mu') d\mu' \\
 & = S_g^+(r, \mu)
 \end{aligned} \tag{II.16}$$

Now if $-\mu$ is substituted for μ we obtain

$$\begin{aligned}
 & \left(\mu \frac{\partial}{\partial r} + \frac{1-\mu^2}{r} \frac{\partial}{\partial \mu} + \Sigma_{tg} \right) F_g^+(r, -\mu) \\
 & - \sum_{\ell=0}^L \sum_{g'=1}^G \frac{2\ell+1}{2} P_\ell(-\mu) B_\ell^{g'+g} \int_{-1}^1 d\mu' F_g^+(r, \mu') P_\ell(\mu') \\
 & = S_g(r, -\mu)
 \end{aligned} \tag{II.17}$$

But

$$\begin{aligned}
 & P_\ell(-\mu) \int_{-1}^1 d\mu' P_\ell(\mu') F_g^+(r, \mu') \\
 & = (-1)^\ell P_\ell(\mu) \int_{-1}^1 d\mu' P_\ell(\mu') (-1)^\ell F_g^+(r, -\mu') \\
 & = P_\ell(\mu) \int_{-1}^1 d\mu' P_\ell(\mu') F_g^+(r, -\mu') ,
 \end{aligned}$$

yielding

$$\begin{aligned}
 & \left(\mu \frac{\partial}{\partial r} + \frac{1-\mu^2}{r} \frac{\partial}{\partial \mu} + \Sigma_{tg} \right) F_g^+(r, -\mu) \\
 & - \sum_{\ell=0}^L \sum_{g'=1}^G \frac{2\ell+1}{2} P_\ell(\mu) B_\ell^{g' \leftarrow g} \int_{-1}^1 d\mu' P_\ell(\mu') F_g^+(r, -\mu') \\
 & = S_g^+(r, -\mu) \tag{II.18}
 \end{aligned}$$

which with the sign of μ changed in F_g^+ and S_g^+ and transposition of the scattering kernel is identical to the equation solved numerically for the direct flux $F_g(r, \mu)$. Because the quadrature angles μ_m for the S_N method to be used are chosen to be symmetric about $\mu=0$, the adjoint calculation of the leakage term proceeds as in the direct calculation; but input for the angular dependent source $S_g^+(r, \mu_m)$ is entered as $S_g(r, -\mu_m)$, and the resulting flux $F_g(r, \mu_m)$ is interpreted as the adjoint flux $F_g^+(r, -\mu_m)$. For example the boundary condition of no incoming flux in an adjoint problem is interpreted as a condition of no outgoing flux. In addition to transposing the scattering matrix, we reverse the group order of the cross sections, the source, and the starting flux guess. This inversion is convenient because the adjoint of a downscatter problem is an upscatter problem, which takes more time to compute. By proceeding in inverse group order, the upscatter problem becomes once more a downscatter problem.

Now if the macroscopic absorption cross section Σ_a of the core material is a smooth function of energy, the adjoint flux can be calculated accurately by means of the group adjoint source:

$$S_g^+(r) = \Sigma_{ag} H(R_{\text{core}} - r) = H(R_{\text{core}} - r) \int_{u_g}^{u_{g+1}} \frac{\Sigma_a(u) du}{\Delta u_g} \quad (\text{II.19})$$

where H is the Heavyside step-function and R_{core} is the core radius. This method is useful at high energies where the absorption cross section is slowly varying. At lower energies (1 to 1000eV) the cross section exhibits a resonance structure (the property we are trying to exploit) and to calculate adjoint flux reasonably accurately in this region would require an inordinately large number of groups. Because of the large cross section values within a resonance, the spatial mesh within the core would have to be extremely small to account for the very short mean free path. Tests (see Appendix B) have shown that calculations become unreliable when the mesh spacing becomes as large as a mean free path. Thus, some other method is required by computer space and time limitations.

If one considers the capture probability for neutrons entering the core, it is seen (Figure 9) that it is a more slowly varying function of energy than the resonance cross sections, so that its group averaged value will yield

more accurate results for the important low energy resonances. The idea here is to calculate the adjoint flux (capture probability) for a bare core and use the result as a boundary condition, leaving to the code the calculation of this adjoint flux through the cadmium, polyethylene and boron (if it is present). The advantage of this method is that one set of boundary conditions for a given core material may be used for many different polyethylene-boron configurations. This scheme neglects the probability of a neutron being absorbed in the core if it is heading out. It will be shown in Section D that this approximation does not result in any serious error.

The adjoint flux boundary condition is calculated on the basis of a first flight capture probability with a second flight correction term. Since an ANISN interpretation of the adjoint flux at a Legendre-Gauss quadrature angle

μ_m is

$$F^+(r, u, \mu_m) = \sum_{\ell=0}^L \frac{2\ell+1}{2} Q_{\ell}(r, u) P_{\ell}(\mu_m), \quad (\text{II.20})$$

it is desirable to expand the capture probability in Legendre polynomials to remain consistent. This is simple for the first flight capture probability $F_1^+(u_0, \mu)$, which is given

by

$$F_1^+(u_0, \mu) = \begin{cases} \frac{\Sigma_c(u_0)}{\Sigma_t(u_0)} (1 - e^{-2\mu R \Sigma_t(u_0)}) & \mu < 0 \\ 0 & \mu > 0 \end{cases}$$

where u_0 is the incident neutron lethargy, R is the core radius, μ is the cosine of the angle of the neutron with respect to the outward normal (see Figure 7), $\Sigma_t(u_0)$ is the total macroscopic cross section, and $\Sigma_c(u_0)$ is the macroscopic absorption cross section for a process which leads to a countable radioactive nucleus. The Legendre coefficient $Q_\ell(u_0)$ is given by

$$Q_\ell(u_0) = \int_{-1}^0 P_\ell(\mu) F_1^+(u_0, \mu) d\mu + \int_0^1 P_\ell(\mu) \cdot 0 d\mu$$

$$= \int_{-1}^0 P_\ell(\mu) \frac{\Sigma_c}{\Sigma_t} (1 - e^{-2\mu R \Sigma_t}) d\mu$$

Since $P_\ell(\mu) = \frac{P'_{\ell+1}(\mu) - P'_{\ell-1}(\mu)}{2\ell+1}$,

$$Q_\ell(u_0) = \int_{-1}^0 \frac{P'_{\ell+1}(\mu) - P'_{\ell-1}(\mu)}{2\ell+1} \frac{\Sigma_c}{\Sigma_t} (1 - e^{-2\mu \Sigma_t R}) d\mu.$$

Integrating by parts yields

$$Q_\ell(u_0) = \frac{P_{\ell+1}(\mu) - P_{\ell-1}(\mu)}{2\ell+1} \frac{\Sigma_c}{\Sigma_t} (1 - e^{-2\mu \Sigma_t R}) \Big|_{-1}^0$$

$$+ \frac{2\Sigma_t R}{2\ell+1} \frac{\Sigma_c}{\Sigma_t} \left[\int_{-1}^0 d\mu P_{\ell+1}(\mu) e^{-2\mu \Sigma_t R} - \int_{-1}^0 d\mu P_{\ell-1}(\mu) e^{-2\mu \Sigma_t R} \right].$$

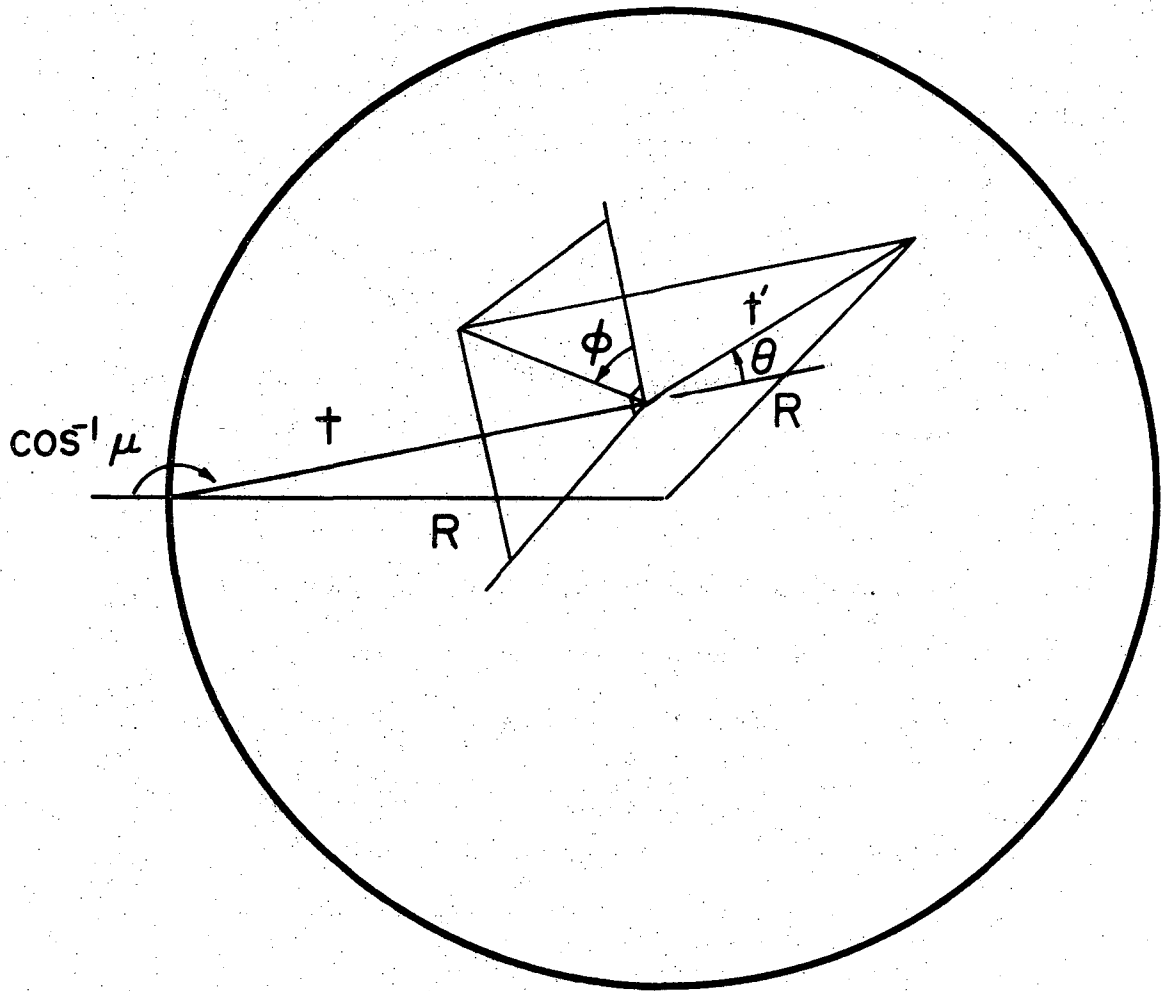


FIGURE 7. Geometry for Calculating Core Capture Probability. The center of the sphere and t are in the plane of the paper. The intersection of t and t' is the origin of a spherical coordinate system. θ and ϕ are the polar and azimuthal angles respectively.

The first term on the right hand side vanishes leaving

$$Q_{\ell}(u_0) = \frac{2\Sigma_t R}{2\ell+1} \left\{ Q_{\ell-1}(u_0) - Q_{\ell+1} + \frac{\Sigma_c}{\Sigma_t} \times \int_{-1}^0 d\mu [P_{\ell+1}(\mu) - P_{\ell-1}(\mu)] \right\}.$$

Solving for $Q_{\ell+1}$ gives

$$Q_{\ell+1}(u_0) = Q_{\ell-1}(u_0) - \frac{2\ell+1}{2\Sigma_t(u_0)} Q_{\ell}(u_0) + C_{\ell+1}(u_0) \quad (\text{II.21})$$

with

$$C_{\ell+1}(u_0) = \begin{cases} -\frac{\Sigma_c(u_0)}{\Sigma_t(u_0)} & \ell=1 \\ 0 & \ell \neq 1, \text{ odd} \\ \frac{\Sigma_c(u_0)}{\Sigma_t(u_0)} \frac{2\ell+1}{(\ell+2)(\ell)} P_{\ell-2}(0) & \ell \geq 2, \text{ even} \end{cases} \quad (\text{II.22})$$

$$Q_0(u_0) = \frac{\Sigma_c(u_0)}{\Sigma_t(u_0)} \left[1 + \frac{e^{-2R\Sigma_t(u_0)} - 1}{2R\Sigma_t(u_0)} \right] \quad (\text{II.23})$$

and

$$Q_1(u_0) = \frac{\Sigma_c(u_0)}{\Sigma_t(u_0)} \left[\frac{1}{(2R\Sigma_t(u_0))^2} - \frac{1}{2} - \frac{e^{-2R\Sigma_t(u_0)}}{2R\Sigma_t(u_0)} \times \left(1 + \frac{1}{2R\Sigma_t(u_0)} \right) \right] \quad (\text{II.24})$$

The recursion relationship for $Q_\ell(u_0)$ allows it to be numerically averaged over each group in the resonance region, and the first flight boundary condition to be generated with the help of II.20.

A second flight correction was added to account for slowing down within the core. This is given by

$$F_2^+(u_0, \mu) = \int_0^{2\mu R} dt \int_0^{2\pi} d\phi \int_0^\pi d\theta \Sigma_S(u_0) e^{-\Sigma_t(u_0)t} \times$$

$$\frac{\Sigma_c(u(\theta))}{\Sigma_t(u(\theta))} \left[1 - e^{-\Sigma_t(u(\theta))t'(\theta, \phi, t)} \right] \quad (\text{II.25})$$

where $\Sigma_S(u_0)$ is the scattering cross section; θ and ϕ determine the direction of the scattered neutron; and t' is the escape path for a neutron that scattered at t (see Figure 7):

$$t' = -\eta(t+R\mu) + R\cos\phi\sqrt{1-\eta^2}\sqrt{1-\mu^2} +$$

$$+ \sqrt{[\eta(t-R\mu-R\cos\phi(1-\mu))^{1/2}(1-\eta)^{1/2}]^2 - t(t-2R\mu)}$$

where $\eta = \cos\theta$. The secondary lethargy u is determined from kinematics of the scattering process as

$$u(\theta) = u_0 - \ln \left[\frac{A^2 + 2A\cos\theta + 1}{(A+1)^2} \right]$$

where A is the mass of the core material. It is assumed here that the lab and center of mass scattering angles are equal for heavy nuclei. F_2^+ was simply evaluated at each quadrature angle and added to the first flight contribution. Its effect was small (accounting for only 2.9% of the adjoint "source", see Figure 8), and expansion in Legendre polynomials would have required an additional numerical integration. The triple integral was evaluated using an eight point Gauss Legendre scheme and then averaged over lethargy according to Simpson's rule.

The boundary condition for the adjoint flux at the Gauss Legendre quadrature angles μ_m is thus

$$F_g^+(R_{\text{core}}, \mu_m) = \sum_{\ell=0}^L \frac{2\ell+1}{2} Q_{\ell g} P_{\ell}(\mu_m) + F_{2g}^+(R_{\text{core}}, \mu_m) \quad (\text{II.26})$$

where the subscript g implies an average over the g^{th} group and R_{core} is the core radius.

By means of a combination of this boundary condition at low energies and an absorption cross section adjoint source (II.19) at high energies the adjoint flux at the surface of the LS can be determined by the code ANISN.

D. Description of Input Data and Test Calculations

The group scheme for the calculation of $\sigma_{\text{LS}}(E)$ was chosen to be a 74-group structure. It was formed by collapsing the GAM^{Ad67} 99-group structure (Table 2) for which cross section libraries exist. The number of groups

TABLE 2

99-GROUP GAM STRUCTURE

GROUP BOUNDARIES									
	ENERGY-EV	LETHARGY	DELTA-E	DELTA-U		ENERGY-EV	LETHARGY	DELTA-E	DELTA-U
1	1.491825E+07	.400	1.419659E+06	.100	52	6.737947E+04	5.000	1.490429E+04	.250
2	1.349859E+07	.300	1.284560E+06	.100	53	5.247518E+04	5.250	1.160747E+04	.250
3	1.221403E+07	.200	1.162318E+06	.100	54	4.086771E+04	5.500	9.039906E+03	.250
4	1.105171E+07	.100	1.051709E+06	.100	55	3.182781E+04	5.750	7.040286E+03	.250
5	1.000000E+07	.000	9.516258E+05	.100	56	2.478752E+04	6.000	5.482980E+03	.250
6	9.048374E+06	.100	8.610666E+05	.100	57	1.930454E+04	6.250	4.270149E+03	.250
7	8.187308E+06	.200	7.791253E+05	.100	58	1.503439E+04	6.500	3.325596E+03	.250
8	7.408182E+06	.300	7.049817E+05	.100	59	1.170880E+04	6.750	2.589977E+03	.250
9	6.703200E+06	.400	6.378939E+05	.100	60	9.118820E+03	7.000	2.017076E+03	.250
10	6.065307E+06	.500	5.771902E+05	.100	61	7.101744E+03	7.250	1.570900E+03	.250
11	5.488116E+06	.600	5.222633E+05	.100	62	5.530844E+03	7.500	1.223418E+03	.250
12	4.965853E+06	.700	4.725634E+05	.100	63	4.307425E+03	7.750	9.527991E+02	.250
13	4.493290E+06	.800	4.275930E+05	.100	64	3.354626E+03	8.000	7.420407E+02	.250
14	4.065697E+06	.900	3.869022E+05	.100	65	2.612586E+03	8.250	5.779019E+02	.250
15	3.678794E+06	1.000	3.500836E+05	.100	66	2.034684E+03	8.500	4.500704E+02	.250
16	3.328711E+06	1.100	3.167687E+05	.100	67	1.584613E+03	8.750	3.505152E+02	.250
17	3.011942E+06	1.200	2.866242E+05	.100	68	1.234098E+03	9.000	2.729815E+02	.250
18	2.725318E+06	1.300	2.593483E+05	.100	69	9.611165E+02	9.250	2.125982E+02	.250
19	2.465970E+06	1.400	2.346680E+05	.100	70	7.485183E+02	9.500	1.655717E+02	.250
20	2.231302E+06	1.500	2.123364E+05	.100	71	5.829466E+02	9.750	1.289473E+02	.250
21	2.019965E+06	1.600	1.921299E+05	.100	72	4.539993E+02	10.000	1.004243E+02	.250
22	1.826835E+06	1.700	1.738464E+05	.100	73	3.535750E+02	10.250	7.821052E+01	.250
23	1.652989E+06	1.800	1.573027E+05	.100	74	2.753645E+02	10.500	6.091041E+01	.250
24	1.495686E+06	1.900	1.423334E+05	.100	75	2.144541E+02	10.750	4.743708E+01	.250
25	1.353353E+06	2.000	1.287885E+05	.100	76	1.670170E+02	11.000	3.694403E+01	.250
26	1.224564E+06	2.100	1.165327E+05	.100	77	1.300730E+02	11.250	2.877204E+01	.250
27	1.109032E+06	2.200	1.054431E+05	.100	78	1.013009E+02	11.500	2.240769E+01	.250
28	1.002588E+06	2.300	9.540890E+04	.100	79	7.889325E+01	11.750	1.745112E+01	.250
29	9.071795E+05	2.400	8.632955E+04	.100	80	6.144212E+01	12.000	1.359095E+01	.250
30	8.208500E+05	2.500	7.811420E+04	.100	81	4.785117E+01	12.250	1.058464E+01	.250
31	7.427358E+05	2.600	7.068065E+04	.100	82	3.726653E+01	12.500	8.243328E+00	.250
32	6.720551E+05	2.700	6.395450E+04	.100	83	2.902320E+01	12.750	6.419910E+00	.250
33	6.081066E+05	2.800	5.786830E+04	.100	84	2.260329E+01	13.000	4.999831E+00	.250
34	5.507322E+05	2.900	5.236152E+04	.100	85	1.760346E+01	13.250	3.893872E+00	.250
35	4.978707E+05	3.000	4.737866E+04	.100	86	1.370959E+01	13.500	3.032551E+00	.250
36	4.504920E+05	3.100	4.286998E+04	.100	87	1.067704E+01	13.750	2.361753E+00	.250
37	4.076220E+05	3.200	3.879037E+04	.100	88	8.315287E+00	14.000	1.839335E+00	.250
38	3.688317E+05	3.300	3.509897E+04	.100	89	6.475952E+00	14.250	1.432476E+00	.250
39	3.337327E+05	3.400	3.175887E+04	.100	90	5.043477E+00	14.500	1.115613E+00	.250
40	3.019738E+05	3.500	2.873661E+04	.100	91	3.927864E+00	14.750	8.688403E-01	.250
41	2.732372E+05	3.600	2.600196E+04	.100	92	3.059023E+00	15.000	6.766535E-01	.250
42	2.472353E+05	3.700	2.352755E+04	.100	93	2.382370E+00	15.250	5.269783E-01	.250
43	2.237077E+05	3.800	2.128860E+04	.100	94	1.855391E+00	15.500	4.104111E-01	.250
44	2.024191E+05	3.900	1.926273E+04	.100	95	1.444980E+00	15.750	3.196285E-01	.250
45	1.831564E+05	4.000	1.742963E+04	.100	96	1.125352E+00	16.000	2.489269E-01	.250
46	1.657268E+05	4.100	1.577099E+04	.100	97	8.764248E-01	16.250	1.938645E-01	.250
47	1.499558E+05	4.200	1.427018E+04	.100	98	6.825603E-01	16.500	1.509818E-01	.250
48	1.356856E+05	4.300	1.291219E+04	.100	99	5.315785E-01	16.750	1.175848E-01	.250
49	1.227734E+05	4.400	1.168343E+04	.100	100	4.139938E-01	17.000	8.129938E-01	6.026
50	1.110900E+05	4.500	2.457301E+04	.250	101	1.000000E-03	23.026		
51	8.651695E+04	4.750	1.913748E+04	.250					

was reduced in the interest of shortening computation time. Group 2 through 49 of width .1 lethargy units (1.u.) of the GAM-II structure were combined to form 24 groups of width .2 1.u.; the remaining 50 groups were left unchanged. The resulting scheme is given in Table 3. A cross section σ'_{xi} for the new group i was given by

$$\sigma'_{xi} = \frac{\sigma_{x,2i} + \sigma_{x,2i+1}}{2} \quad i=1, \dots, 24$$

$$\sigma'_{xi} = \sigma_{x,i+25} \quad i=25, \dots, 74$$

where x stands for either total or absorption. The expansion coefficients for the scattering kernel $B_{\ell}^{j+i'}$ was given by

$$B_{\ell}^{j+i'} = \frac{B_{\ell}^{2i+2i} + B_{\ell}^{2i+2i+1} + B_{\ell}^{2i+1+2i+1}}{2} \quad \begin{array}{l} i=j \\ i=1, \dots, 24 \end{array}$$

$$= \frac{B_{\ell}^{2j+2i} + B_{\ell}^{2j+1+2i} + B_{\ell}^{2j+2i+1} + B_{\ell}^{2j+1+2i+1}}{2}$$

$$= \frac{B_{\ell}^{j+25+2i} + B_{\ell}^{j+25+2i+1}}{2} \quad \begin{array}{l} i=1, \dots, 24 \\ j=25, \dots, 74 \end{array}$$

$$= B_{\ell}^{j+25+i+25} \quad \begin{array}{l} i=25, \dots, 74 \\ j=25, \dots, 74 \end{array}$$

Remember that in a downscatter problem

$$B_{\ell}^{j+i'} = 0 \quad j < i$$

TABLE 3

74-GROUP SCHEME USED FOR PRESENT CALCULATION

GROUP BOUNDARIES									
	ENERGY-EV	LETHARGY	DELTA-E	DELTA-U		ENERGY-EV	LETHARGY	DELTA-E	DELTA-U
1	1.349859E+07	-.300	2.446879E+06	.200	39	3.354626E+03	8.000	7.420407E+02	.250
2	1.105171E+07	-.100	2.003335E+06	.200	40	2.612586E+03	8.250	5.779019E+02	.250
3	9.048374E+06	.100	1.640192E+06	.200	41	2.034684E+03	8.500	4.500704E+02	.250
4	7.408182E+06	.300	1.342876E+06	.200	42	1.584613E+03	8.750	3.505152E+02	.250
5	6.065307E+06	.500	1.099454E+06	.200	43	1.234098E+03	9.000	2.729815E+02	.250
6	4.965853E+06	.700	9.001564E+05	.200	44	9.611165E+02	9.250	2.125982E+02	.250
7	4.065697E+06	.900	7.369858E+05	.200	45	7.485183E+02	9.500	1.655717E+02	.250
8	3.328711E+06	1.100	6.033929E+05	.200	46	5.829466E+02	9.750	1.289473E+02	.250
9	2.725318E+06	1.300	4.940163E+05	.200	47	4.539993E+02	10.000	1.004243E+02	.250
10	2.231302E+06	1.500	4.044664E+05	.200	48	3.535750E+02	10.250	7.821052E+01	.250
11	1.826835E+06	1.700	3.311490E+05	.200	49	2.753645E+02	10.500	6.091041E+01	.250
12	1.495686E+06	1.900	2.711219E+05	.200	50	2.144541E+02	10.750	4.743708E+01	.250
13	1.224564E+06	2.100	2.219758E+05	.200	51	1.670170E+02	11.000	3.694403E+01	.250
14	1.002588E+06	2.300	1.817385E+05	.200	52	1.300730E+02	11.250	2.877204E+01	.250
15	8.208500E+05	2.500	1.487949E+05	.200	53	1.013009E+02	11.500	2.240769E+01	.250
16	6.720551E+05	2.700	1.218229E+05	.200	54	7.889325E+01	11.750	1.745112E+01	.250
17	5.502322E+05	2.900	9.974018E+04	.200	55	6.144212E+01	12.000	1.359095E+01	.250
18	4.504920E+05	3.100	8.166035E+04	.200	56	4.785117E+01	12.250	1.058464E+01	.250
19	3.688317E+05	3.300	6.685784E+04	.200	57	3.726653E+01	12.500	8.243328E+00	.250
20	3.019738E+05	3.500	5.473857E+04	.200	58	2.902320E+01	12.750	6.419910E+00	.250
21	2.472353E+05	3.700	4.481615E+04	.200	59	2.260329E+01	13.000	4.999831E+00	.250
22	2.024191E+05	3.900	3.669236E+04	.200	60	1.760346E+01	13.250	3.893872E+00	.250
23	1.657268E+05	4.100	3.004116E+04	.200	61	1.370959E+01	13.500	3.032551E+00	.250
24	1.356856E+05	4.300	2.459562E+04	.200	62	1.067704E+01	13.750	2.361753E+00	.250
25	1.110900E+05	4.500	2.457301E+04	.250	63	8.315287E+00	14.000	1.839335E+00	.250
26	8.651695E+04	4.750	1.913748E+04	.250	64	6.475952E+00	14.250	1.432476E+00	.250
27	6.737947E+04	5.000	1.490429E+04	.250	65	5.043477E+00	14.500	1.115613E+00	.250
28	5.247518E+04	5.250	1.160747E+04	.250	66	3.927864E+00	14.750	8.688403E-01	.250
29	4.086771E+04	5.500	9.039906E+03	.250	67	3.059023E+00	15.000	6.766535E-01	.250
30	3.182781E+04	5.750	7.040286E+03	.250	68	2.382370E+00	15.250	5.269783E-01	.250
31	2.478752E+04	6.000	5.482980E+03	.250	69	1.855391E+00	15.500	4.104111E-01	.250
32	1.930454E+04	6.250	4.270149E+03	.250	70	1.444980E+00	15.750	3.196285E-01	.250
33	1.503439E+04	6.500	3.325596E+03	.250	71	1.125352E+00	16.000	2.489269E-01	.250
34	1.170880E+04	6.750	2.589977E+03	.250	72	8.764248E-01	16.250	1.938645E-01	.250
35	9.118820E+03	7.000	2.017076E+03	.250	73	6.825603E-01	16.500	1.509818E-01	.250
36	7.101744E+03	7.250	1.570900E+03	.250	74	5.315785E-01	16.750	1.175848E-01	.250
37	5.530844E+03	7.500	1.223418E+03	.250	75	4.139938E-01	17.000	4.129938E-01	6.026
38	4.307425E+03	7.750	9.527991E+02	.250	76	1.000000E-03	23.026		

Cross sections for hydrogen and carbon for the polyethylene were from the DLC-2 set.[†] Boron and cadmium cross-sections were from the "fast" library for the code GGC-4.^{††} These fine group sets were generated from energy dependent data by methods similar to those summarized in Appendix C. The specific gravity of the polyethylene (CH₂) was given by the manufacturer as .93, leading to an atom density of .04 atoms/cm³. The density of boron carbide (B₄C, the form of boron selected for design) was chosen equal to that which could be attained by packing B₄C powder (approximately 1/2 theoretical density) into a spherical shell surrounding the polyethylene (see Figure 5).

In what follows, a four character code (X,x,y,z) is followed for the structure of a given spectrometer. X is the core material, x is the core diameter in mm, y is the polyethylene diameter in inches, and z is the B₄C powder thickness (Δr) in inches (density assumed to be 1.40 grams/cm³). In all cases the cadmium thickness was 40 mil.

As can be seen in equations II.20-26, the total cross section $\Sigma_T(E)$, the scattering cross section $\Sigma_s(E)$, and an activation cross section $\Sigma_c(E)$ are required for the determination of the adjoint flux boundary condition at the polyethylene-core interface. The materials chosen for the core were natural indium, gold, and manganese. The most

[†] Obtained from the Radiation Shielding Information Center at Oak Ridge National Laboratory.

^{††} From the Argonne Code Center.

extensive calculations were performed for indium since they were partially tested experimentally (see Chapter III).

Natural indium consists of two isotopes ^{113}In and ^{115}In , with abundances 4% and 96% respectively. Resonance parameters ^{Go66}, from which the total and scattering cross sections for natural indium and the absorption cross section for ^{115}In can be calculated (Appendix C), have been determined for neutron energies up to 100 eV. When ^{115}In absorbs a neutron and the highly excited ^{116}In compound nucleus is formed, three possible final states of ^{116}In result from the γ -decay that follows. ^{Dr58, Do60, Po65} One is a conveniently counted 54 min isomeric state $^{116}\text{In}(m1)$, and the other two are the 14 sec ground state and a 2 second isomeric state $^{116}\text{In}(m2)$. The probability of being in the 54 min state depends upon the incident neutron energy and the J-value of the compound nucleus. This probability has been determined for thermal energies and the first three resonances (1.46, 3.86, and 9.12 eV). Over this range it is a constant p_0 except in the neighborhood of the 3.86 eV resonance where a minimum p_{II} is attained. The average value of this probability was found to be close to p_0 from resonance integral measurements. ^{Be63, Al65} Here it is somewhat arbitrarily assumed that

$$\Sigma_c(E) = \Sigma_{^{116}\text{In}(m1)}(E) = \Sigma_a^{^{116}\text{In}}(E) \left\{ p_0 - \frac{p_0 - p_{II}}{1 - \frac{4(E-3.86)^2}{\Gamma^2}} \right\} \quad (\text{II.27})$$

up to 10 keV, where Γ is the total width of the 3.86 resonance, and p_0 and p_{II} are .789 and .661 respectively. Using II.26-27 and the resonance parameters, the group average boundary condition $F_g^+(R_{core}, \mu)$ was calculated for a 4 mm diameter natural indium sphere for the energy groups between the cadmium cut-off and 61 eV. Above this energy accurate pointwise data were not available, and group average cross sections were used both as an adjoint source, as in II.19, or directly in II.26, to calculate the adjoint boundary condition. These two techniques gave the same results for $\sigma_{LS}(E)$ (to within .73%) and were therefore assumed to be equivalent. Considerable computation time was saved by using the adjoint boundary condition, so it was selected for most of the calculations.

From 61 eV to 10 keV the average cross sections needed were obtained from the "fast" library for the Code GGC-4, which were generated from average resonance parameters in a manner similar to that mentioned in Appendix C. Above 10 keV the cross section for the formation of $^{116}\text{In}(m1)$ and others needed have been measured.^{Go66} Fortunately, no such complications arise for gold and manganese: the (n, γ) process ends in the ground state of the compound nucleus, and the cross sections needed are available in evaluated form.[†] The methods used and the input data sources for the calculation of $F_g^+(R_{core}, \mu)$ are summarized

[†]From the ENDF/B (Evaluated Nuclear Data File) CSEWG.

in Table 4.

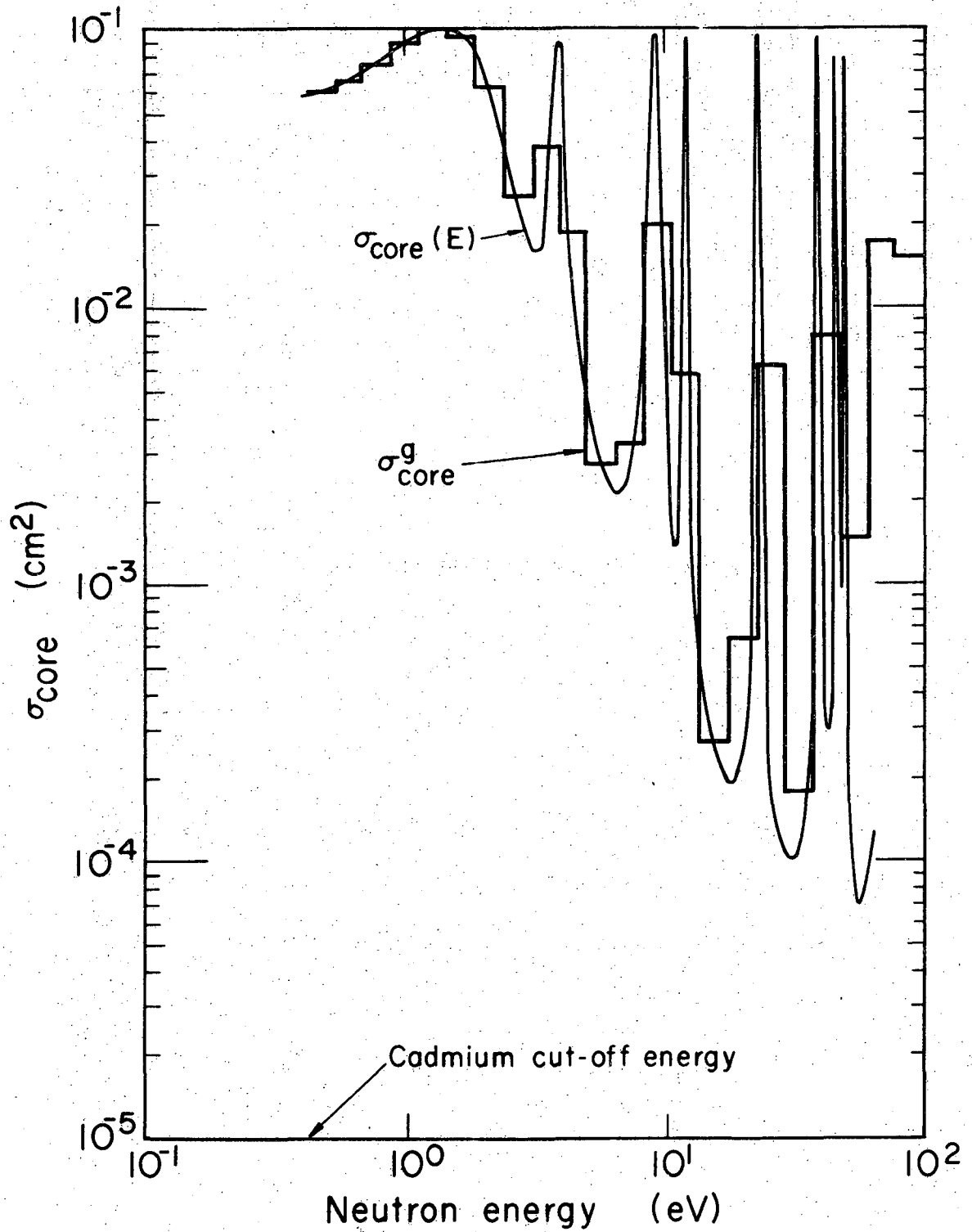
Results for σ_{core} (the core counterpart to σ_{LS} ; see II.4 and II.5) for indium are given in Figures 8 and 9. Included in Figure 8 is a plot of $\sigma_{\text{core}}(E)$ for comparison. It can be seen that the principal (1.45 eV) resonance is very well approximated by the group average value. This is important since this resonance accounts for 70% of the area under the curve and hence is the major contribution to the absorption probability. Figure 10 gives $F_g^+(\mu)$ for several groups. Here $F_g^+(\mu)$ is expanded in Legendre Polynomials up to order 7. The four angles for the ANISN boundary condition for an S8 (eighth order Gauss-Legendre Quadrature) approximation are indicated. It should be noted that the black core value is not 1.0 but .789 since only this fraction of the neutrons captured lead to the 54 min isomer of ^{116}In .

Tests of the code ANISN were made to determine mesh spacing, order of angular quadrature and order of the scattering kernel that would give good results. Several problems for which analytic solutions exist were run (see Appendix B), and these showed that a mesh spacing of 1/10 the shortest mean free path always gave accurate results for the spatial dependence. Calculations were performed for various quadrature and scattering-kernel orders to determine if the P-7 kernel available would be adequate. The smallest polyethylene sphere contemplated

TABLE 4

SUMMARY OF METHODS USED FOR ADJOINT SOURCE USED IN ANISN

Activation Process	Resonance Region $F_g^+ = \int_g F^+(E) dE$	Average Cross Sections Used
$\text{In}(n, \gamma) {}^{116}\text{In}(m1)$ 54 m	.4-61 eV cross sections from Go^{66} and Eq. II.27	Either F_g^+ from $\bar{\Sigma}_g^+$ (Eq. II.26) or $S_g^+ = \Sigma_{cg}^+$ (Eq. II.19) 61 eV - 10 keV "fast" data for GGC-4 and Eq. II.27 10 keV - 13.5 MeV average cross sections calculated from data in Go^{66} combined with "fast" data for GGC-4
${}^{197}\text{Au}(n, \gamma) {}^{198}\text{Au}$ 2.7 d	.4-960 eV recent eval- uation from ENDF/B file	960 eV - 13.5 MeV average cross sections from DLC-2 set (which was generated from ENDF/B data) used to calculate F_g^+ (Eq. II.26)
${}^{55}\text{Mn}(n, \gamma) {}^{56}\text{Mn}$ 2.56 h		.4 eV - 13.5 MeV same as for gold



XBL 7012-4209

FIGURE 8. Effective Cross Section of 4 mm Indium Core, from .1 to 100 eV. The superscript g denotes group average.

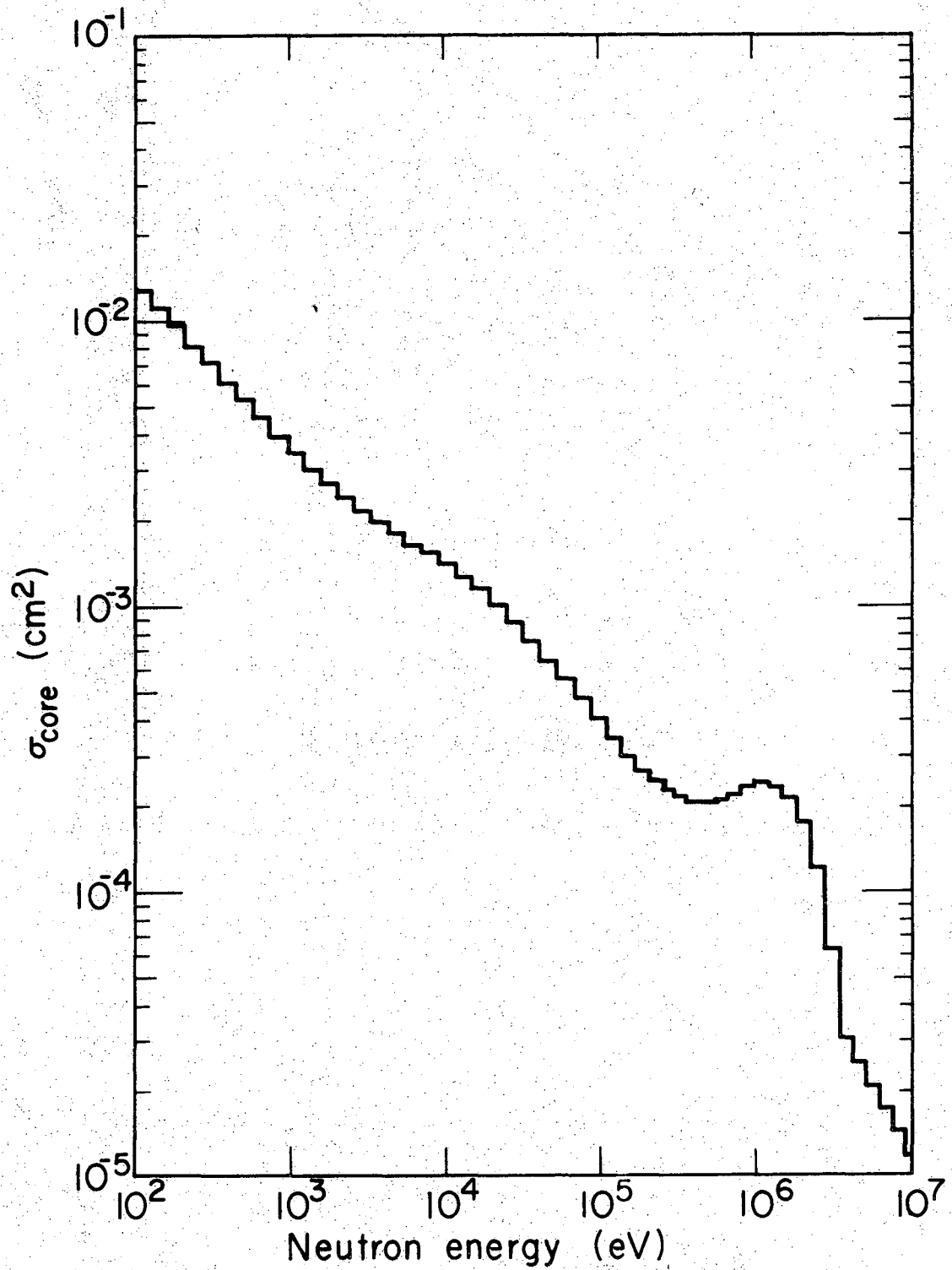


FIGURE 9. Effective Cross Section of a 4mm Diameter Indium Core, from 10^2 to 10^7 eV.

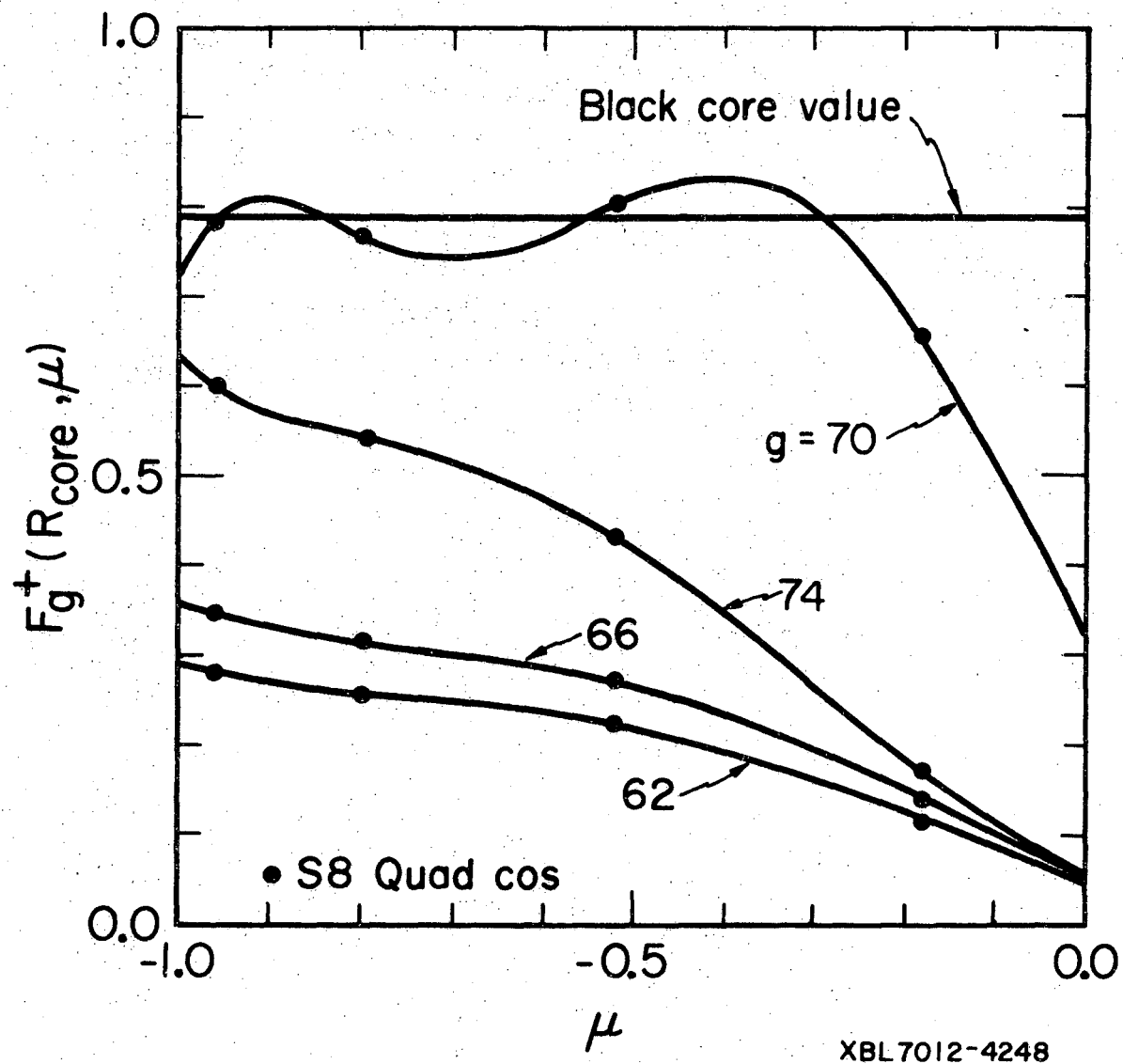
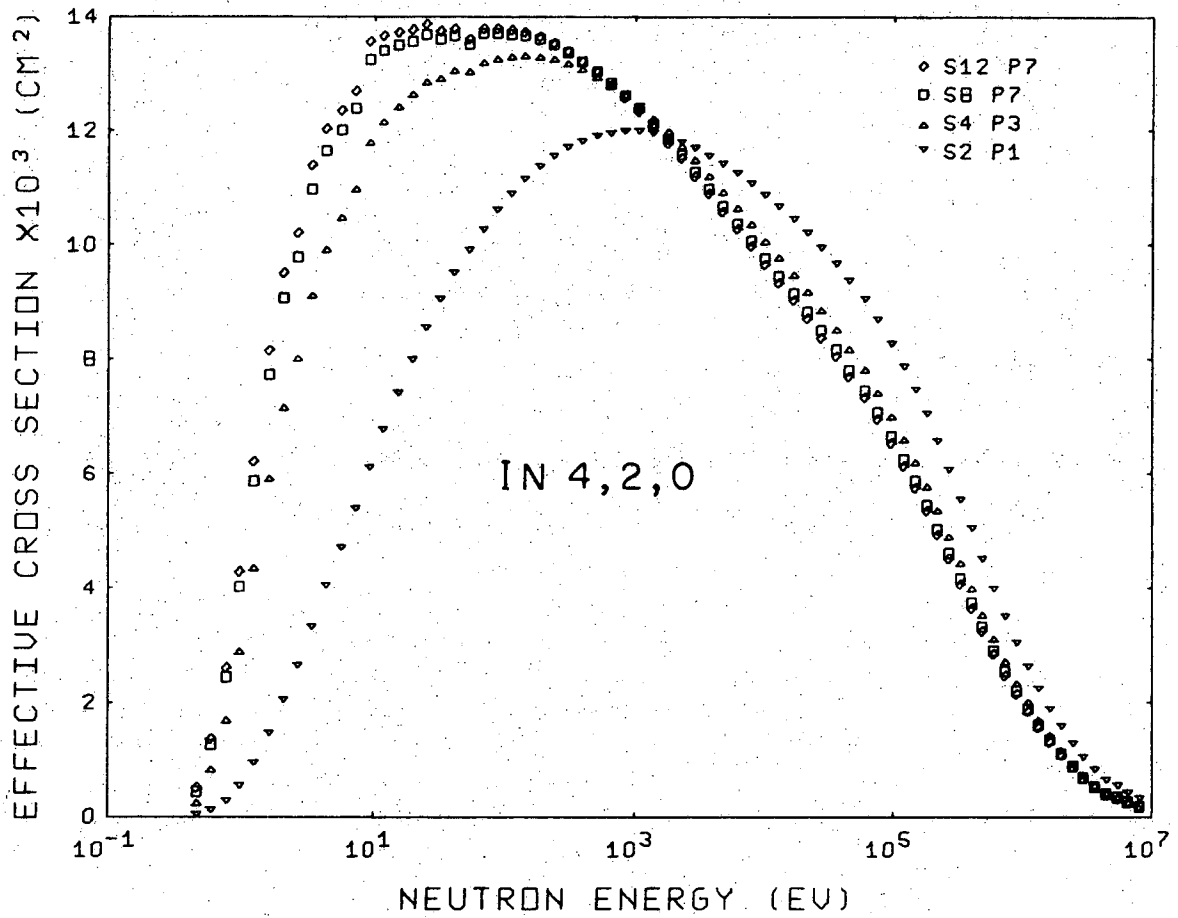


FIGURE 10. $F_g^+(R_{\text{core}}, \mu)$ for In Core for $g=62, 66, 70, 74$
(groups numbered as in Table 3)

(In 4,2,0) was chosen for consideration since it was thought to be the most sensitive.

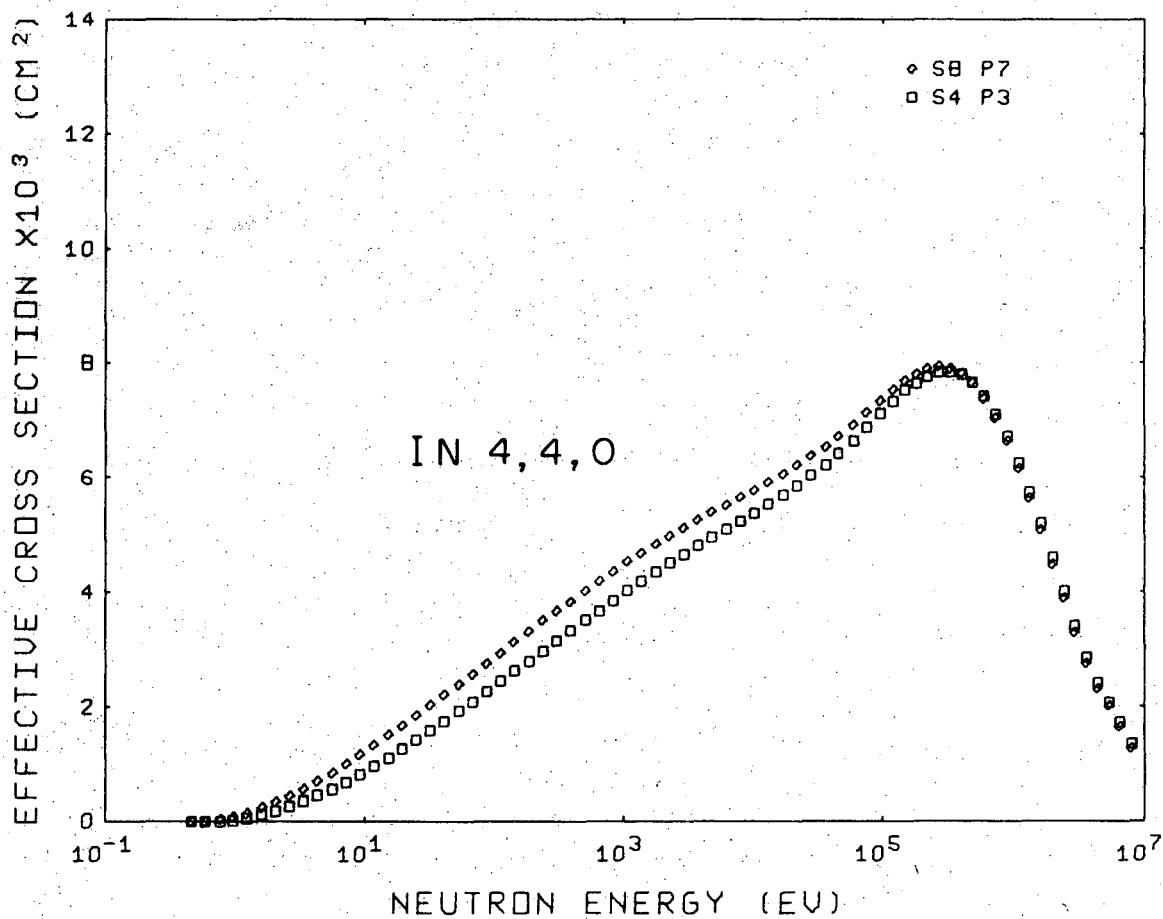
Results are given in Figure 11. As the order is increased, the peak response value increases and shifts to lower energy. The change between P-7 and P-3 is less than the change between P-3 and P-1, indicating that higher order terms will have a small effect. For the P-7 kernel the difference between S8 and S12 quadrature is small compared to the errors due to inaccuracies in the indium cross section. The variation for two larger spheres (In 4,4,0 and In 4,3,1) are given in Figures 12 and 13, which indeed show less change with increasing order. S8 P7 was chosen for the calculations.

An estimate of the error involved in neglecting the absorption probability for neutrons leaving the core was made by putting a unit outgoing source at the core radius at several different energies and allowing the code to calculate the flux returning to the core at all lower energies. By multiplying this flux by the first flight capture probability, an estimate of the number of absorptions was made. For the energies tested, the probability of capture for exiting neutrons was less than 1.1% of that for incident neutrons. This is to be expected since the hydrogen of the polyethylene is a forward scatterer, and neutrons either leak from the spectrometer or, if they do return, are slowed down below the cadmium cut-off.



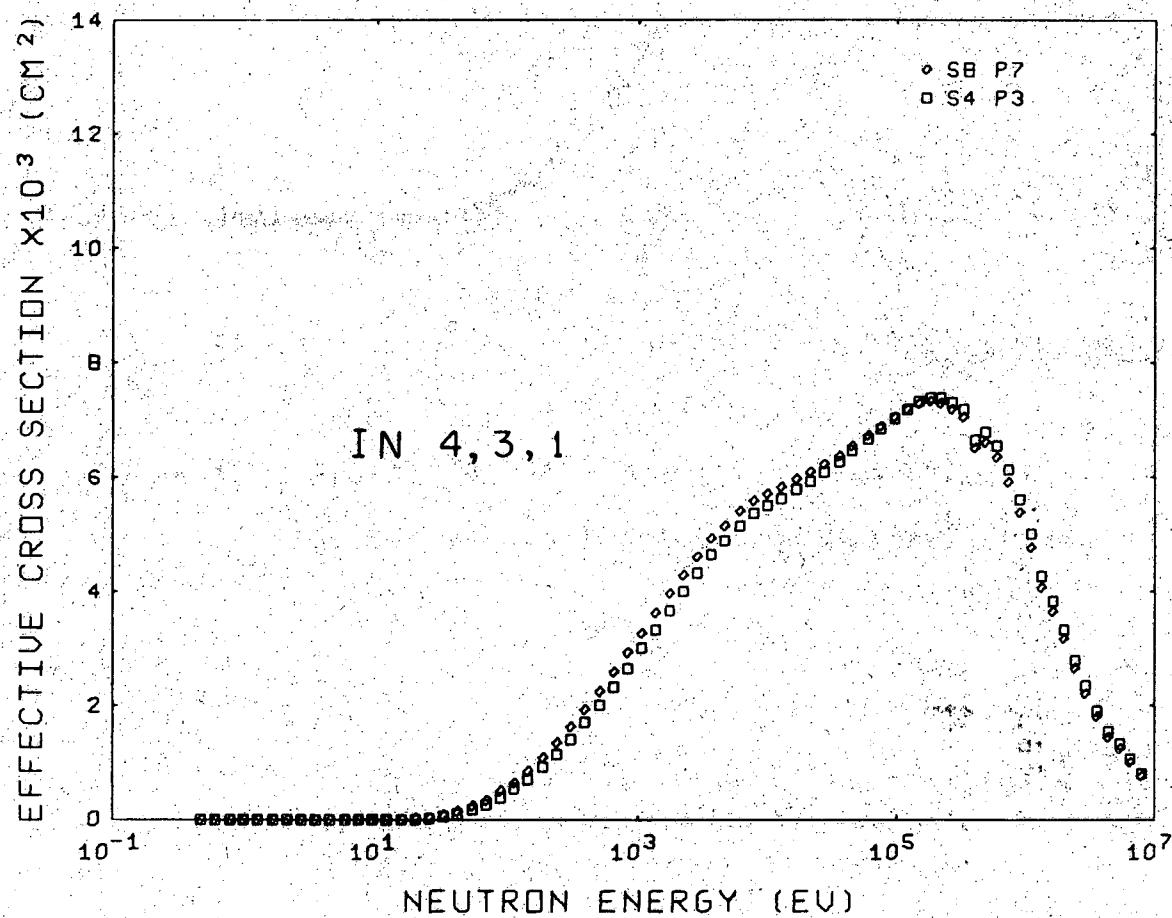
XBL7012-4190

FIGURE 11. $\sigma_{LS}(E)$ for In 4,2,0 for Several Combinations of Quadrature and Scattering-Kernel Order



XBL7012-4191

FIGURE 12. $\sigma_{LS}(E)$ for In 4,4,0 for Two Combinations of Quadrature and Scattering-Kernel Order



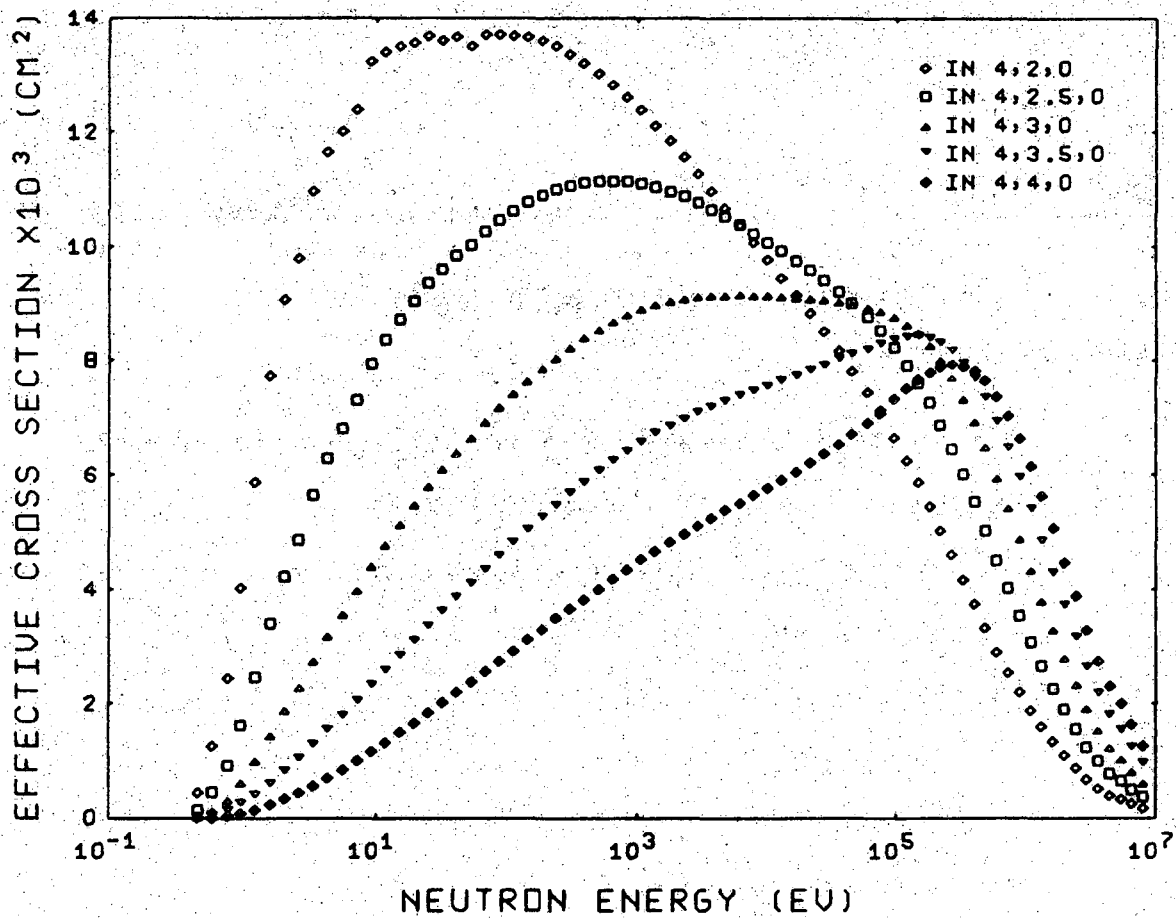
XBL7012-4192

FIGURE 13. $\sigma_{LS}(E)$ for In 4,3,1 for Two Combinations of Quadrature and Scattering-Kernel Order

E. Results

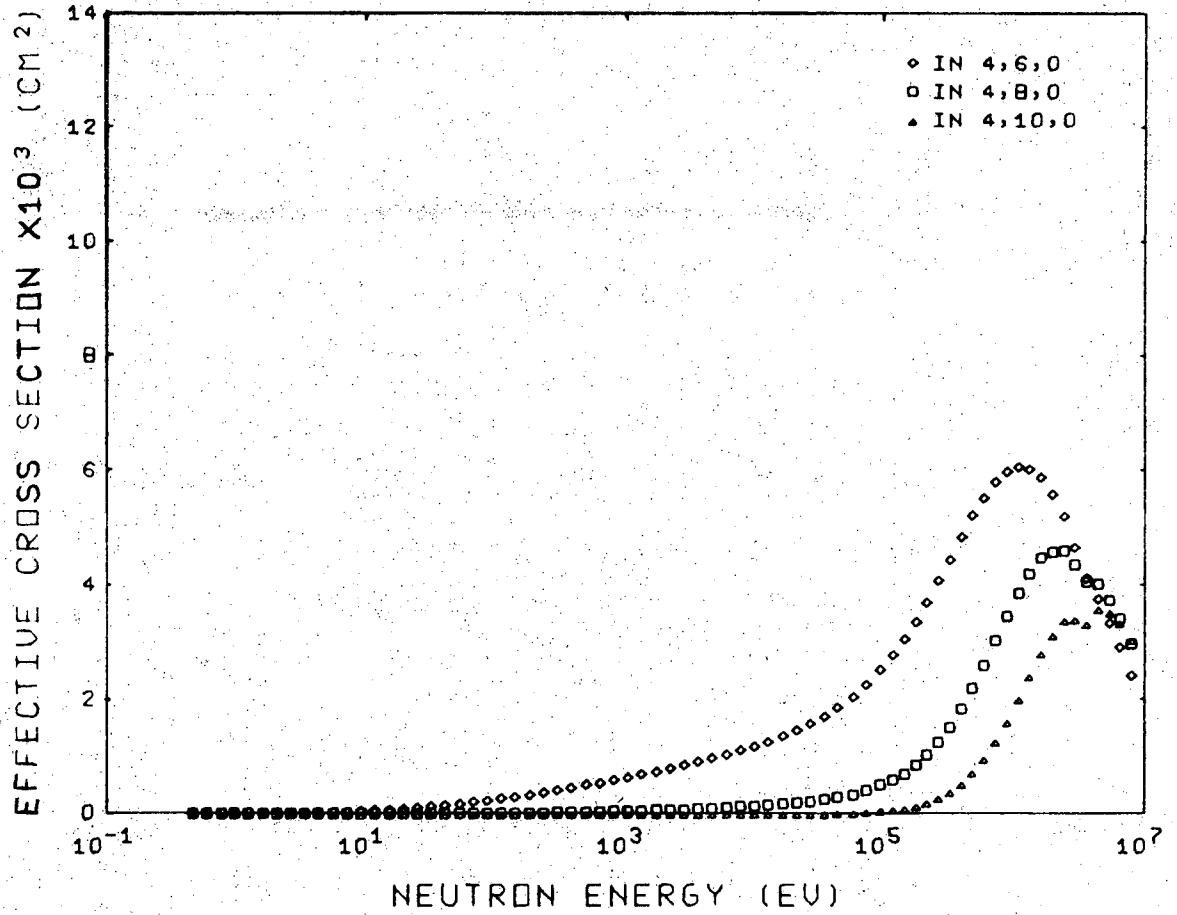
Calculations were performed for bare polyethylene for diameters varying from 2 inches to 10 inches; the results are given in Figures 14 and 15. It can be seen that response for the smaller spheres is extremely broad, several decades at half maximum. As the diameter is increased, the response first flattens, with the second derivative with respect to lethargy on the low energy side of the peak becoming less negative until at 4" the second derivative is almost zero. Further increase in diameter improves the resolution, and the second derivative becomes positive. The unevenness of $\sigma_{LS}(E)$ caused by the resonance structure of the core material for the 2" sphere becomes smoothed as polyethylene is added until it once again exhibits structure at 2 MeV due to resonances in the carbon cross section. It can also be seen that responses of high resolution are impossible to attain in the keV region.

In Figures 16-19 the results of calculations for various thicknesses of boron carbide powder are given. As with the modified Bonner spheres (Figure 4) the peak response is lowered in value and shifted to higher energy. The bare sphere response does not however form an envelope for the spheres with boron added as in Metha's curves. This is because the calculations here did not neglect the small but finite moderating ability of boron carbide (i.e., boron is not a pure absorber at high energy). The



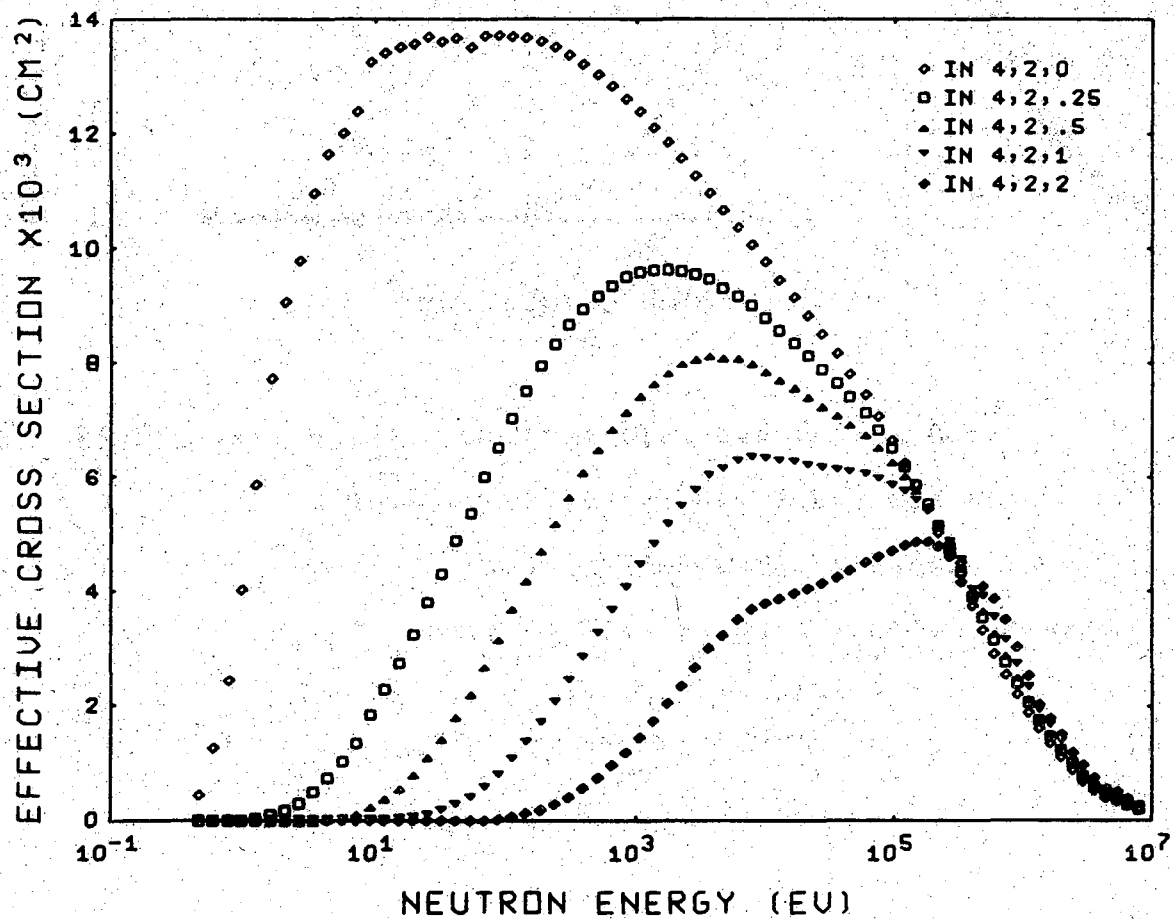
XBL7012 - 4184

FIGURE 14. $\sigma_{LS}(E)$ for 4 mm Diameter Indium Core
with Polyethylene Diameters Varying from
2-4 Inches



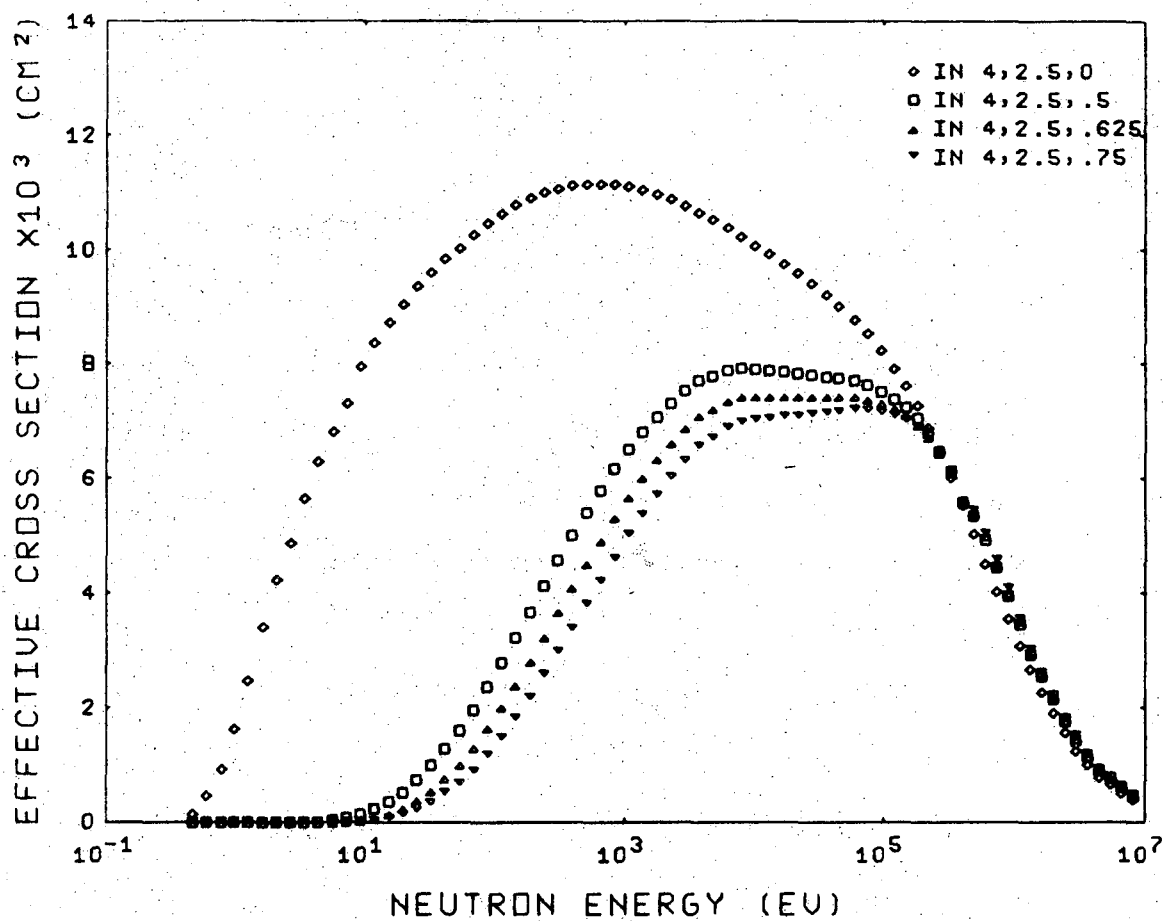
XBL7012-4195

FIGURE 15. $\sigma_{LS}(E)$ for 4 mm Diameter Indium Core
with Polyethylene Diameters Varying
from 6-10 Inches



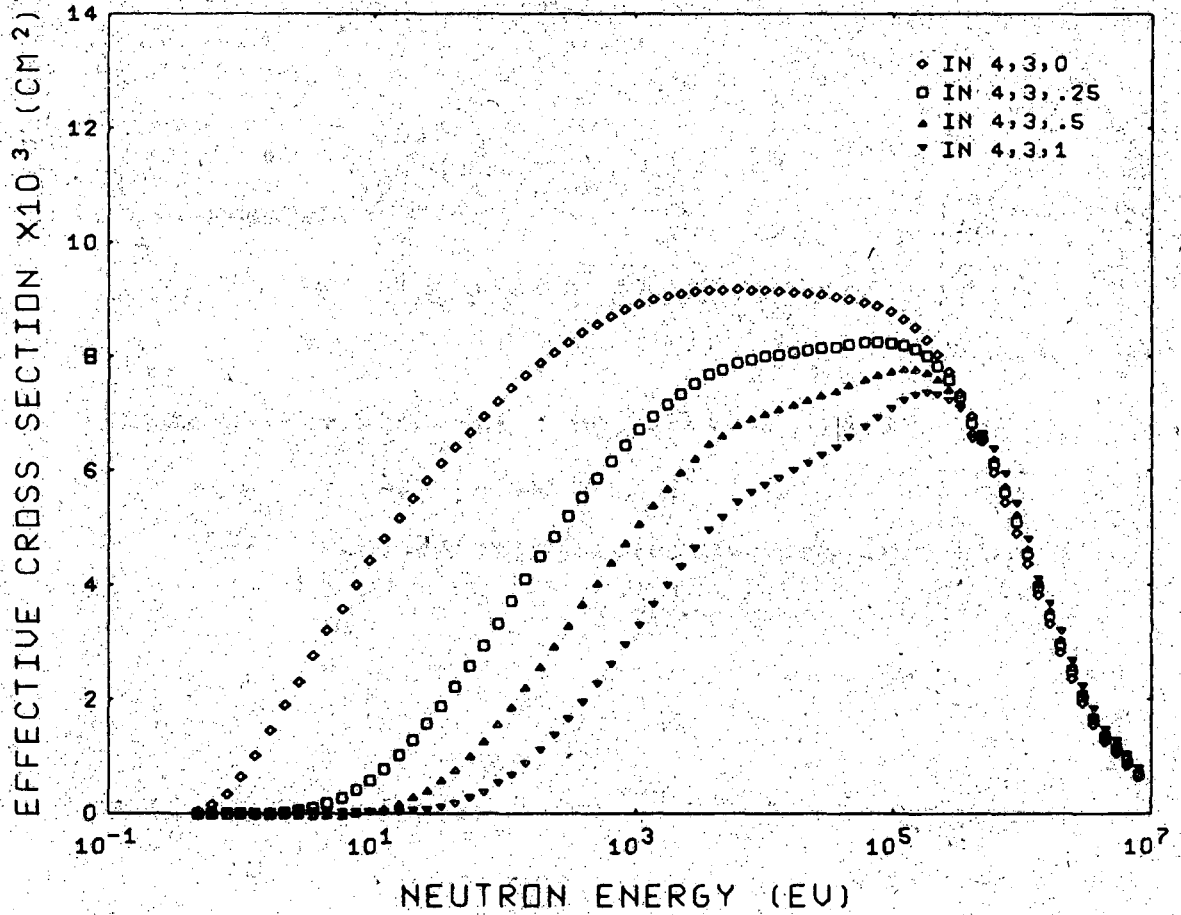
XBL 7012-7386

FIGURE 16. $\sigma_{LS}(E)$ for 4 mm Diameter Indium Core, 2 Inch Polyethylene Diameter, and Boron-Carbide Powder Thicknesses Varying from 0-2 Inches. .25, .5, 1, 2 Inches Correspond to .55, .97, 1.60, 3.74 gB/cm².



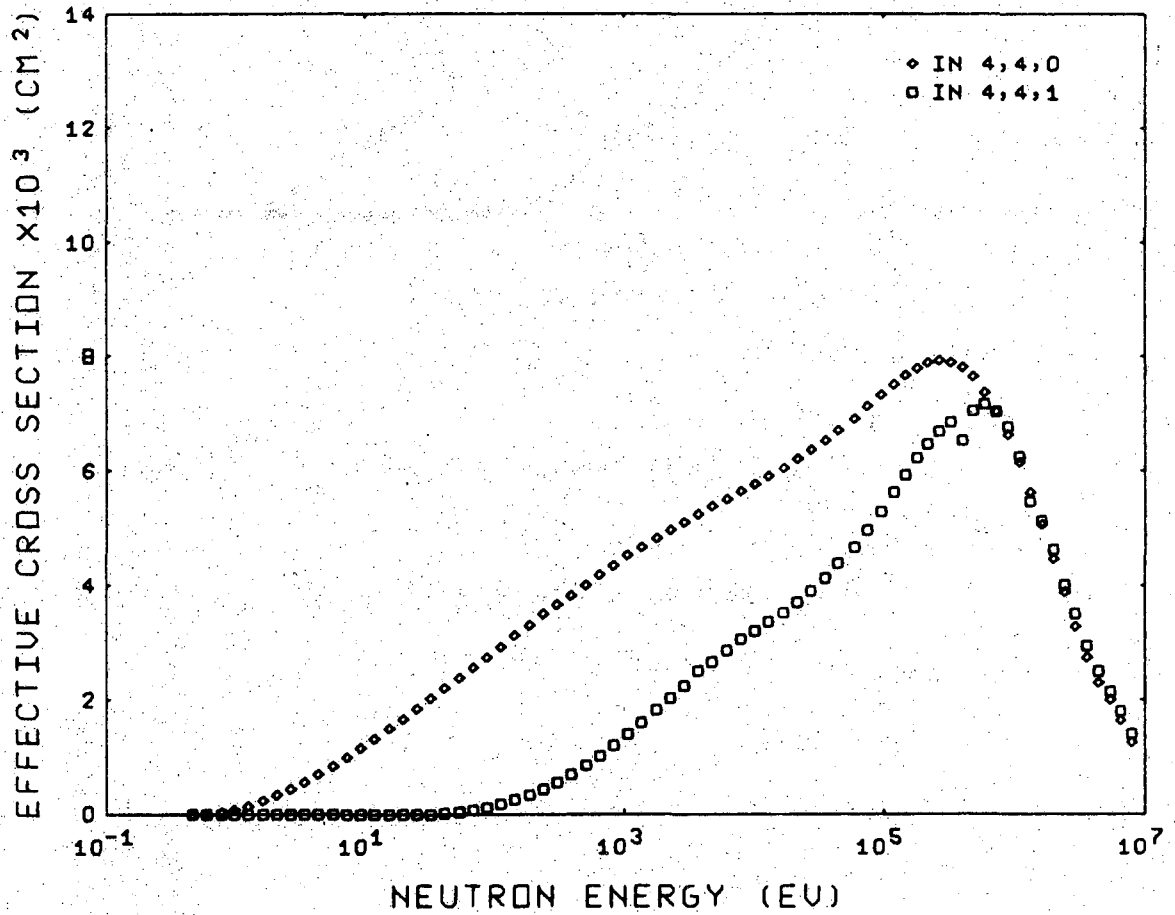
XBL7012-4186

FIGURE 17. $\sigma_{LS}(E)$ for 4 mm Diameter Indium Core, 2.5 Inch Polyethylene Diameter, and Boron-Carbide Powder Thicknesses Varying from 0-.75 Inches. .5, .625, .75 Inches Correspond to 1.04, 1.22, 1.40 gB/cm².



XBL7012-4187

FIGURE 18. $\sigma_{LS}(E)$ for 4 mm Diameter Indium Core,
 2 Inch Polyethylene Diameter, and Boron-
 Carbide Thicknesses Varying from 0-1 Inches
 .25, .5, 1 Inches Correspond to .60, 1.07,
 1.67 gB/cm².



XBL7012-4188

FIGURE 19. $\sigma_{LS}(E)$ for 4 mm Diameter Indium Core
 4 Inch Polyethylene Diameter, and Boron-
 Carbide Powder Thicknesses of 0 and 1 Inch.
 1 Inch corresponds to 1.96 gB/cm².

minimum (most evident in Figure 19) that occurs at about 500 keV for thicker boron shells is caused by a resonance in the boron cross section which scatters neutrons away from the sphere, decreasing the probability of penetrating to the core. The peak position for a given CH_2 diameter is not a simple function of the boron thickness, because of the complicated combination of scattering and absorption in the boron. Small changes in the thickness cause large changes in peak shape, making it difficult to place the maximum response where desired (see Figure 17).

Figure 20 shows $F_g(R_{LS}, \mu)$ for In 4,2,0. Of interest is the peaking at $\mu=-1$ and the lessening of this peak as energy increases. The results for a 4 mm indium core are summarized in Figure 21, where response maximum value, energy position, and resolution (full width at half maximum) are represented. From this figure, a set of spectrometers can be chosen according to the needs of the situation. One may, for instance, for a given peak position want to trade resolution for peak value or vice versa. This figure is intended to be used directly or to serve as a basis for interpolation for construction of spheres. For constructions using a form of boron other than B_4C powder, the thicknesses are given in gB/cm^2 in the figure captions.

Responses were also calculated for a 4 mm gold absorber, and the results are given in Figures 22 and 23. The shapes are similar to those of indium, as expected, since the

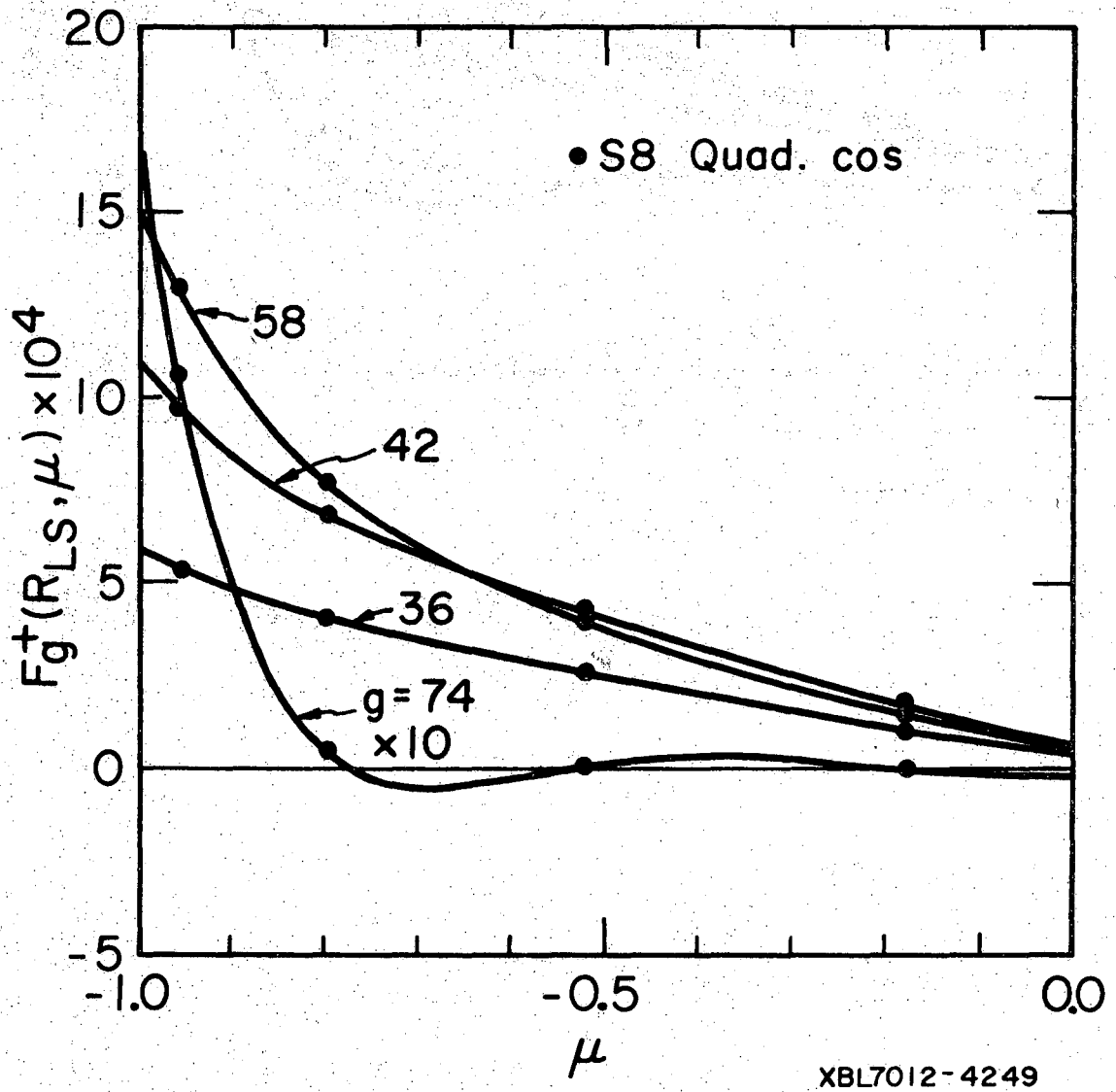


FIGURE 20. $F_g^+(R_{LS}, \mu)$ for In 4,2,0 for $g=36,42,58$ and 74 (groups numbered as in Table 3)

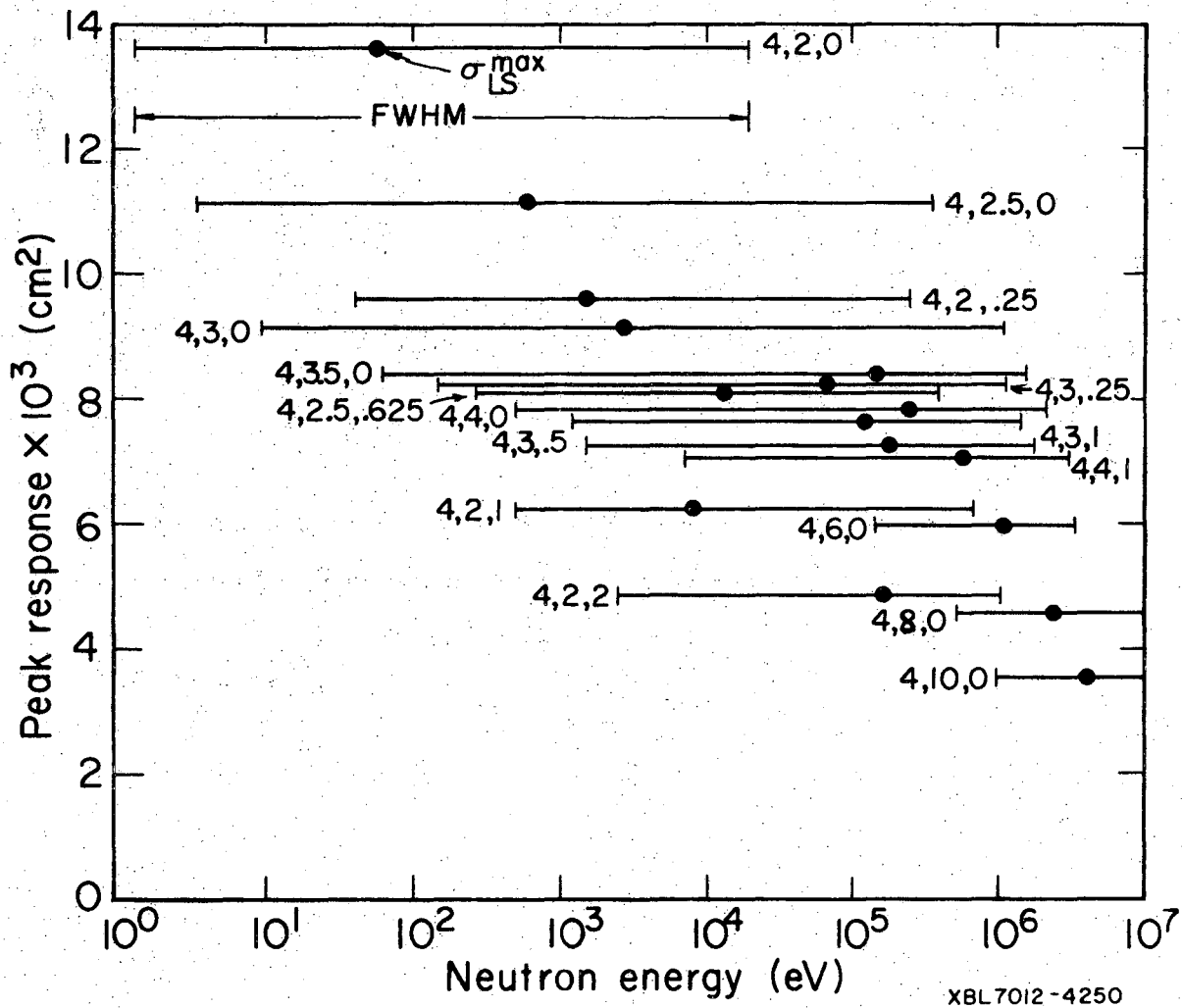
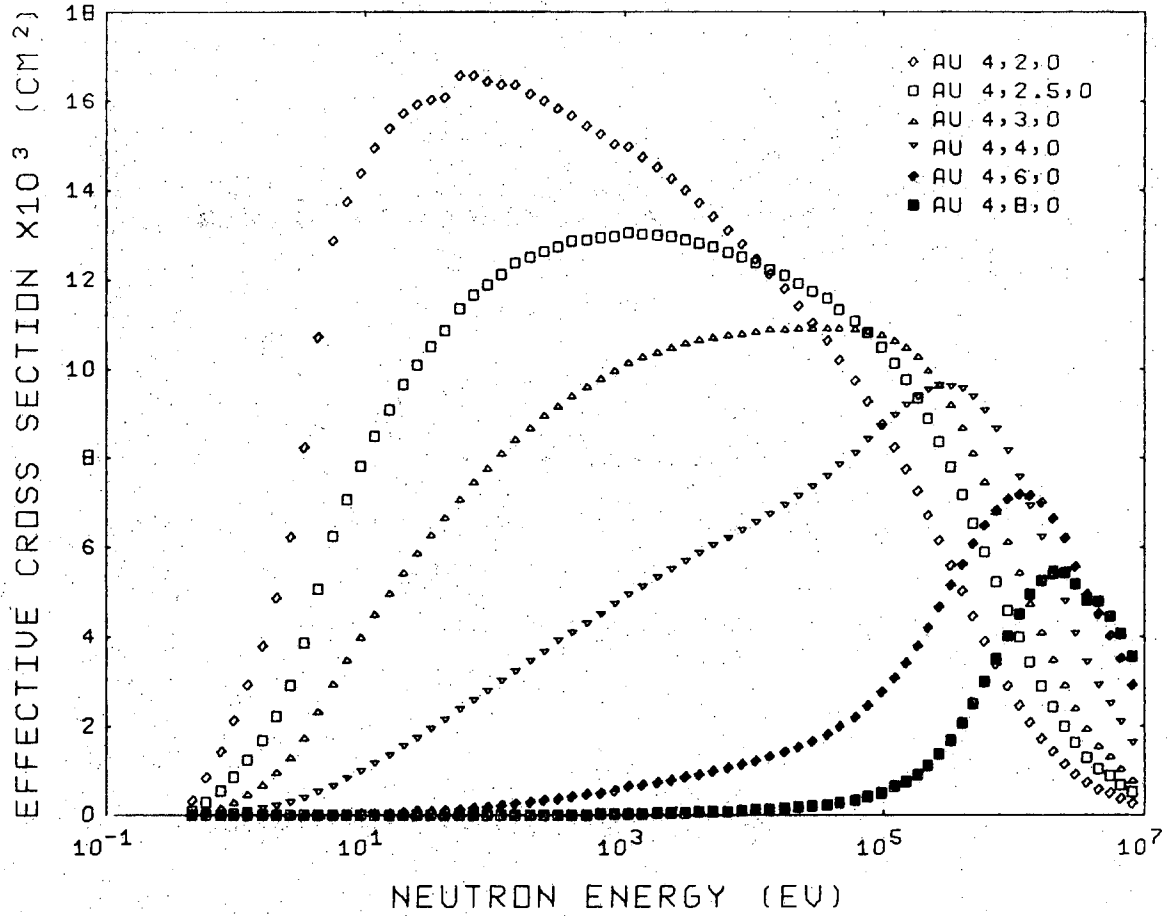
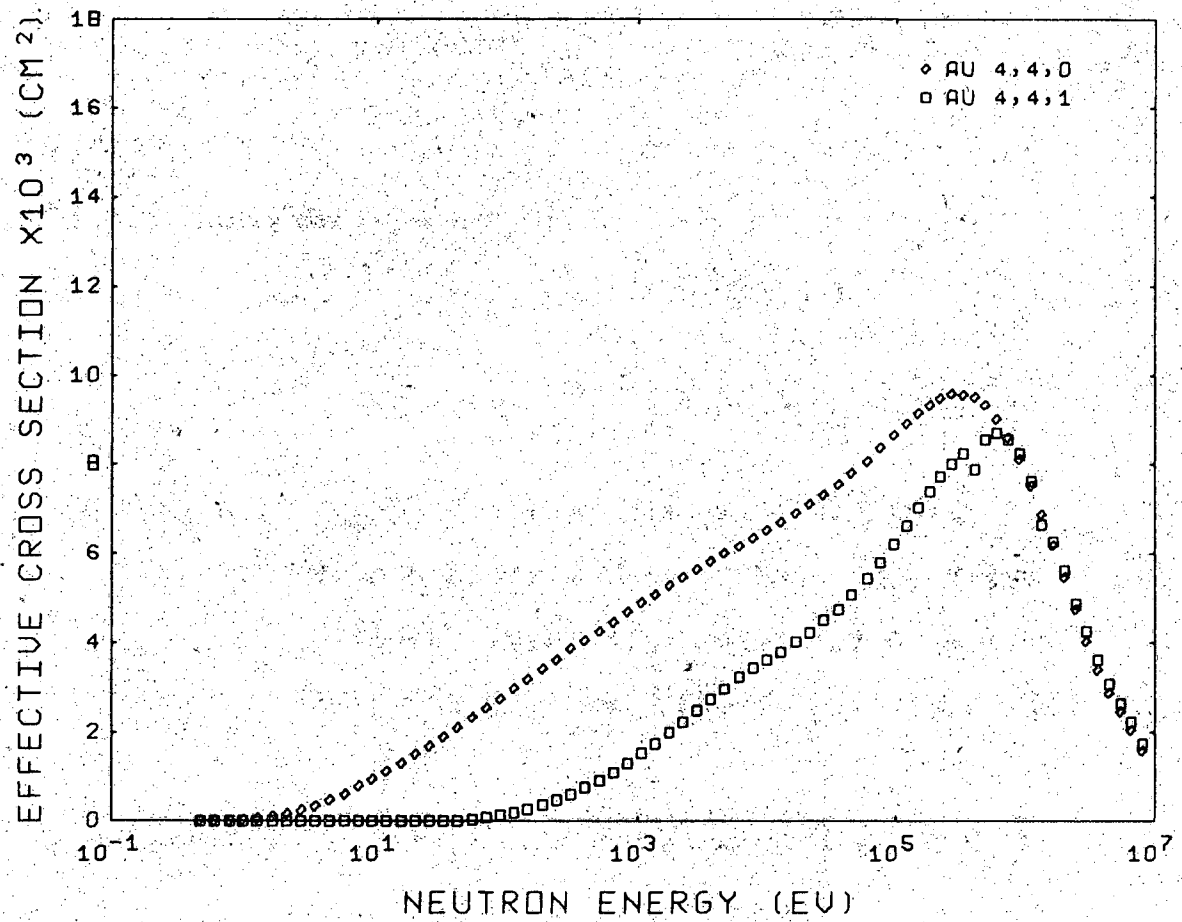


FIGURE 21. Peak Response Position and Resolution for LS's with 4 mm Diameter Indium Cores as a Function of Energy



XBL7012-4189

FIGURE 22. $\sigma_{LS}(E)$ for 4 mm Diameter Gold Core
and Polyethylene Diameters Varying from
2-8 Inches

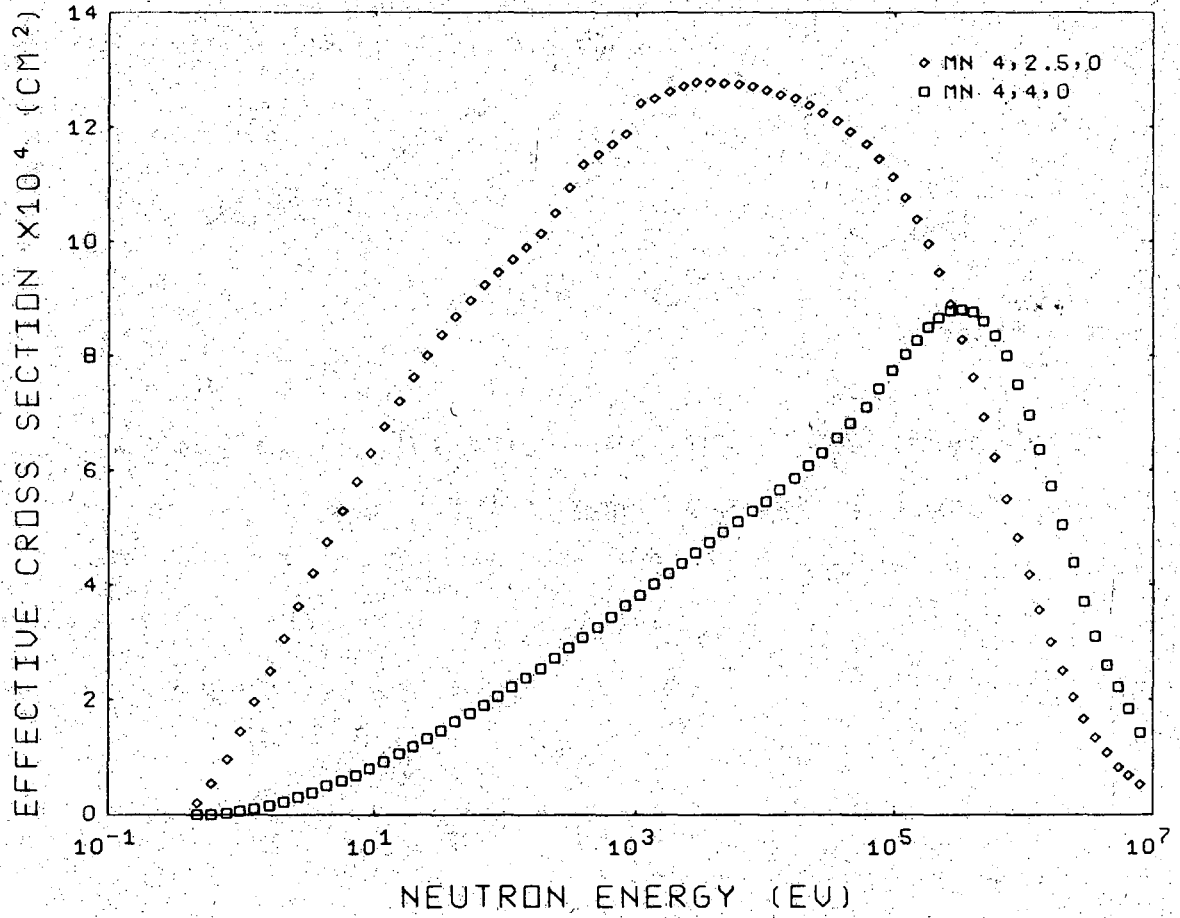


XBL7012-4194

FIGURE 23. $\sigma_{LS}(E)$ for 4 mm Diameter Gold Core,
 4 Inch Polyethylene Diameter and Boron-
 Carbide Powder Thicknesses of 0 and 1
 Inch. 1 Inch Corresponds to 1.96 g/cm².

major contribution to the capture is the 4.91 eV resonance, which is only 3.4 eV from the principal indium resonance. The responses are about 20% higher for all energies because, as mentioned above, all captures lead to activation compared to 78.9% for indium. Indium has the advantage of reaching saturation more quickly (half-life of 54 min compared to 2.7 d for gold); hence, for a given flux, better counting statistics can be obtained in a short time. Gold is superior in that it need not be counted immediately after irradiation. Its cross sections have also been evaluated in more detail and are therefore more reliable.

$\sigma_{LS}(E)$ was also determined for two spheres with a 4 mm core of manganese, which has its first resonance at 337 eV (results in Fig. 24). The response for the larger sphere (Mn 4,4,0) was similar to that of the indium core and shifted only slightly to higher energy for the 2.5 inch diameter sphere. Because the resonances of ^{55}Mn are largely scattering (the resonance integral as defined in Eq. I.1 is only 15 barns, of which 5.7 barns is $1/v$), and the $1/v$ variation from 337 eV down to the cadmium cut-off, a large portion of the absorption takes place at low energy (below the 337 eV resonance); hence, the small shifts in response compared to In. In view of the above and the fact that the responses for a manganese core are almost an order of magnitude lower, it would be better



XBL7012-4193

FIGURE 24. $\sigma_{LS}(E)$, for 4 mm Diameter Manganese Core
and Polyethylene Diameters 2.5 and 4 Inches

to choose a polyethylene-boron configuration with a gold or indium core and the same shape.

III. EXPERIMENT

A. Apparatus and Experimental Results

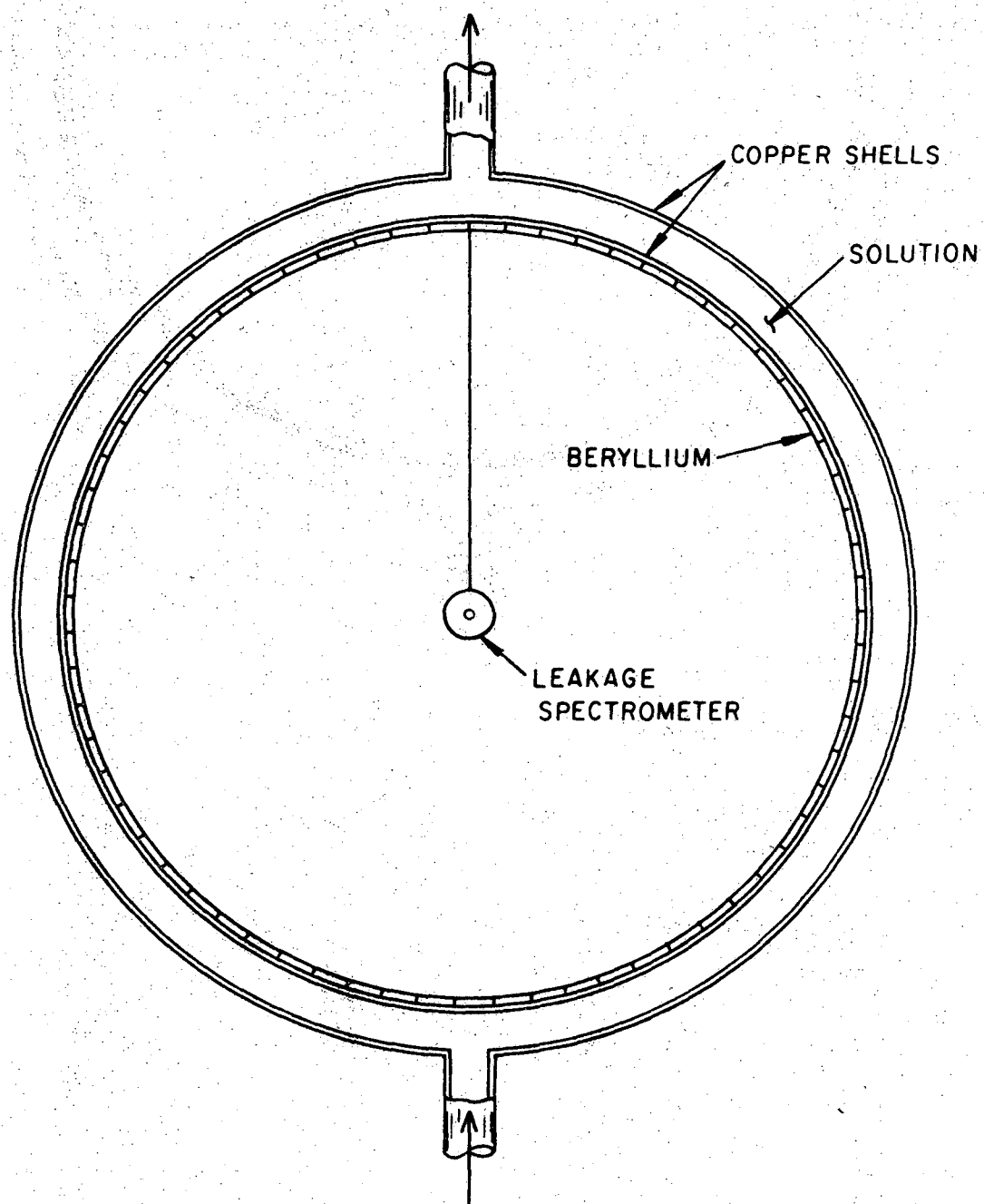
In this section we summarize the work of S. Binney,^{B170} who performed an experiment to calibrate and check the calculations of four leakage spectrometers (In 4,2,0; In 4,2,1; In 4,4,0; and In 4,3,1). Results of the experiment are given, and in the section that follows they are compared to the theoretical results of Chapter II.

The calibration of the Leakage Spectrometers (LS's) was carried out with neutrons from the $^9\text{Be}(\gamma, n)$ reaction, whose threshold is 1.665 MeV. With the proper choice of activated isotopes - to produce the gammas - neutrons with keV energies were produced. The isotopes that were activated for gamma emission are listed in Table 5, showing the neutron energies obtained. Salts of the material to be activated were dissolved in water and pumped through a container next to the core of the UC TRIGA Mark III research reactor. The container was part of a continuous flow loop. At the other end of the loop, the activated solution flowed between concentric spherical copper shells (see Figure 25), 18 and 20 inches in diameter respectively. The liquid between the shells constituted the gamma ray source, producing neutrons through the irradiation of a beryllium shell inside the inner copper shell. The beryllium target "sphere" was constructed by epoxying many small flat beryllium sheets (1/16" thick) to the inside of the copper

TABLE 5
NEUTRON SOURCE DATA

Isotope	Compound for Solution	i	Gamma Energy	$\sigma_{\gamma n_L}$ mb	Gamma Fraction F_i	Neutron Energy E_{Si}
Al-28	$Al_2(SO_4)_3$		1.78MeV	0.88	1.00	102keV
Mn-56	$Mn(SO_4)$	1	1.811MeV	0.74	.291	130keV
		2	2.110MeV	0.41	.15	395keV
In-116	$In_2(SO_4)_3$	1	1.753MeV	1.03	.015	78keV
		2	2.110MeV	0.41	.195	396keV
Sb-124*			1.692MeV	1.262	.46	24keV

* A solid source was used in this case.

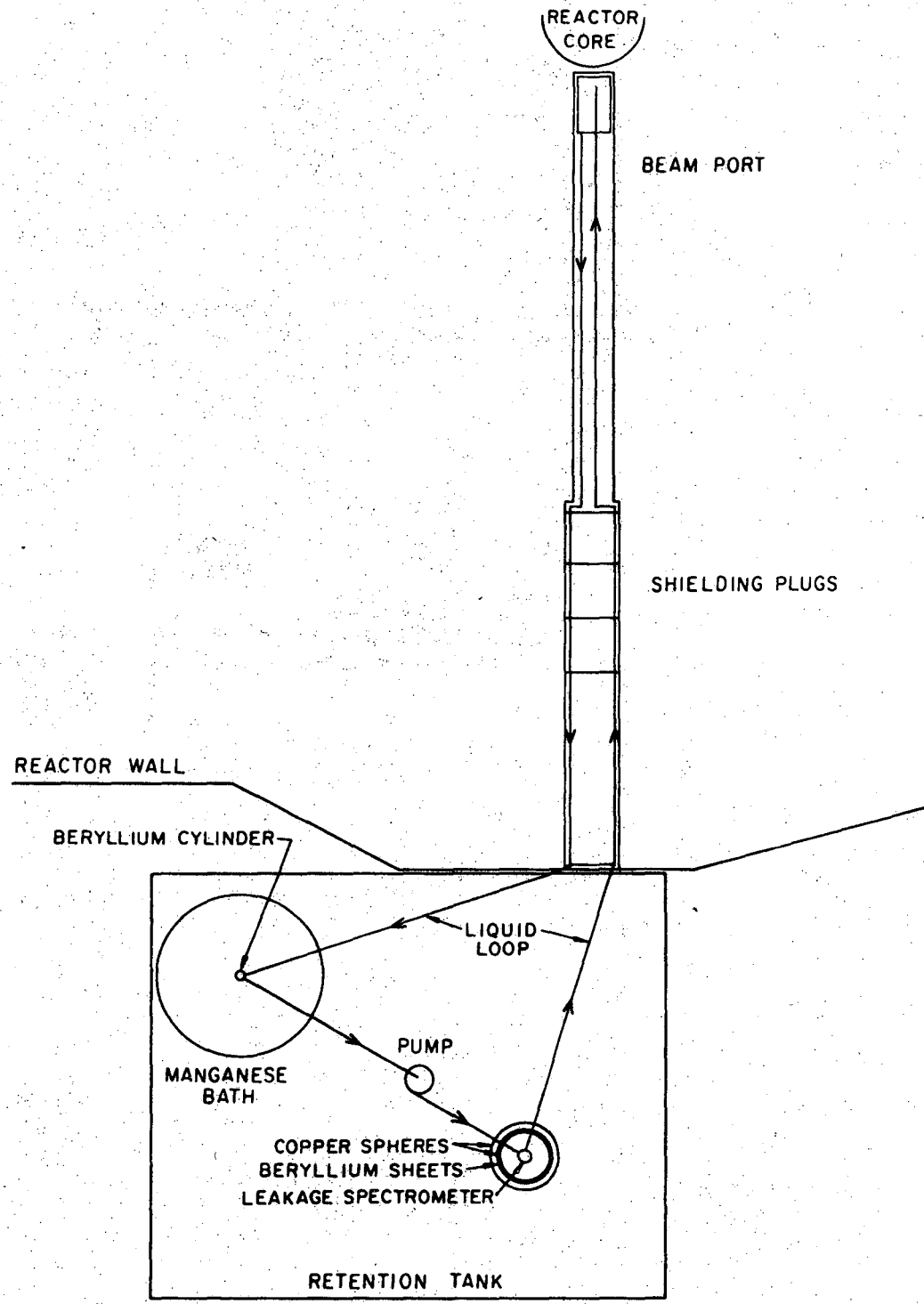


XBL 7012-7356

FIGURE 25. Spectrometer Calibration Assembly

sphere. The neutron flux near the center of the assembly, where the spectrometers were placed, was nearly isotropic and strongly peaked at the energy determined by the particular gamma ray initiating the (γ, n) reaction. The remainder of the loop consisted of a pump to keep the liquid circulating, an expansion tank to permit monitoring of the liquid and allow for any thermal expansion, and a tank to allow drainage. The relative neutron source strength for different solutions was monitored by a manganese (MnSO_4) bath through which a section of the loop consisting of a pipe surrounded by a beryllium cylinder was passed. Neutrons from the irradiated cylinder were captured by the manganese and the activity was measured. For an absolute measurement of the source strength, a 1/2 in. diameter hollow cadmium sphere packed with iodine was activated and counted. A diagram of the entire flow system showing the various components is shown in Figure 26. Surrounding the spill retention tank was concrete personnel shielding, since the activity contained in the loop approached 500 Ci at times.

In addition to the flow loop sources a solid 10 Ci Sb-Be source producing 24 keV neutrons was used. The values of the saturated activity A_{sat} of the indium cores of the four LS's and the cadmium covered iodine for the four sources are given in Table 6.



XBL 7012-7357

FIGURE 26. Flow System

TABLE 6
SATURATED ACTIVITY

Source	Detector	A_{sat} , dps	ΔA_{sat} , %
Mn	I-Cd	273	5.4
	In 4,2,0	83.2	6.9
	In 4,4,0	57.9	7.3
	In 4,2,1	31.6	7.3
	In 4,3,1	40.9	8.7
In	I-Cd	67.9	5.1
	In 4,2,0	24.2	5.1
	In 4,4,0	15.0	6.6
	In 4,2,1	10.5	5.9
	In 4,3,1	15.1	5.4
Al	I-Cd	69.9	4.6
	In 4,2,0	21.9	4.6
	In 4,4,0	12.7	4.7
	In 4,3,1	8.7	5.2
	In 4,3,1	10.1	4.9
Sb	I-Cd	11.1	5.5
	In 4,2,0	6.3	5.8
	In 4,4,0	4.7	5.9
	In 4,2,1	3.6	8.0
	In 4,3,1	4.0	6.1

B. Analysis of Experiment and Comparison of Results

The neutron source (Figure 25) was designed so that the ingoing neutron flux at the surface of the spectrometer was nearly isotropic (a smaller Be shell would still have given rotational symmetry but as mentioned in Section II.A translational invariance is required when the scalar flux is to be measured). The incident spectra for the four neutron source energies were calculated by ANISN, taking advantage of the spherical symmetry. In all cases the source was taken as isotropic within the Be shell and normalized to 1 neutron/sec spread over the group which contained the source energy E_S . The 99 group scheme in Table 2 with input data from the DLC-9 set and the "fast" library for the GGC-4 code[†] was used. The shielding was approximated by a thick concrete shell concentric to the copper sphere.

For the present geometry Eq. II.1 becomes

$$A = 4\pi R_{LS}^2 \int_{.4eV}^{E_S} dE \int_{-1}^0 d\mu \mu F^+(E, \mu) F(R_{LS}, E, \mu) .$$

In particular, since the incident flux is isotropic,

$$F(R_{LS}, E, \mu) = \phi(R_{LS}, E)/2 \quad -1 < \mu < 0$$

and

[†] See footnote on page 41.

$$A = \int_{.4\text{eV}}^{E_S} dE \phi(R_{LS}, E) 2\pi R_{LS}^2 \int_{-1}^0 d\mu \mu F^+(E, \mu)$$

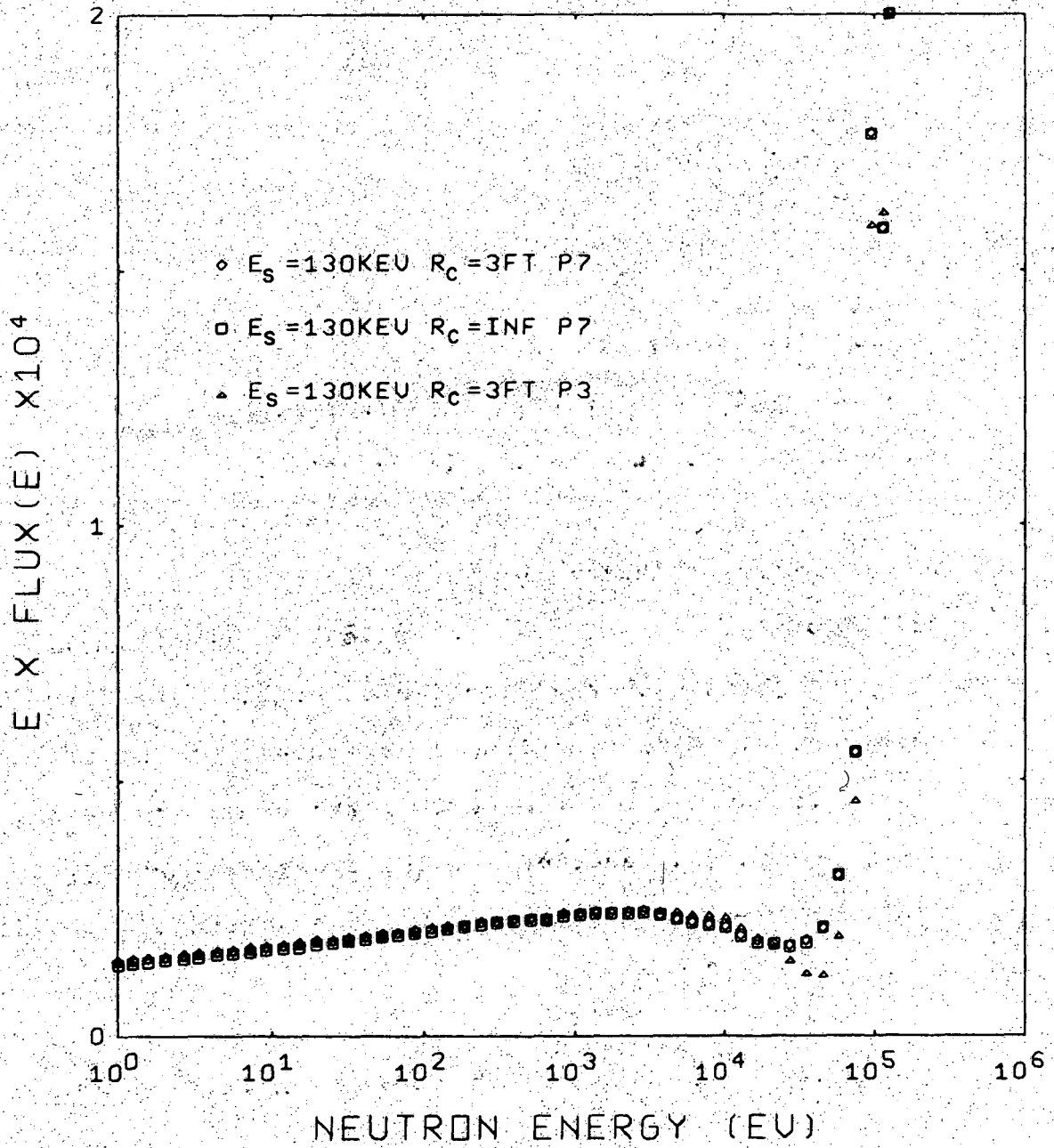
or

$$A = N_0 \int_{.4\text{eV}}^{E_S} dE \hat{\phi}(E) \sigma_{LS}(E) \quad (\text{III.1})$$

where $\hat{\phi}$ is the scalar flux due to one neutron originating in the beryllium at energy E_S , and N_0 is the total number of neutrons produced by the (γ, n) reaction. This equation is correct for the aluminum-beryllium source. The indium and manganese solutions each produce neutrons with contributions at two different energies and the integral has to be weighted with the fraction of neutrons produced at each energy. This fraction is determined by the product of the fractional occurrence f of the gamma ray causing the photoneutron reaction and the cross section $\sigma_{n\gamma}$ for the reaction (see Table 5). Thus the saturated activity

$$A = N_0 \frac{\sum_{i=1}^2 (\sigma_{\gamma n})_i f_i \int_{.4\text{eV}}^{E_{S_i}} dE \hat{\phi}_i(E) \sigma_{LS}(E)}{\sum_{i=1}^2 (\sigma_{\gamma n})_i f_i} \quad (\text{III.2})$$

Results for $\hat{\phi}_i(E)$ for $E_{S_i} = 130$ keV are given in Figure 27 for two quadrature orders and concrete radii. In this case a PN calculation denotes an N+1 order Gauss



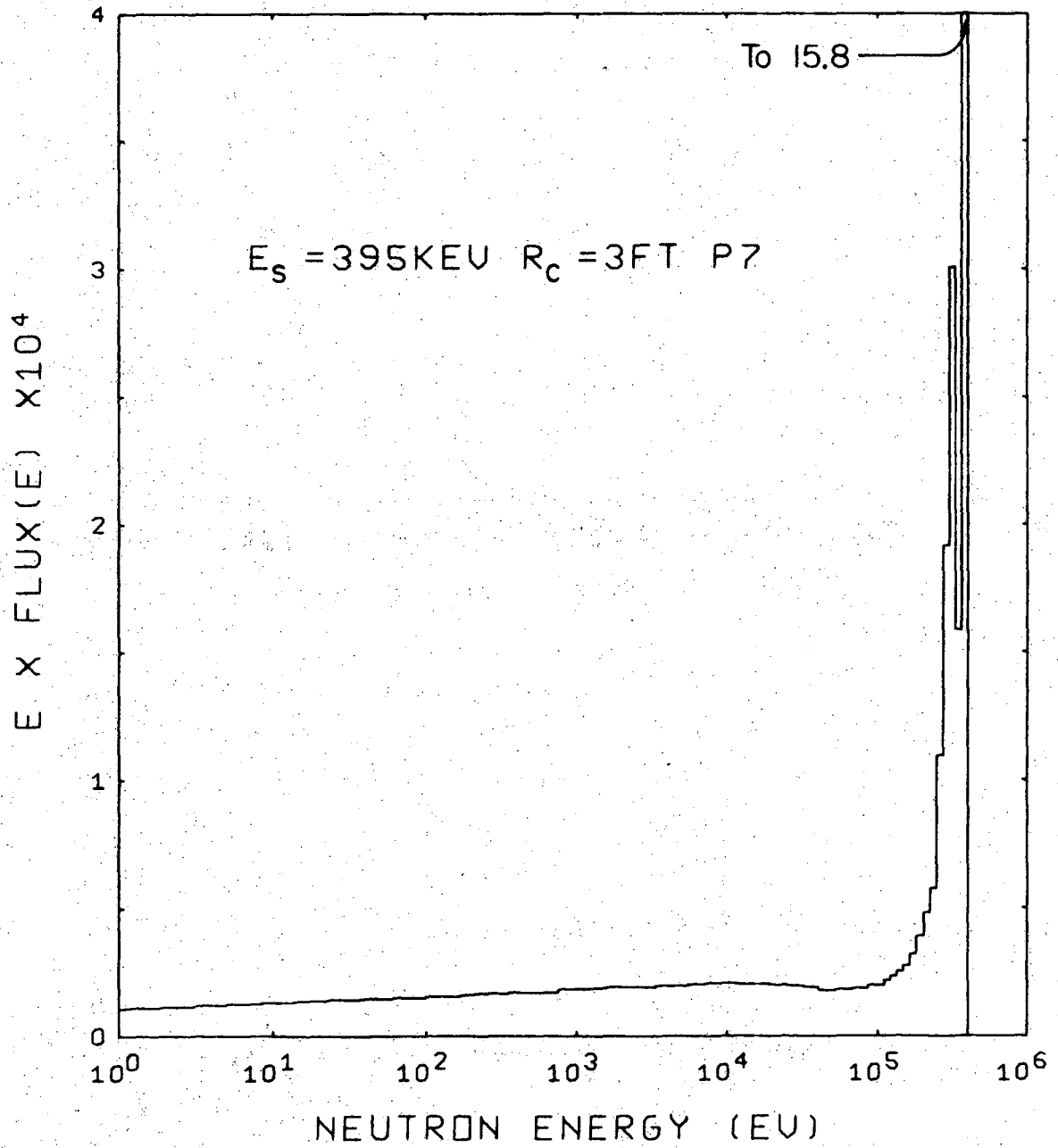
XBL 7012-4275

FIGURE 27. Incident Scalar Flux for $E_s = 130$ keV.
 Comparison of three approximations.

Legendre Quadrature with an N^{th} order expansion of the scattering kernel. The concrete shell (2 ft. thick) located at a radius R_c of 3 ft. is the lower bound on the distance between the copper shell and the concrete. Infinite R_c corresponds to no concrete being present. The variation for the two geometries is extremely small as can be seen in the figures. The peak value (15.7) is identical, and the area under the curve for the case of no concrete is only 1% lower than that for a concrete radius of 3 ft.

Using P7 calculations and $R_c=3$ ft., the flux spectra were calculated for the four different source energies (see Figures 28 to 31). For the three γ -emitting solutions, A/N_0 for each of the four spectrometers tested was determined using III.1 or III.2. Values of A/N_0 for the Sb-Be source (considered a point monoenergetic source at 9 inches) were obtained by dividing the value of σ_{LS} from the curves in Chapter II at 24 keV by $4\pi R^2$. As mentioned above, iodine was used as a flux monitor. A response $\sigma_I(E)$ was calculated in a manner similar to $\sigma_{\text{core}}(E)$. This was used together with III.1 or III.2 and the experimental values of A for iodine (Table 6) to determine N_0 for each of the four sources.

From N_0 the theoretical values of A were calculated. These are given in Table 7 along with the experimental values. On the basis of the test calculations previously mentioned, the errors in the theoretical value of A/N_0



XBL7012-4276

FIGURE 28. Incident Scalar Flux for $E_s = 395$ keV

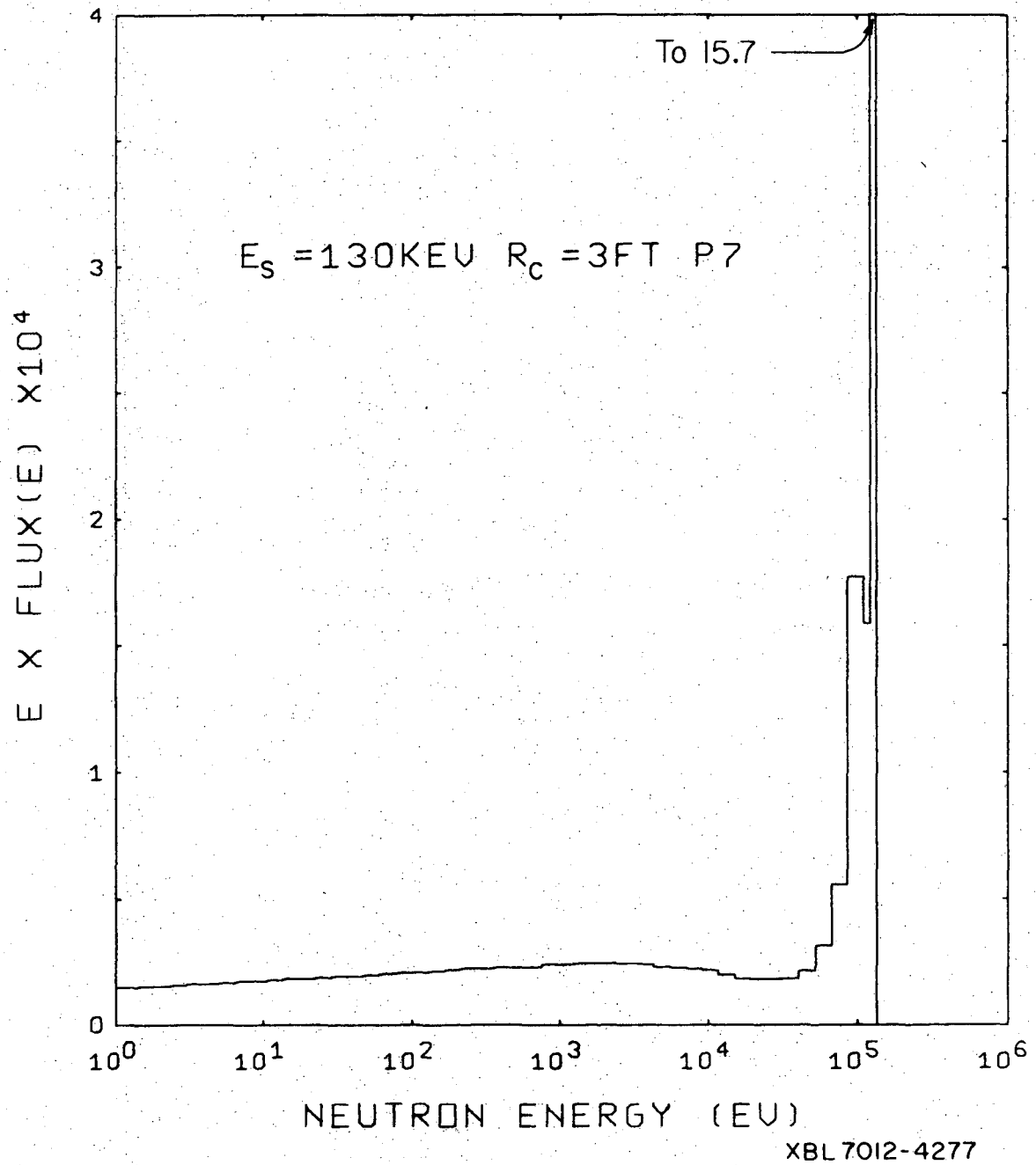


FIGURE 29. Incident Scalar Flux for $E_s = 130$ keV

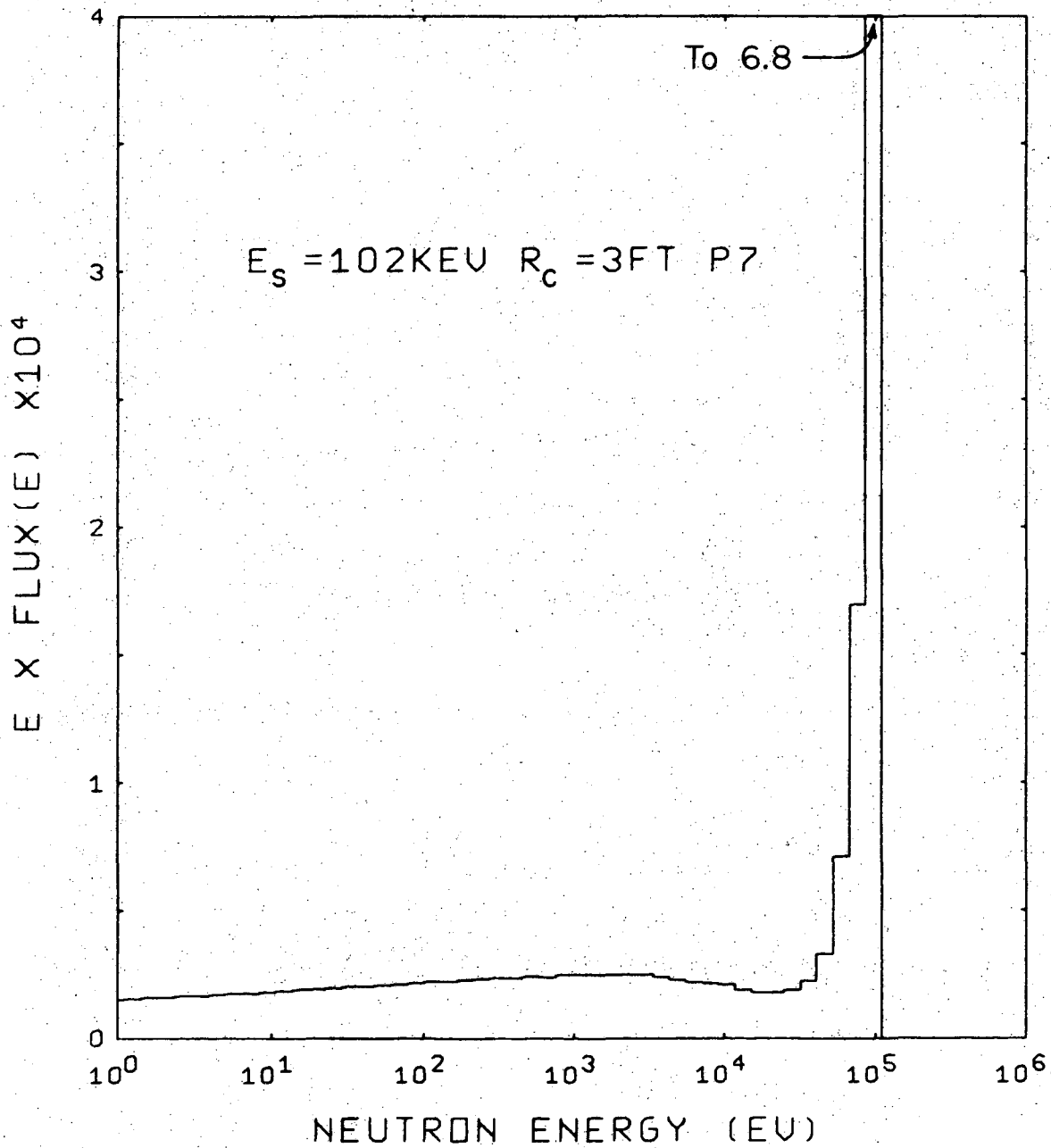


FIGURE 30. Incident Scalar Flux for $E_s = 102 \text{ keV}$

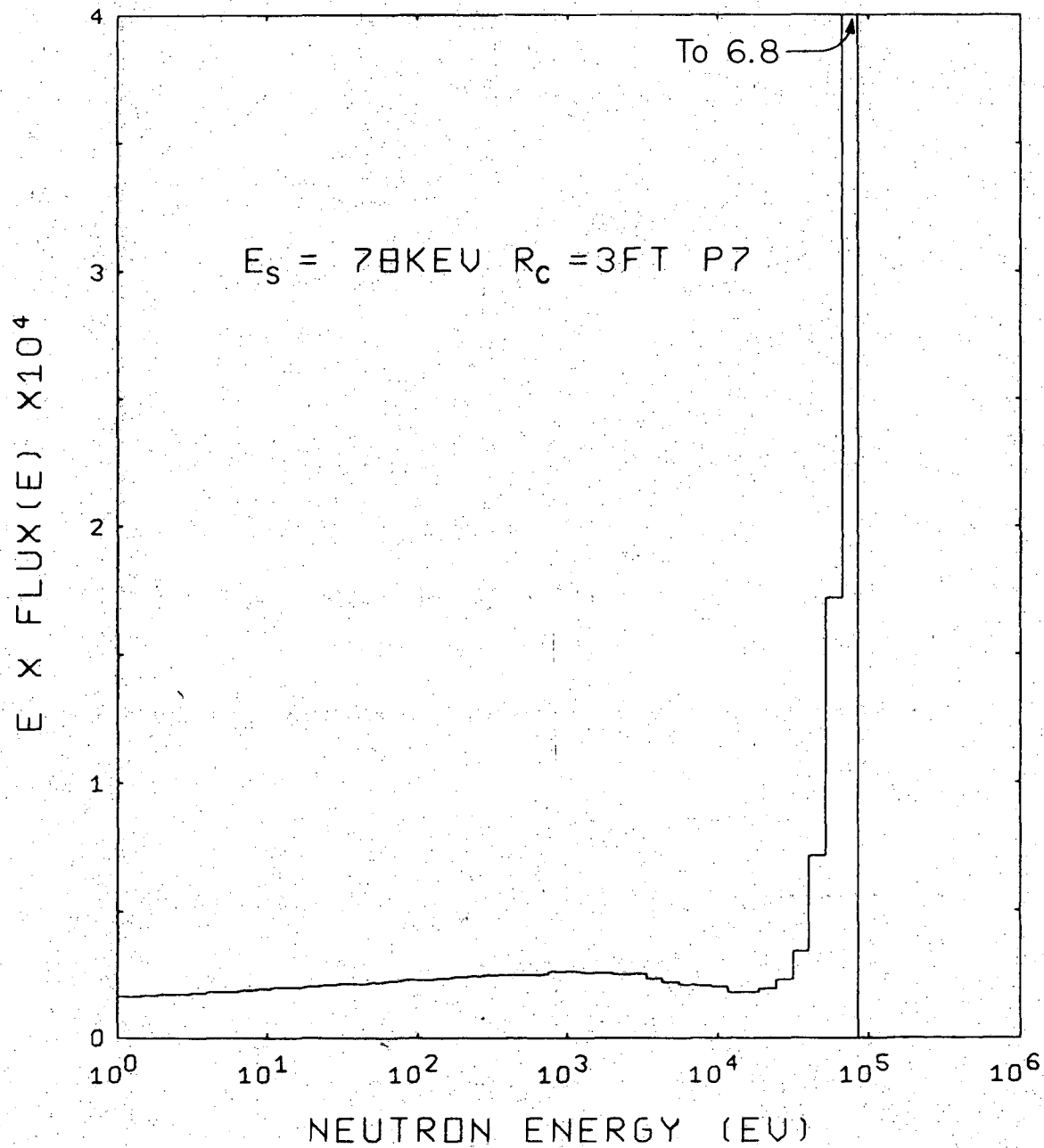


FIGURE 31. Incident Scalar Flux for $E_s = 78 \text{ keV}$

TABLE 7
COMPARISON OF EXPERIMENTAL AND THEORETICAL DATA

Spectrometer	Source	A	B	% Diff.
		A _{sat} ,dps Expt.	A _{sat} ,dps Theor. (norm to I)	$\frac{B-A}{B} \times 100$
In 4,2,0	Mn	83.2	119	30
	In	24.2	30.1	18
	Al	21.9	29.8	26
	Sb	6.3	9.6	34
In 4,4,0	Mn	57.9	62.0	6.6
	In	15.0	24.2	38
	Al	12.7	17.5	27
	Sb	4.7	6.9	32
In 4,2,1	Mn	31.6	60.2	47
	In	10.5	16.1	35
	Al	8.7	14.2	39
	Sb	3.6	6.8	47
In 4,3,1	Mn	40.9	71.0	42
	In	15.1	20.1	25
	Al	10.1	16.1	37
	Sb	4.0	6.7	40

are estimated to be 10 to 15%, at maximum. This, plus the inconsistency of certain experimental results (e.g., the failure to measure the iodine cross section correctly at the energy of the Sb-Be source whose strength was known) indicate that a more refined calibration experiment should be performed.

IV. SUMMARY OF RESULTS AND CONCLUSIONS

A set of leakage spectrometers (LS's) which make use of activation techniques has been developed. Some of these spectrometers have their peak responses in the keV range. Their resolution, however, generally seems too poor to be used for determining rapidly varying spectra. However, they could determine rough spectra or the parameters of trial functions describing spectra where there is some information about the shape.

Certain response shapes can be useful for special applications. Two examples are: (1) the nearly flat response of In 4,2.5,.625 between 10^3 and 10^5 eV (see Figure 17) will be useful for measuring the total number of neutrons in that range only; (2) determining the total dose, which can be obtained by combining LS responses to form the dose-energy relationship, which is normally smooth.

The special methods developed here for calculating $\sigma_{LS}(E)$ have proved particable and very accurate. In particular, the use of the adjoint boundary condition to account for the resonance activation of the core material is expected to be useful in other problems within nuclear technology.

Accurate calculations of the flux spectrum for the photoneutron source have been presented. These show that it was possible to produce nearly monoenergetic isotropic neutrons by the method described. It is felt that more refined experiments would agree better with results derived from the theoretical response curves.

APPENDIX A

DEVELOPMENT OF GROUP EQUATIONS USED IN ANISN

The transport equation with spherical symmetry

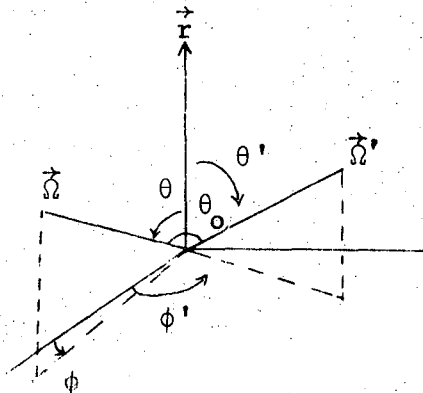
$$\begin{aligned} & \mu \frac{\partial F}{\partial r}(r, u, \mu) + \frac{(1-\mu^2)}{r} \frac{\partial F}{\partial \mu}(r, u, \mu) + \Sigma_t(u)F(r, u, \mu) \\ &= \int_0^\infty du' \int_{4\pi} d\vec{\Omega}' \Sigma_S(u' \rightarrow u; \vec{\Omega}' \cdot \vec{\Omega}) F(r, u', \mu') + S(r, u, \mu) \end{aligned} \quad (\text{A.1})$$

will be expanded into spherical harmonics and divided into lethargy groups, the form solved by ANISN.

The scattering kernel $\Sigma_S(u' \rightarrow u, \vec{\Omega}' \cdot \vec{\Omega})$, is first approximated by an L^{th} order Legendre expansion in the cosine of the scattering angle $(\vec{\Omega}' \cdot \vec{\Omega})$

$$\Sigma(u' \rightarrow u; \vec{\Omega}' \cdot \vec{\Omega}) = \frac{2\ell+1}{4\pi} B_\ell(u' \rightarrow u) P_\ell(\vec{\Omega}' \cdot \vec{\Omega}), \quad (\text{A.2})$$

where $\vec{\Omega}'$ and $\vec{\Omega}$ are the initial and final neutron directions respectively.



$$\theta = \cos^{-1} \mu$$

$$\theta' = \cos^{-1} \mu'$$

$$\theta_0 = \cos^{-1} \mu_0$$

\vec{r} points radially outward

$\vec{\Omega}' \cdot \vec{\Omega}$ depends only on μ, μ' and $\phi' - \phi$. The spherical harmonics addition theorem is

$$\begin{aligned}
 P_\ell(\vec{\Omega}' \cdot \vec{\Omega}) &= \frac{4\pi}{2\ell+1} \sum_{m=-\ell}^{\ell} Y_\ell^{m*}(\vec{\Omega}) Y_\ell^m(\vec{\Omega}') \\
 &= \sum_{m=-\ell}^{\ell} \frac{(\ell-m)!}{(\ell+m)!} P_\ell^m(\mu) P_\ell^m(\mu') e^{im(\phi' - \phi)} \quad (A.3)
 \end{aligned}$$

where Y_ℓ^m are spherical harmonics (* indicating complex conjugation) and P_ℓ^m are the associated Legendre functions. Substituting A.3 into A.2 and performing the integration over ϕ' in A.1

$$\begin{aligned}
 &\int_0^\infty du' \int_{4\pi} d\vec{\Omega}' \Sigma_S(u' \rightarrow u; \vec{\Omega}' \cdot \vec{\Omega}) F(r, u', \mu') \\
 &= \int_0^\infty du' \int_{-1}^1 d\mu' \sum_{\ell=0}^L \frac{2\ell+1}{4\pi} B_\ell(u' \rightarrow u) F(r, u, \mu') P_\ell^m(\mu) P_\ell^m(\mu') \times \\
 &\times \int_0^{2\pi} d\phi' \sum_{m=-\ell}^{\ell} \frac{(\ell-m)!}{(\ell+m)!} e^{im(\phi' - \phi)},
 \end{aligned}$$

but

$$\int_0^{2\pi} d\phi' \sum_{m=-\ell}^{\ell} \frac{(\ell-m)!}{(\ell+m)!} e^{im(\phi' - \phi)} = \begin{cases} 2\pi & m=0 \\ 0 & m \neq 0 \end{cases}$$

so A.1 becomes

$$\begin{aligned}
 & \mu \frac{\partial F}{\partial \mu} (r, u, \mu) + \frac{(1-\mu^2)}{r} \frac{\partial F}{\partial \mu} (r, u, \mu) + \Sigma_t(u) F(r, u, \mu) \\
 &= \sum_{\ell=0}^L \frac{2\ell+1}{2} P_\ell(\mu) \int_0^\infty du' B_\ell(u' \rightarrow u) \int_{-1}^1 d\mu' P_\ell(\mu') F(r, u', \mu') \\
 &+ S(r, u, \mu) \tag{A.4}
 \end{aligned}$$

We assume that the flux is constant within the g^{th} lethargy group

$$F(r, u, \mu) = F_g(r, \mu) \quad u_g < u < u_{g+1} \quad g=1, \dots, G.$$

The flux per solid angle within the g^{th} group N_g is then

$$N_g(r, \mu) = F_g(r, \mu) \Delta u_g$$

where

$$\Delta u_g \equiv u_{g+1} - u_g$$

Integrating A.4 over the g^{th} group, we obtain

$$\begin{aligned}
 & \mu \frac{\partial}{\partial r} N_g(r, \mu) + \frac{1-\mu^2}{r} \frac{\partial}{\partial \mu} N_g(r, \mu) + \Sigma_{tg} N_g(r, \mu) \\
 &= \sum_{\ell=0}^L \frac{2\ell+1}{2} P_\ell(\mu) \int_{u_g}^{u_{g+1}} du \sum_{g'=1}^G \int_{u_{g'}}^{u_{g'+1}} du' B_\ell(u' \rightarrow u) \int_{-1}^1 d\mu' P_\ell(\mu') F_{g'}(r, \mu') \\
 &+ S_g(r, \mu), \tag{A.5}
 \end{aligned}$$

where

$$\Sigma_{tg} \equiv \int_{u_g}^{u_{g+1}} \Sigma_t(u) \frac{du}{\Delta u_g}$$

and

$$S_g(r, \mu) \equiv \int_{u_g}^{u_{g+1}} S(r, u, \mu) du$$

Defining

$$B_{\ell}^{g+g'} \equiv \frac{\int_{u_g}^{u_{g+1}} du \int_{u_{g'}}^{u_{g'+1}} du' B_{\ell}(u'+u)}{\Delta u_{g'}} \quad \ell=1, \dots, L \quad (\text{A.6})$$

yields for A.5

$$\begin{aligned} & \mu \frac{\partial}{\partial r} N_g(r, \mu) + \frac{1-\mu^2}{r} \frac{\partial N_g}{\partial \mu}(r, \mu) + \Sigma_{tg} N_g(r, \mu) \\ &= \sum_{\ell=0}^L \frac{2\ell+1}{2} P_{\ell}(\mu) B_{\ell}^{g+g'} \int_{-1}^1 N_g(r, \mu') P_{\ell}(\mu') d\mu' \end{aligned} \quad (\text{A.7})$$

APPENDIX B
TESTS OF ANISN

A. Plane Isotropic Source in an Infinite Medium of Hydrogen
with Unit Cross Section

(1) P-1 Approximation

With an energy structure of one group of width 10^{-6} lethargy units (l.u.) followed by 10 groups of width .01 l.u., an S2-P1 ANISN calculation was performed for the above problem. According to the P-1 approximation, the flux at the source lethargy is

$$\phi(x,0) = \sqrt{3} e^{-\sqrt{3} \Sigma_t x} \text{ Me}^{60a} \quad (\text{B.1})$$

The P-1 flux for neutrons with lethargy slightly greater than the source lethargy was given by Amster^{Am68} as

$$\phi(x,0^+) = 3xe^{-\sqrt{3} \Sigma_t x} \quad (\text{B.2})$$

B.1 and B.2 are plotted in Figure 32 along with results from the ANISN calculation for the first two groups. It can be seen that except for the large mesh spacing (~ 1 mean free path), ANISN gives excellent results. The deviations near $x=0$ are caused by the fact that the plane source had to be given finite thickness in ANISN.

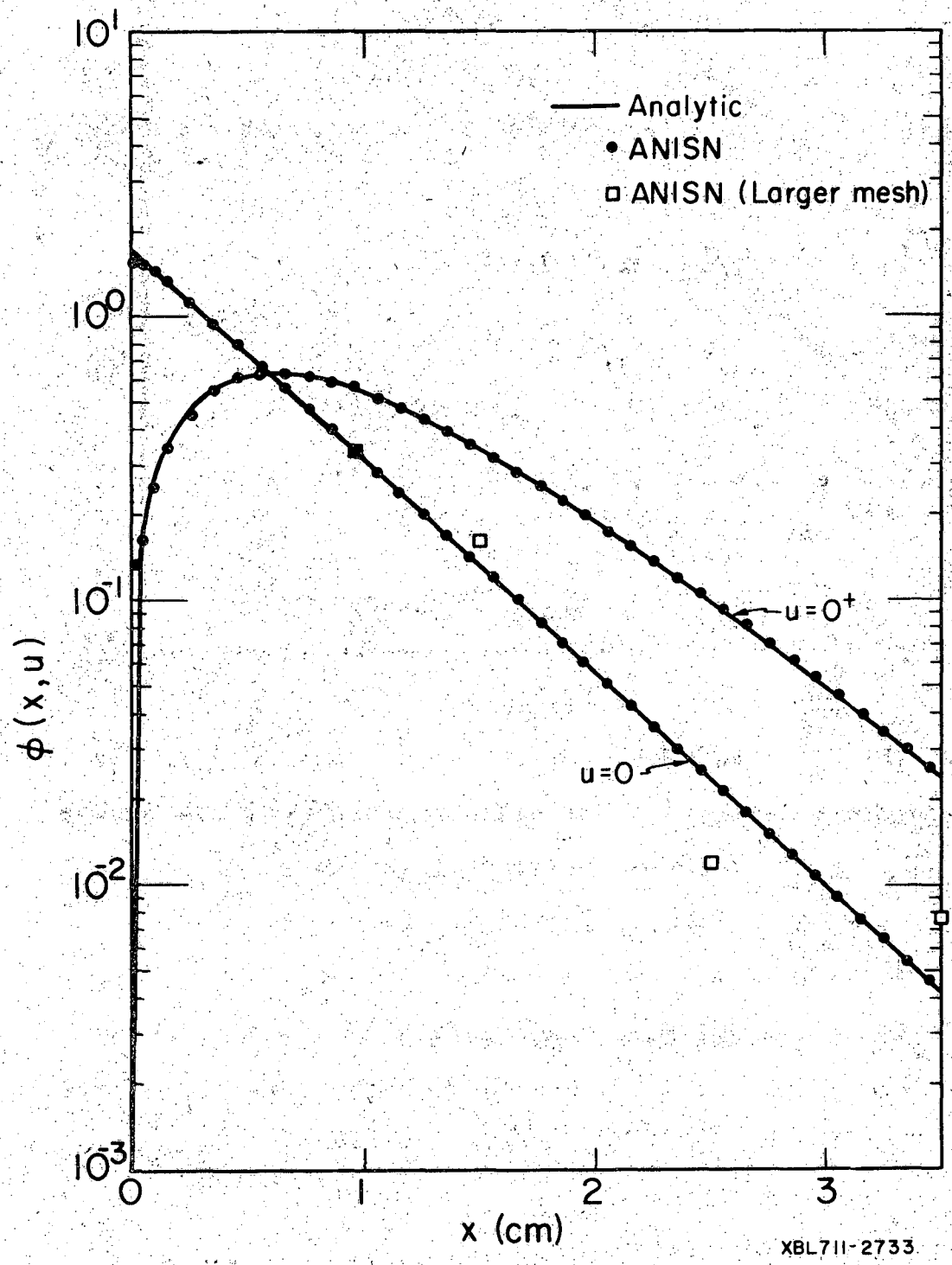


FIGURE 32. P-1 Approximation for a Plane Source at $x=0$ in an Infinite Medium. Comparison of analytic solution and ANISN for two lethargies. The squares indicate ANISN results for a larger mesh spacing at $u=0$.

(2) Spatial Moments

The spatial moments for the above problem

$$M_o^n(u) = \int_{-\infty}^{\infty} x^n \phi(x,u) dx$$

are rigorously given by

$$M_o^0 = \frac{1}{\Sigma_S} [\delta(u) + 1]$$

$$M_o^2 = \frac{1}{\Sigma_S} \left[\frac{\delta(u)}{3} + \frac{1}{3} e^{-u/2} + u + \frac{2}{3} \right] \quad (\text{B.3})$$

A P-1 solution for the above problem gives the exact second moment. ^{Ma47} As a check on the correctness of the ANISN method, the second moment for the last (11th) group (.09-.1 l.u.) was calculated using Simpson's rule. The moment determined in this manner was only .5% different from the rigorous value determined by B.3, indicating that for this problem, the ANISN lethargy dependence is accurate.

B. Pure Absorber Spherical Geometry

The flux due to an isotropic spherical shell source emitting 1 neutron/sec in a purely absorbing medium is given ^{Ca53} by

$$\phi(r) = \frac{1}{8\pi r a} \left\{ \frac{E_1[\Sigma_a(a-r)] - E_1[\Sigma_a(a+r)]}{2} \right\} \quad (\text{B.4})$$

where a is the radius of the source and E_n is the n^{th} order exponential integral function. Figure 33 shows B.4 and the results of a S8 ANISN calculation plotted for $a=2.4$ and $\Sigma_a=1$.

C. Energy Dependent, Heavy Scatterer

The spatially independent collision density $F(u) = \Sigma_S(u)\phi(u)$ due to a delta-function source $\delta(u)$, is given Me60b by

$$F(u) = \frac{e^{\alpha u/1-\alpha}}{1-\alpha} ; \quad 0 < u < \ln(1/\alpha)$$

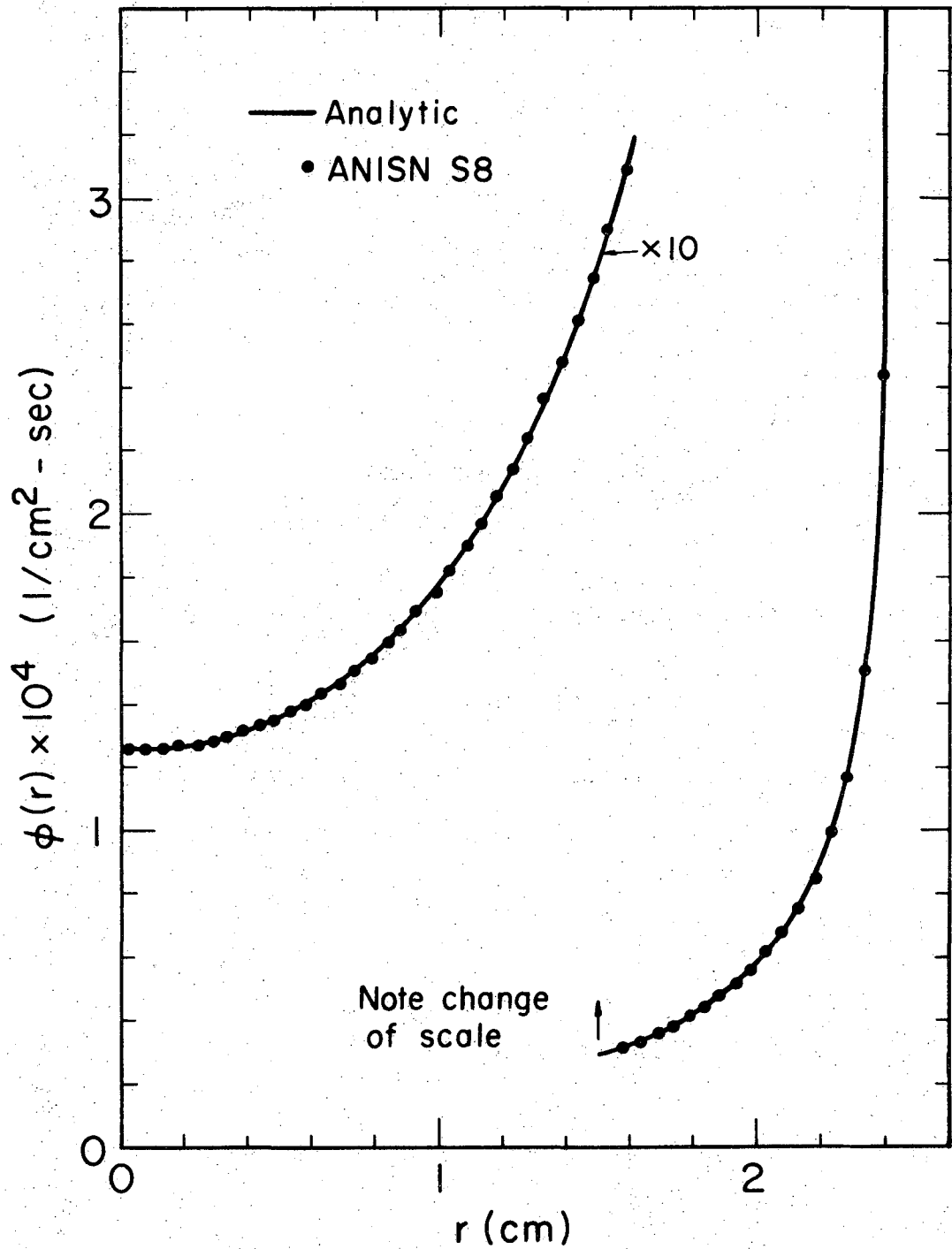
$$F(u) = \frac{1-\alpha^{1/1-\alpha}}{1-\alpha} e^{\alpha u/1-\alpha} - \frac{\alpha}{(1-\alpha)^2} \left(u - \ln \frac{1}{\alpha}\right) e^{\alpha u/1-\alpha} ;$$

$$\ln \frac{1}{\alpha} < u < 2 \ln \frac{1}{\alpha} \quad (\text{B.5})$$

for the first two collision intervals, where

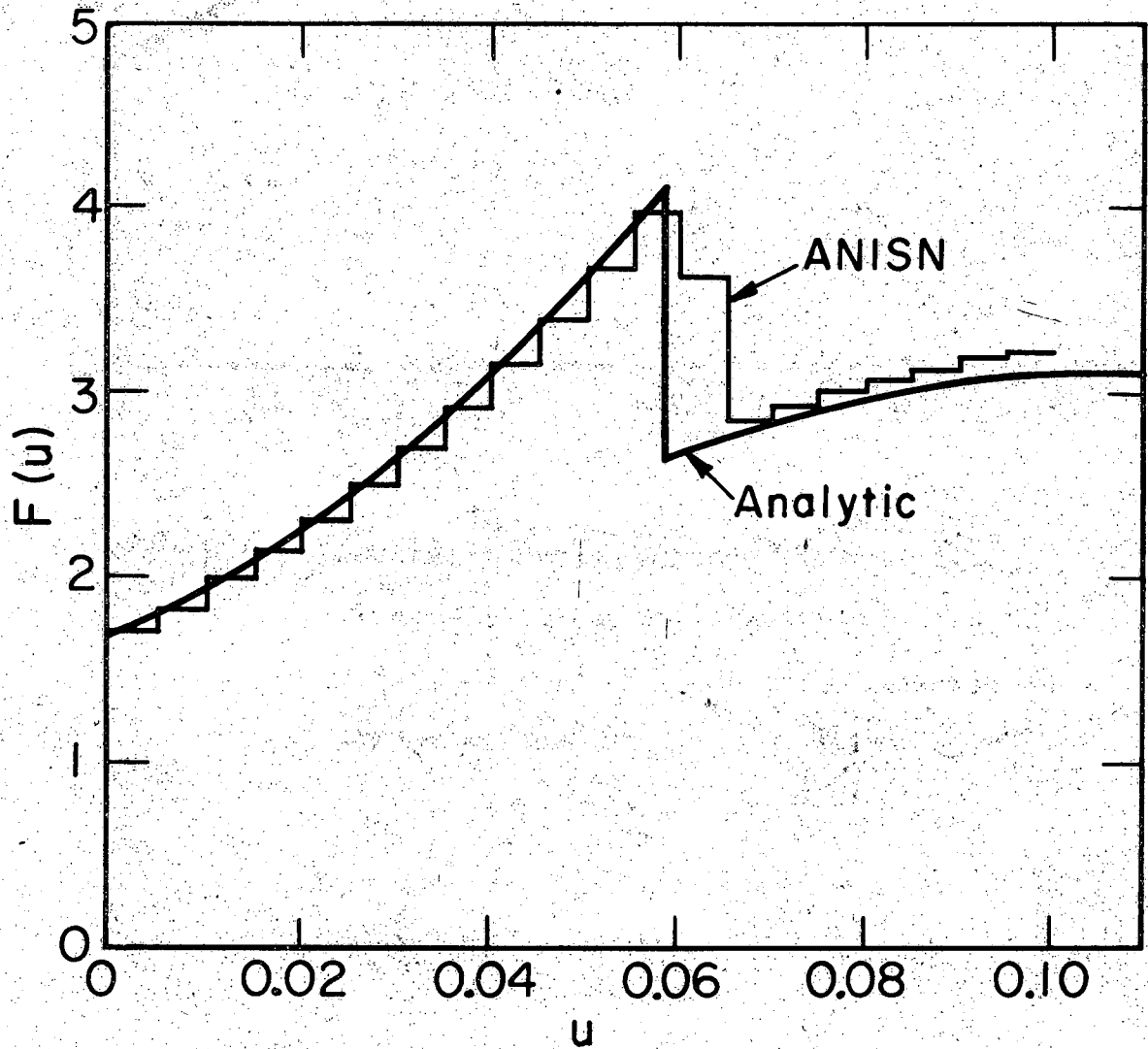
$$\alpha = \left(\frac{A-1}{A+1} \right)^2 .$$

A 20 group ANISN solution and B.5 are plotted in Figure 34 for $A=63.5$.



XBL711-2736

FIGURE 33. Flux in a Purely Absorbing Medium Due to an Isotropic Shell Source at $r=2.4$ cm.



XBL711-2737

FIGURE 34. Collision Density Over Two Scattering Intervals for a Non-Absorbing Infinite Medium with $A=63.5$ and a Delta-Function Source at $u=0$

APPENDIX C

CROSS SECTIONS AND ENERGY TRANSFER ARRAY

A. Resonance Cross Sections

The resonance cross sections required for the adjoint boundary condition are generated using a single-level Breit-Wigner formula.

The radiative capture cross section is

$$\sigma_a(E) = 2.60 \times 10^6 \sum_i g_i \frac{\Gamma_{ni}^0 \Gamma_{\gamma i}}{\Gamma_i^2 \sqrt{E}} \frac{(1 + 1/A)^2}{\left(\frac{E - E_i}{\Gamma_i/2}\right)^2 + 1} \quad (C.1)$$

where the total width has been taken to be

$$\Gamma_i = \Gamma_{ni}^0 \sqrt{E_i} + \Gamma_{\gamma i}$$

Γ_n^0 is the reduced neutron width ($\Gamma_n / \sqrt{E_0}$) and Γ_γ is the gamma ray width. E is the neutron energy, E_i is the energy of the i^{th} resonance, and A is the mass of the target nucleus. The statistical spin factor is

$$g = \frac{1}{2} \frac{2J+1}{2I+1},$$

where I is the target spin and J is the spin of the compound nucleus.

In a similar manner, the resonance scattering cross section is given by

$$\sigma_S(E) = \sigma_P + \sum_i \left[2.6 \times 10^6 g_i \frac{(\Gamma_{ni}^o)^2}{\Gamma^2} \frac{(1 + 1/A)^2}{\left(\frac{E-E_i}{\Gamma/2}\right)^2 + 1} + 1.61 \times 10^3 g_i \frac{\Gamma_{ni}^o \sqrt{\sigma_P}}{\Gamma_i} \frac{\frac{E-E_i}{\Gamma/2} (1 + 1/A)^2}{\left(\frac{E-E_i}{\Gamma/2}\right)^2 + 1} \right] \quad (C.2)$$

where σ_P is the spin independent potential scattering cross section. The second term in the summation accounts for the interference between resonance and potential scattering. Me60c, Ho66

The total cross section is

$$\sigma_t(E) = \sigma_a(E) + \sigma_S(E) \quad (C.3)$$

B. Average Unresolved Resonance Cross Section

The average capture cross section in the unresolved resonance region for neutrons of orbital angular momentum, ℓ , assuming a Porter-Thomas probability distribution of reduced neutron widths

$$P(x) = \frac{1}{\sqrt{2\pi} x} e^{-x/2}$$

with

$$x = \Gamma_{n\ell}^o / \bar{\Gamma}_{n\ell}^o$$

is given by Garrison and Roos^{Ga61} as

$$\bar{\sigma}_a^\ell(E) = \frac{4.09 \times 10^9}{\sqrt{E}} \frac{V_\ell(E) \bar{\Gamma}_{n\ell}^0}{D} \phi(\theta_\ell) (2\ell+1) (1 + 1/A)^2$$

where $\bar{\Gamma}_{no}^\ell$ is the average reduced width obtained from resolved resonance data. The neutron penetrability functions, $V_\ell(E)$ are given by

$$V_0 = 1$$

$$V_1 = Y^2 / (1+Y^2)$$

$$V_2 = Y^4 / (9+3Y^2+Y^4)$$

$$V_3 = Y^6 / (225+45Y^2+6Y^4+Y^6)$$

and

$$V_4 = Y^8 / (1025+1575Y^2+135Y^4+10Y^6+Y^8)$$

where

$$Y = \frac{A^{1/3} E^{1/2}}{3250}$$

$\bar{\Gamma}_{n\ell}^0/D$ is the neutron strength function and

$$\theta_\ell = \frac{\Gamma_\ell / D_\ell}{\left(\frac{\bar{\Gamma}_{n\ell}^\ell}{D} \right) V_\ell} \times 10^{-3}$$

The level spacing per spin state D_ℓ is obtained from observed level spacing, D_0 , by

$$D_\ell = D_0 \frac{2\ell+1}{\sum_J g_J^2}$$

The sum $\sum_J g_J^2$ extends over the statistical spin factors for all allowable combinations of the spin J of the compound nucleus for a target spin I and an orbital angular momentum ℓ of the neutron. The function $\phi(\theta_\ell)$ is given by

$$\phi(\theta_\ell) = \int_0^\infty \frac{xP(x)}{1 + x/\theta_\ell} dx .$$

$\sigma_\ell^\ell(E)$ is a smooth function of energy, so the average capture cross section for group g is given by

$$(\bar{\sigma}_a)^g = \sum_{\ell=0}^{\ell} \frac{\max_{\ell} \sigma_\ell^\ell(E_g) + \sigma_\ell^\ell(E_{g+1})}{2} . \quad (C.4)$$

Unresolved resonance scattering is usually either neglected ($(\bar{\sigma}_s)^g = \sigma_p$, (potential scattering) or determined in a manner similar to $(\bar{\sigma}_a)^g$, neglecting interference effects.

C. Transfer Array

The energy transfer array or scattering kernel expansion coefficients $B_\ell^{g \rightarrow g'}$ (see Eq. A.6) written in terms of an integral over energy are given by

$$B_{\ell}^{g \leftarrow g'} = \frac{1}{\Delta u_g} \int_{E_g}^{E_{g+1}} dE \int_{E_{g'}}^{E_{g'+1}} \frac{dE'}{E'} B_{\ell}(E' \rightarrow E)$$

The factor $1/E'$ corresponds with the change of variables to a weighting flux that is constant in lethargy. $B_{\ell}^{g \leftarrow g'}$ is composed of three terms

$$(B_{\ell}^{g \leftarrow g'})_n + (B_{\ell}^{g \leftarrow g'})_{n'} + (B_{\ell}^{g \leftarrow g'})_{2n}$$

denoting elastic scattering, inelastic scattering and an $(n,2n)$ reaction respectively. In each case the transfer coefficient $B_{\ell}(E' \rightarrow E)$ is obtained from a differential cross section

$$B_{\ell}(E' \rightarrow E) = \int_{-1}^1 d\mu_0 \sigma(E' \rightarrow E, \mu_0) \quad (C.5)$$

where μ_0 is the cosine of the scattering angle in the lab system.

For elastic scattering

$$\begin{aligned} \sigma_n(E' \rightarrow E, \mu_0) &= \sigma_n(E') \sum_m \frac{2m+1}{2} f_m(E) P_m(\mu_c) \frac{\partial \mu_c}{\partial \mu_0} \times \\ &\times \delta[E - E' + \frac{1-\alpha}{2} E'(1-\mu_c)] \end{aligned} \quad (C.6)$$

where $\sigma_n(E')$ is the elastic scattering cross section, μ_c is the cosine of the scattering angle in the center-

of-mass (CM) system, $f_m(E')$ are determined from the CM differential cross section $\sigma_n(E', \mu_c)$ and

$$\alpha = \left(\frac{A-1}{A+1} \right)^2$$

The delta-function arises because the final energy E is determined by kinematics for a given initial energy E' and μ_c . Changing the integration variable in C.5 to energy and noting that

$$\frac{d\mu_c}{d\mu_o} d\mu_o = d\mu_c = \frac{2}{(1-\alpha)E'} dE,$$

and using C.6 yields

$$(B_\ell(E' \rightarrow E))_n = \frac{\sigma_n(E')}{(1-\alpha)E'} P_\ell(\mu_o) \sum_m (2m+1) f_m(E') P_m(\mu_c)$$

for $\alpha E' \leq E \leq E'$ (C.7)

Otherwise

$$(B_\ell(E' \rightarrow E))_n = 0.$$

For inelastic scattering for which the discrete level excitation cross sections $\sigma_{n,k}(E')$ and Q-value are known

$$\sigma_{n',k}(E' \rightarrow E, \mu_0) = \sigma_{n',k}(E, \mu_0) \delta \left[E - E' + \frac{AW_k}{A+1} + \frac{2AE'}{(A+1)^2} (1-\mu_c) \sqrt{1 - \frac{(A-1)}{AE'} W_k} \right]$$

where $W_k = -Q$. Following the same steps as for elastic scattering above

$$(B_{\ell k}(E' \rightarrow E))_{n'} = \frac{\sigma_{n',k}(E') P_{\ell}(\mu_0)}{(1-\alpha) E' \sqrt{1 - \frac{(A+1)}{AE'} W_k}} \times \sum_m (2m+1) f_{m,k}(E') P_{\ell}(\mu_c) \quad (C.8)$$

for

$$\left(\frac{1 + A \sqrt{1 - \frac{(A+1)}{AE'} W_k}}{1+A} \right)^2 \geq \frac{E}{E'} \geq \left(\frac{1 - A \sqrt{1 - \frac{(A+1)}{AE'} W_k}}{1+A} \right)^2$$

otherwise

$$(B_{\ell k}(E' \rightarrow E))_{n'} = 0$$

For $(n, 2n)$ reactions and that portion of the inelastic cross section that cannot be treated as individual levels a statistical model is used. An evaporation type spectrum is assumed

$$N(E', E) = C(E') E e^{-E/\theta(E')}$$

where $C(E')$ is the normalization factor and $\theta(E')$ is the nuclear temperature

$$\theta(E') = kT \approx 3226 \sqrt{E'/A}$$

The differential inelastic scattering kernel in the laboratory system is

$$\sigma_{in}(E' \rightarrow E, \mu_o) = \frac{\sigma_{in}(E')}{2} \frac{d\mu_c}{d\mu_o} N(E', E)$$

where it is assumed that the angular distribution of secondary neutrons is isotropic. The subscript in stands either for n' or $2n$. Thus

$$(B_o(E', E))_{in} = \sigma_{in}(E') N(E', E) \quad E < E' \quad (C.9)$$

Of these three contributions, the elastic transfer is the most important, the other two being non-zero only above 100 keV, for the isotopes of interest here.

REFERENCES

- Ad67 J. Adir and K.D. Lathrop, "Theory of Methods Used in the GGC-3 Multigroup Cross Section Code", USAEC Report GA-7156 (1967).
- Al65 E. Albold and P. von Blankenhagen, "Eine Messung des isomeren Aufspaltverhältnisse bei Aktivierung in den ersten 3 Indium-Resonanzen", Nukleonik, 7(7), 406 (1965).
- Am68 H.J. Amster, "An Analysis of Methods for Calculating Spatially Dependent Neutron Slowing Down Distributions", Nuc. Sci. Eng., 34, 313 (1968).
- Be63 K.H. Beckurts, M. Brose, M. Kroche, G. Krüger, W. Pönitz and H. Schmidt, "Thermal Activation Cross Sections and Resonance Integrals of Indium", Nuc. Sci. Eng., 17, 329 (1963).
- Bi70 S.E. Binney, "Calibration of Boron-Covered Multi-sphere Detectors Using Resonance Activation for Neutron Spectrometry in the keV Region", Ph.D. Thesis, U. of California, Berkeley (1970).
- Bo60 T.W. Bonner, "Measurements of Neutron Spectra from Fission", Nuc. Phys., 23, 116 (1961).
- Br60 R.L. Bramblett, R.I. Ewing and T.W. Bonner, "A New Type of Neutron Spectrometer", Nuc. Inst. Meth., 9, 1 (1960).
- Ca53 K.M. Case, F. de Hoffman and G. Placzek, Introduction to the Theory of Neutron Diffusion, Vol. 1 (Los Alamos Scientific Laboratory, 1953), p. 16.
- Di65 G. DiCola and A. Rota, "Calculation of Differential Fast Neutron Spectra from Threshold-foil Activation Data by Least-Squares Series Expansion Methods", Nuc. Sci. Eng., 23, 344 (1965).
- Do60 F. Domonic and V.L. Sailor, "Dependence of the In^{116} Activation Ratio on Neutron Energy", Phys. Rev., 119(1), 208 (1960).
- Dr58 J.E. Draper, C.A. Fenstermacher and H.L. Schulz, "Variations in Spectra of Resonance Neutron Capture Gamma Rays in Indium," Phys. Rev., 111(3), 906 (1958).
- En67 W. Engle, "A Users Manual for ANISN, A One Dimensional Discrete Ordinates Transport Code with Anisotropic Scattering," USAEC Report K-1693 (1967).

- Ga61 J.D. Garrison and B.W. Roos, "Fission Product Capture Cross Sections", USAEC Report GA-2112 (1961).
- Go64 R. Gold, "An Iterative Unfolding Method for Response Matrices", USAEC Report ANL-6984 (1964).
- Go66 M.D. Goldberg, S.F. Mughabghab, S.N. Burohit, B.A. Magurno, and V.M. May, "Neutron Cross Sections", USAEC Report BNL-325 Second Edition Supplement No. 2 (1966).
- Ho66 H.C. Honeck, "ENDF/B Specifications for an Evaluated Nuclear Data File for Reactor Applications", USAEC Report BNL-50066 (T-467) ENDF 102 (1966).
- Ki60 C.M. Kim, "A Theoretical Comparison of 4π Fast-Neutron Spectrometers", (M.S. Thesis) USAEC Report UCRL-9504 (1960).
- La65 K.D. Lathrop, "DTF-IV, a Fortran IV Program for Solving the Multigroup Transport Equation with Anisotropic Scattering", USAEC Report LA-3373 (1965).
- Ma47 R.E. Marshak, "Theory of the Slowing Down of Neutrons by Elastic Collisions with Atomic Nuclei", Rev. Mod. Phys., 19, 185 (1947).
- Mc67 W.N. McElroy, S. Berg, and G. Gigus, "Neutron Spectral Determination by Foil Activation", Nuc. Sci. Eng., 27, 533 (1967).
- Mc69 W.N. McElroy, S. Berg, J.B. Crockett and R.J. Tuttle, "Measurement of Neutron Flux Spectra by a Multiple Foil with Reactor Physics Calculations and Spectrometer Measurements", Nuc. Sci. Eng., 36, 15 (1969).
- Me60 R.V. Meghreblian and D.K. Holmes, Reactor Analysis, McGraw-Hill, New York (1960). (a, p.182; b, p.94; c, p.673)
- Me64 S.K. Metha, "Modification of Bonner Sphere Spectrometer to Measure Spectra of Low-Energy Neutrons from (α ,n) Sources", USAEC Report ORNL-3714, p. 80 (1964).
- Me65 S.K. Metha, "A New Method for the Evaluation of Neutron Emission, Kerma, Kerma Equivalent, Dose Equivalent of the Spectrum Below 1 MeV for (α ,n) Sources, Using Bonner Spheres", USAEC Report ORNL-TM-1171 (1965).

- Po65 W. Pönitz, "The Spin of the 2-sec Isomeric State of In¹¹⁶", Nuc. Phys., 66, 297 (1965).
- Ro69 Y.T. Routti, "High Energy Neutron Spectroscopy with Activation Detectors, Incorporating New Methods for the Analysis of Ge(Li) Gamma Ray Spectra and the Solution of Fredholm Integral Equations", Ph.D. Thesis, USAEC Report UCRL-18514 (1969).
- Se59 D.S. Selengut, "Variational Analysis of Multi-Dimensional Systems", USAEC Report HW-59126, p. 89 (1959).
- St68 A. Staub, D. Harris and M. Goldsmith, "Analysis of a Set of Critical Homogeneous U-H₂O Spheres", Nuc. Sci. Eng., 34, 263 (1968).
- Th53 B.W. Thompson, "Fast-Neutron Scintillation Survey Meter", USAEC Report UCRL-2357 (1953).
- Tr68 D.K. Trubey and B.F. Maskewitz, Ed., "A Review of the Discrete Ordinates S_n Method for Radiation Transport Calculations", USAEC Report ORNL-RSIC-19 (1968).

ACKNOWLEDGMENTS

I would like to express my gratitude to the three men with whom I worked on this project. Dr. Hans Mark and Dr. Stephen Binney, who formulated the project, helped me in innumerable ways to understand the experimental work and guided my analysis of that work. Special thanks go to Dr. Harvey Amster, my thesis advisor, who helped in the development of the methods used here, and who was always willing to give advice for their implementation.

I would also like to thank Dr. Roger Wallace and Dr. Kenneth Watson, who read my thesis and provided valuable comments.

Finally, I would like to thank my wife Susan, whose encouragement and companionship contributed to the completion of this work.

I received financial support from an AEC Special Fellowship in Nuclear Science and Engineering, and a Research Assistantship in the Health Physics Department of the Lawrence Radiation Laboratory at Berkeley. This work was partially supported by AEC Contract AT 0911-10 34 Proj. 161. The bulk of the work was supported by the Health Physics Department of LRL-Berkeley under the auspices of the Atomic Energy Commission.

LEGAL NOTICE

This report was prepared as an account of work sponsored by the United States Government. Neither the United States nor the United States Atomic Energy Commission, nor any of their employees, nor any of their contractors, subcontractors, or their employees, makes any warranty, express or implied, or assumes any legal liability or responsibility for the accuracy, completeness or usefulness of any information, apparatus, product or process disclosed, or represents that its use would not infringe privately owned rights.

TECHNICAL INFORMATION DIVISION
LAWRENCE RADIATION LABORATORY
UNIVERSITY OF CALIFORNIA
BERKELEY, CALIFORNIA 94720